Role of Sulphur on Carbon Deposition on AGR Fuel Cladding Steel

By **Subash Rai**

A Thesis submitted to the University of Birmingham for the degree of Doctor of Philosophy

School of Metallurgy and Materials

University of Birmingham

Birmingham

United Kingdom

B15 2TT

UNIVERSITY OF BIRMINGHAM

September 2018

Abstract

20Cr/25Ni/Nb austenitic stainless steel is used as the fuel cladding in advanced gas-cooled nuclear reactors (AGR). At elevated temperatures, when exposed to CO_2 based environments filamentary carbon deposits form on the surface of the steel. This filamentary carbon deposition is known to be catalysed by metallic nickel-rich particles. Adding a trace amount of carbonyl sulphide (COS) into the gas mixtures suppresses the carbon deposition. To understand the formation mechanism of the nickel-rich particles and the inhibition mechanism of carbon deposition due to the addition of COS, two deposition experiments were performed at 600 °C in 1000 ppm C_2H_4 / 1% CO / bal. CO_2 with and without 215 ppb COS addition. Samples were analysed using electron microscopy techniques. Electron diffraction and energy dispersive spectroscopy (EDS) showed that the metallic nickel-rich particles formed in the oxide layer and assumed the same crystallography as that of the austenitic metal underneath, regardless of the COS addition. Furthermore, it was found that the oxide-metal interfaces were nickel-enriched. A simple model has been proposed to explain the formation of nickel-rich particles within the subsurface oxide layer. In addition, EDS analysis of the sample exposed to a COS bearing gas showed that the surface of the nickel-rich particles in the oxide layers was found to be sulphur-rich. It is believed that it was the surface sulphur adsorption onto the nickel-rich particles, rather than bulk sulphide formation that resulted in the inhibition of carbon deposition on the steel.

It is known that certain sulphur species (such as hydrogen sulphide, H_2S, and methanethiol, CH_3SH) can exist in the reactor, it is important therefore to understand the influence of these species on the catalytic properties of a nickel catalyst. This was investigated in the second part of the current work where the effect of COS, H_2S and CH_3SH on carbon deposition from either 1000 or 5000 ppm ethylene (C_2H_4) in 1 % CO/CO_2 were examined. All three species

were effective at suppressing the carbon deposition, but the effect decreased with increasing concentration of ethylene. When the samples were reacted with 215 ppb COS/1000 ppm C_2H_4 and 259 ppb H_2S/1000 ppm C_2H_4 depositing gas at 600 °C, the formation of carbon filaments was virtually eliminated. However, at higher concentration of ethylene 188 ppb COS, 246 ppb H_2S and 260 ppb CH_3SH all failed to prevent the filamentary carbon formation. Nonetheless, the amount of carbon deposits was significantly reduced. The suppressing effect of sulphur on carbon deposition was explained in term of the role played by the adsorbed sulphur in reducing the rate of the key steps of the growth process of a filament. Of all the three sulphur species, the CH_3SH was the least effective. This was attributed to the formation of surface carbon from the decomposition of CH_3SH that aided the deposition process.

Acknowledgements

I wish to thank Dr Y.L. Chiu and Professor H. E. Evans for their enthusiasm and guidance as my academic supervisors over the past four years. I am forever indebted to Dr M. P. Taylor for her tireless help and support since the beginning of my PhD. Her constant guidance has been invaluable to me. In addition, I am very grateful to Dr B. J. Connolly for his advice and feedback on my progress during the early stage of my PhD.

I would also like to thank my industry supervisors (EDF Energy) Mr N. Smith and Dr C. W. Mowforth for their helpful discussions and for providing me with technical reports.

I would like to express my sincere gratitude to Mrs T. Morris and Mr P. Stanley for the provision of Laboratory facilities, and along with Dr Ding for assisting me with the electron microscope during my training as a microscopist.

I am grateful to several members of Electron Microscopy group for their support and friendship.

I would like to thank my parents and my brother for their love and support.

Lastly, I would like to acknowledge EDF Energy and the Engineering and Physical Sciences Research Council (EPSRC- EP/L017725/1) for funding this project.

Preface

This research was carried out by Subash Rai in School of Metallurgy and Materials, the University of Birmingham (from September 2014 to September 2018), under the supervision of Dr Y. L. Chiu and Prof. H. E. Evans.

The present work is original, and no part of the work has been submitted for another degree at any other university. Wherever other researchers' work has been drawn from or cited, it is acknowledged in the text and the references are listed.

Partial results of the presented work have been published as:

[1] **S. Rai**, M. P. Taylor, Y. L. Chiu, H. E. Evans, B. J. Connolly, N. Smith and C. W. Mowforth, "Electron microscopy study of the formation mechanism of catalytic nickel-rich particles and the role of carbonyl sulphide in the suppression of carbon deposition on 20Cr-25Ni steel," *Materials Characterization,* **144**, 505-515, 2018

Table of Contents

1. Introduction

Carbon deposition has been encountered in various high-temperature processes including nuclear reactors [1, 2], Fischer-Tropsch [3, 4], steam-reforming [5, 6] and steam-cracking [7, 8, 9]. It is an unwanted by-product resulting from the surface catalytic reaction between the carbon precursor (CO and hydrocarbons) and hot metals (such as iron, nickel, cobalt). Excessive carbon accumulation can lead to reactor blockage, reduction of heat transfer properties and degradation or deactivation of the catalyst. One such example where carbon deposition is observed is on the surfaces of the stainless steel fuel cladding in an Advanced Gas-Cooled Reactor (AGR).

The AGR uses high pressured carbon dioxide as the primary coolant, graphite as a neutron moderator and stainless steel (20Cr/25Ni/Nb) as a fuel cladding material. Carbon dioxide is radiologically compatible and has good heat transfer properties at high pressure, making it an efficient coolant medium. However, under intense gamma and neutron irradiation, carbon dioxide decomposes to give oxidising species that react with graphite, resulting in its weight loss [10, 11]. Since the moderators are not designed to be replaced, the oxidation of graphite is suppressed by allowing a small concentration of carbon monoxide to build up and the addition of a small concentration of methane into the coolant. However, the addition of methane can result in carbon deposition on the surface of stainless steel fuel clad and in sections of the boilers (Fig.11 (a)) and boiler (Fig.1.1 (b)).

It has been shown that the filamentary carbon deposited on 20Cr/25Ni/Nb steel were catalysed by metallic nickel-rich particles [12]. These particles are formed during the oxidation of steel. Under AGR operating conditions, nickel is the only alloying element which is thermodynamically stable, whereas iron and chromium oxidise to Fe_3O_4 and Cr_2O_3 which are catalytically inactive towards carbon deposition. Fig.1.1 (c) demonstrates the clear

association of heavy carbon deposition with the high nickel alloys in the boiler transition pieces.

The accumulation of such carbon deposit can have an undesirable effect (Fig.11. (d)). An excessive carbon build-up can reduce the heat transfer efficiency of the fuel clad so drastically that it can lead to failure. One way to suppress the carbon deposition on the cladding steel is to form a physical barrier such as protective chromia [12] and/or silica layers [12, 13] or to increase the oxygen potential of the system such that the oxidation of nickel is favourable [14]. However, the currently implemented method to mitigate the carbon deposition problem is to inject carbonyl sulphide (COS) into the gas coolant. A previous study [15] has shown that only 240 ppb COS added to the carbon depositing gas was able to prevent deposition at 550 °C and, to inhibit further growth of pre-existing deposit. Two possible mechanisms [15] have been proposed on the role of sulphur in deactivating nickel particles, namely bulk sulphiding and surface poisoning by sulphur adsorption. No experimental evidence supporting either mechanism has been obtained previously [15].

In the AGR coolant, other forms of sulphur species can exist. The evidence of other sulphur species was found from the plant measurements of total sulphur [S] and [COS] concentration which showed that the [S]/ [COS] ratio is more than 1 [16]. Thermodynamic equilibrium calculation suggests that COS and H_2S are the most prevalent sulphur species [17]. Other sulphur species such as SO_2, CS_2, HS, H_2S_2, S_2 and CH_3SH also exist in trace amount [18, 19]. The amount of carbon deposition suppressed by sulphur depends not only on the concentration [20] but also the chemical nature of the sulphur species [21, 22]. It is important therefore to understand the influence of other species on the catalytic properties of a nickel catalyst.

The aim of this project was to characterise and study the formation mechanism of the catalytic nickel-rich particles and to improve the understanding of the inhibiting role of carbonyl sulphide (COS) on the carbon deposition on 20Cr-25Ni steel. Furthermore, this project aims to investigate the poisoning effect of various sulphides (COS, H_2S and CH_3SH) on carbon deposition on 20Cr-25Ni steel.

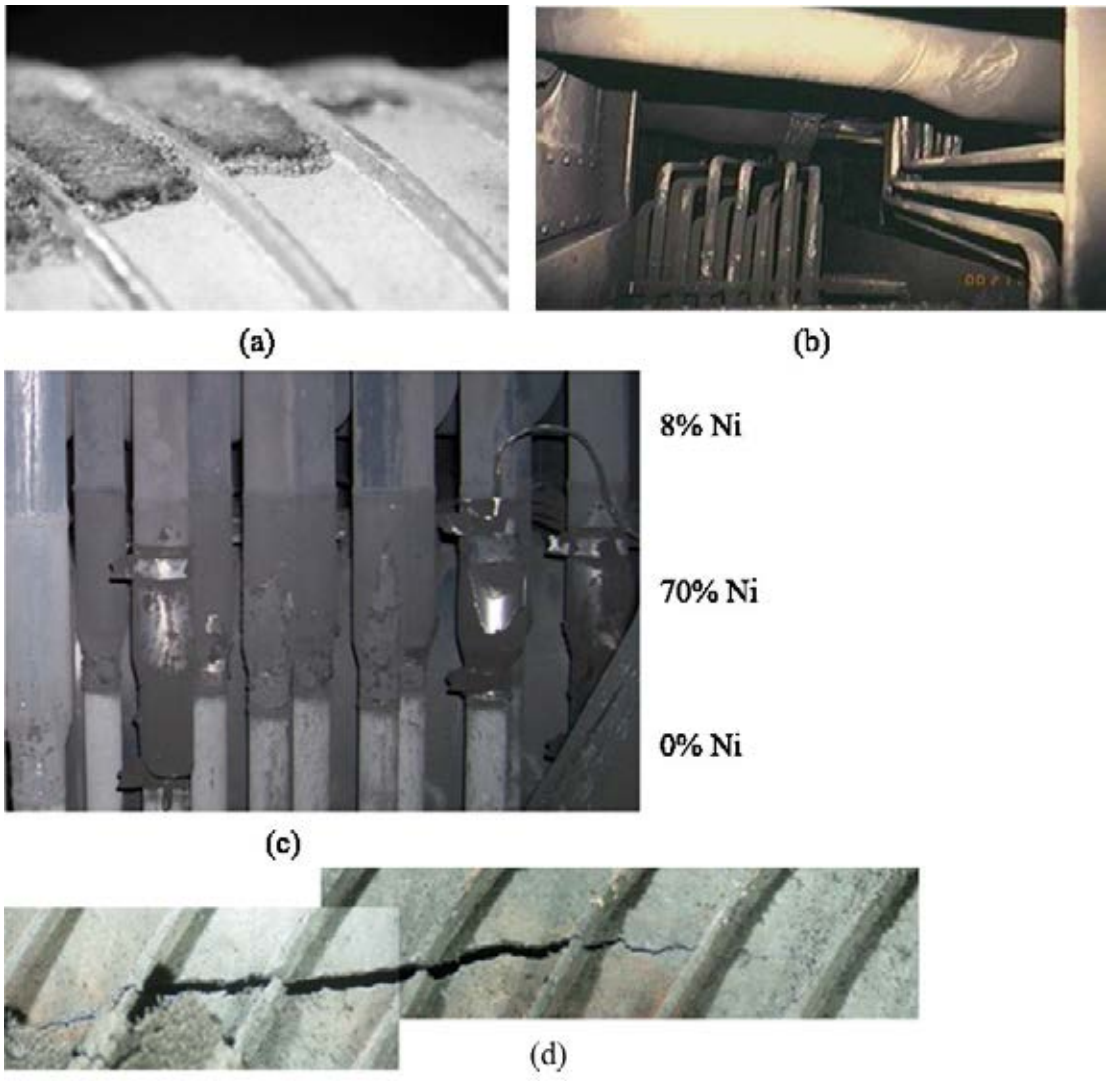

Fig. 1.1: Carbon deposition on (a) fuel element and (b) boiler. (c) Influence of Ni concentration on carbon deposition. (d) Fuel clad failure due to excessive carbon deposition *[23]*.

2. Literature Review

2.1. A Brief History of 20Cr-25Ni Stainless Steel

For a material to be used as nuclear fuel clad it must satisfy several criteria such as low thermal neutron absorption cross-section, chemical compatibility with the environment (fuel and coolant), corrosion resistance, good thermal conductivity and mechanical properties at elevated temperature [24]. For early gas-cooled reactors, aluminium, magnesium and beryllium were considered as the cladding material due to their low neutron absorption cross-section. Aluminium was the first cladding material to be used in a gas-cooled (air) reactor [24, 25]. However, their use as cladding material was limited as they have poor high-temperature properties. For higher coolant temperature aluminium became unfeasible.

Magnesium has a lower neutron capture cross-section than aluminium. It was rejected for cladding material in earlier air-cooled reactors as the magnesium has inferior oxidation resistance in air. However, it became favourable for carbon dioxide-cooled reactors due to its superior oxidation resistance in carbon dioxide [26]. Magnesium also has good compatibility with uranium fuel at high temperature. Subsequently, an oxidation resistant magnesium alloy called Magnox [27] was developed which was used in commercial Magnox reactors.

A magnox reactor operates at less than 400°C (coolant outlet temperature) [28]. Above this temperature, the magnesium alloy has poor high-temperature properties. Magnesium alloys melt at 650°C. At above 450°C, they have poor oxidation resistance, inadequate creep resistance [29] and react with uranium [30], making them unpractical at this elevated temperature. The need for higher power output meant that the reactor was needed to operate at a higher temperature which led to the development of the advanced gas-cooled reactor (AGR). It was planned to raise the cladding temperature by 250°C and the coolant outlet

temperature by 220°C [31]. As a result of which, beryllium and stainless steel were considered as a cladding material for the AGR.

Beryllium has a higher melting point than stainless steel. Owing to its low neutron absorption cross-section, beryllium was more attractive than stainless steel for fuel clad. It was used in an early AGR. However, it was realised that the beryllium clads had inadequate ductility, low creep strength and poor corrosion resistance in AGR reactor conditions. This, coupled with the high cost associated with the production of beryllium clad led to a loss of interest and the effort was concentrated in developing stainless steel as a cladding material for AGR [29, 30].

The major drawback in using stainless steel was that it has a relatively high neutron capture cross-section (about 90 times higher than magnesium alloy [30]). There was also the possibility of reaction between the stainless steel and (metallic) uranium fuel [24]. The former problem was solved by using the thin-walled tube (0.38mm) and an enriched uranium fuel, and the latter was solved when the metallic uranium was replaced with uranium dioxide as fuel.

Stainless steel of austenitic type was chosen as it had excellent oxidation resistance, adequate ductility, and creep strength. For it to be used as fuel clad, it was required in the form of a thin-walled tube that is free from detrimental inclusions. This was achieved by using a vacuum melting process that gave high degrees of cleanliness [32]. With regards to its alloy composition, particular attention was given to its metallurgical stability.

Initially, five niobium stabilised steels with 18 to 25% chromium concentrations were selected for possible cladding materials. These were 18Cr/8Ni/Nb, 19Cr/14Ni/Nb 20Cr/25Ni/Nb, 25Cr/20Ni/Nb and 25Cr/23Ni/3Mo/1V/Nb [29]. The last alloy was rejected as it had seriously inferior oxidation resistance. The other four alloys were tested for their oxidation resistance in 5% CO/CO_2 at 300 lb/in^2 *g* over the temperature range 650-800°C.

The result showed (Table 2.1) that the oxidation resistance of the more highly alloyed material was superior and 20Cr/25Ni/Nb and 25Cr/20Ni/Nb were considered most favourable.

Table 2.1: Oxidation (weight gains expressed as mg/cm^2) of stainless steels in CO_2 5% CO by volume at 300 lb/in^2 gauge *[29]*.

Materials		650°C			750°C			800°C		
		1000 h	3500 h	10000 h	1000 h	3500 h	9000 h	1000 h	3500 h	10000 h
Sheet Materials:										
18/8/Nb	P	0.46	0.59	0.74	0.75	0.80	0.97	0.54	0.64	0.87
	A	0.11	0.30	0.50	0.27	0.32	2.10	0.06	0.41	0.89
20/25/Nb	P	0.16	0.22	0.36	0.21	0.25	0.39	0.26	0.35	0.51
	A	0.09	0.20	0.38	0.17	0.21	0.27	0.08	0.45	0.57
25/20/Nb	P	0.12	0.19	0.34	0.16	0.21	0.31	0.22	0.31.	0.48
	A	0.10	0.25	0.46	0.18	0.24	0.14	0.25	0.39	0.51
Tube Materials:										
18/8/Nb	P	0.59	0.73	0.90	1.02	1.11	1.19	0.55	0.65	0.83
19/14/Nb	P	0.30	0.40	0.55	0.50	0.58	0.74	0.37	0.52	0.80
20/25/Nb	P	0.13	0.22	0.37	0.19	0.25	0.34	0.26	0.39	0.53
20/25/Nb‡	P	0.22	0.29	0.44	0.30	0.38	0.49	0.24	0.32	0.47
25/20/Nb	P	0.21	0.31	0.46	0.30	0.33	0.51	0.27	0.39	0.62
AGR 20/25/Nb‡ production type can		0.25	0.36†	0.41	0.24	0.33†	0.38	0.27	0.35†	0.47

† Weight gain after 4500 hours.

‡ Double Vacuum melted: all others single vacuum melted.

A abraded to 600 SiC grit.

P acid pickled.

The next stage of the selection process was based on the thermal stability tests which involved 10000 h ageing treatments at 650-750°C and a subsequent Charpy impact test at room temperature. The test showed that of the four alloys tested, 20Cr/25Ni/Nb was found to be the most stable, and 25Cr/20Ni/Nb to be the most embrittled. The latter contained 30-40% sigma phase after 10000 h treatment at 750°C.

On this basis, 20Cr/25Ni/Nb was selected as the cladding material for AGR. Furthermore, studies of the 20Cr/25Ni/Nb alloy at 750 and 900°C in CO_2 have confirmed the choice of cladding material based on its compatibility (oxidation resistance) with CO_2 even at temperatures higher than had been originally envisaged.

2.2. Oxidation of 20Cr-25Ni Stainless Steel in the CO_2 Atmosphere

During the normal reactor operation, the steel-clad must withstand the severe CO_2 environment at a temperature between 400°C to 850°C. Over the past several decades, a considerable number of studies have been made on the oxidation of 20Cr-25Ni-Nb stainless steel in CO_2, covering several aspects of the oxidation process, such as spallation [33, 34, 35, 36, 37], oxide characterisation [38, 39, 40, 41, 42], pit formation [43], the influence of minor alloying elements [44, 45] and metallurgical stability [29].

The compatibility of 20Cr/25Ni/Nb steel with CO_2 at elevated temperature is attributed to its excellent corrosion resistance in CO_2. At high temperature, the surface of the steel-clad oxidises to form a protective chromium-rich oxide layer that acts as a barrier to further oxidation by slowing the outward diffusion of metal cations. It has been demonstrated that about 15-19 wt % minimum (surface) chromium concentration is required to form this protective layer [43, 46, 47].

When the steel-clad (M) is exposed to carbon dioxide, the primary oxidation reaction is $M + CO_2 \rightarrow MO + CO$, with a secondary reaction of $2M + CO_2 \rightarrow 2MO + C$ contributing less

than 7% to the total weight gain [48]. The oxide formed on the 20Cr/25Ni/Nb after exposure to CO_2 at < 850°C has been well characterised [42, 49, 50, 51]. The fully-developed oxide scale is duplex in nature, consisting of an outer (Fe, Cr, Mn) rich spinel and inner chromium rich rhombohedral layer. For an extended oxidation, e.g. after 4900 h exposure in CO_2 at 825°C, a third, silicon rich, oxide layer can form at the oxide-metal interface, Fig. 2.1 [52].

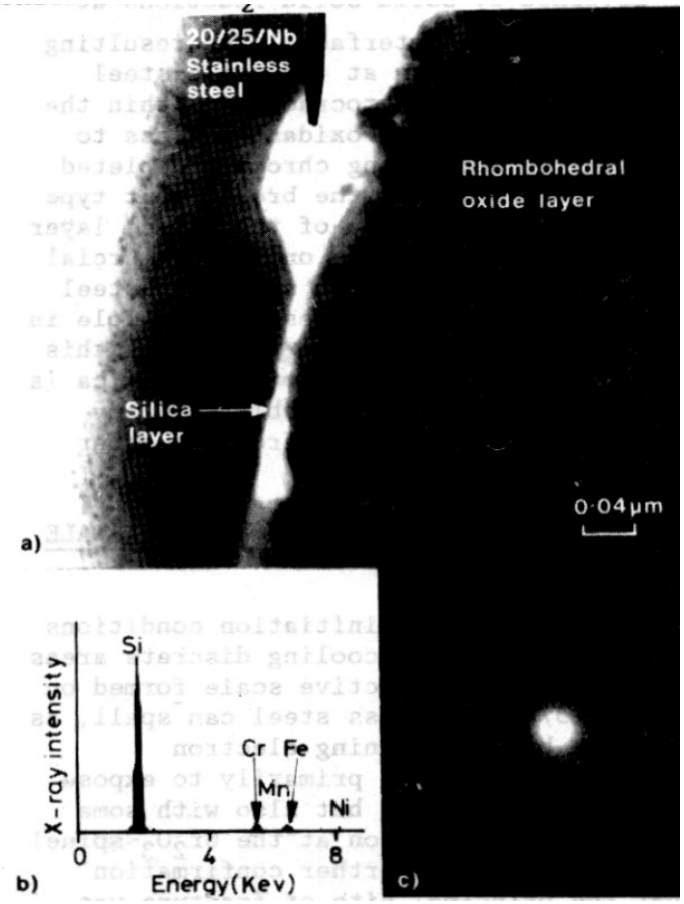

Fig. 2.1: (a) Microstructure, (b) EDS analysis and (c) micro-diffraction pattern of the silica layer formed at the interface with underlying 20/25/Nb steel during 4900 h oxidation in CO_2 at 825°C *[52]*. Clearly, the innermost oxide layer was thin (between 5 and 20 nm thick) amorphous silica.

2.2.1. The Initial Oxide Formed on 20Cr/25Ni/Nb Steel

The formation of initial oxide in 20Cr/25Ni/Nb steel is complex and depends on the temperature and pressure. Tyler [39] has investigated the formation and growth of oxide layers on 20Cr/25Ni/Nb steel, oxidised at 700°C in 50 torrs (0.07 atm) CO_2 for 2 min – 100 hr. After a 2 min oxidation period, the surface oxide was iron-rich with virtually no (<1 at %)

chromium and there was little change in the surface composition throughout the oxidation period Fig. 2.2. On completion of 100 hr oxidation, the bulk oxide consisted of Fe-Cr-rich spinel, Fig. 2.3.

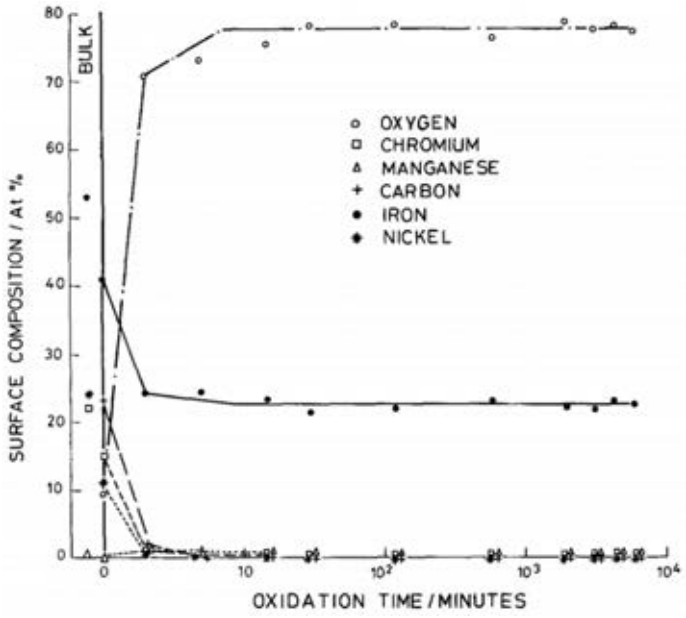

Fig.2.2: The surface composition of 20Cr/25Ni/Nb steel during oxidation in 50 torr CO_2 at 700°C. *[39]*

A similar result was observed by Tempest and Wild [40] for "in-situ" oxidation of steel in 1 atm CO_2 at 850°C. They reported only iron oxide was formed on the surface after 1 min exposure and the surface composition of oxide remains unaltered for up to 45 min of exposure. Only after 180 min of oxidation period, incorporation of chromium into the iron oxide was barely detected. This observation [40] was in contrast with the sample oxidised at 850°C in CO_2 at a much lower pressure of 5×10^{-2} torr (6.6×10^{-5} atm) where the initial surface oxide was chromium rich with some iron and silicon. After the oxidation period of 180 min, the surface was completely covered with a chromia layer.

Based on these observations and a literature survey, Tempest and Wild [40] summarised that at high pressure and at a temperature below 850°C, the oxide which forms initially on 20Cr/25Ni/Nb steel is an iron oxide which, subsequently, incorporates chromium and

manganese into iron-rich spinel. At a later stage, chromium-rich rhombohedral oxide grows as an inner layer beneath the primary spinel phase. The chromia is then separated from the metal by a thin silica layer.

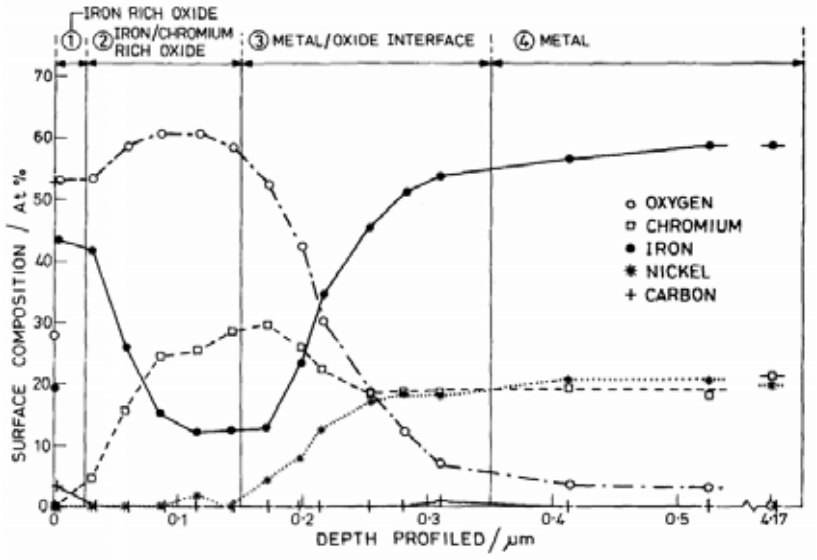

Fig. 2.3: Chemical depth profile through the oxide formed on 20Cr/25Ni/Nb steel oxidised in 50 torr CO_2 at 700°C for 100 hr. *[39]*

Based on the free energy of formation of each oxide, SiO_2 is expected to form first, followed by Cr_2O_3 and Fe_3O_4. However, Tempest and Wild [40] argued that at high pressure, thermodynamic equilibrium does not exist during the early stage. It can be achieved at low pressure and high temperature. They proposed that, at low pressure (such as 5×10^{-2} torr CO_2 at 850°C) the rate of arrival of gas atoms at the surface is slow relative to the diffusion of metal atoms in the surface and from the bulk, there is enough time for the most stable oxide to form (chromia). Indeed, Bennett *et al.* [53] have shown that by annealing 20Cr/25Ni/Nb steel in low oxygen partial pressure 50:1 H_2/H_2O for 1 hr at 930°C, a chromia layer, separated from the underneath alloy by a thin silica layer, was formed. Similarly, Tempest and Wild [54] demonstrated that chromia-rich oxide could be induced at a temperature above 850°C and pressure below 10^{-3} torr (~10^{-6} atm). However, at high pressure (above 1 atm, non-

equilibrium) they suggested that the gas atoms would react with all the atoms at the surface to form a mixed iron, chromium, and nickel (if thermodynamically allowed) spinel.

2.2.2. Growth Mechanism of Duplex Oxide

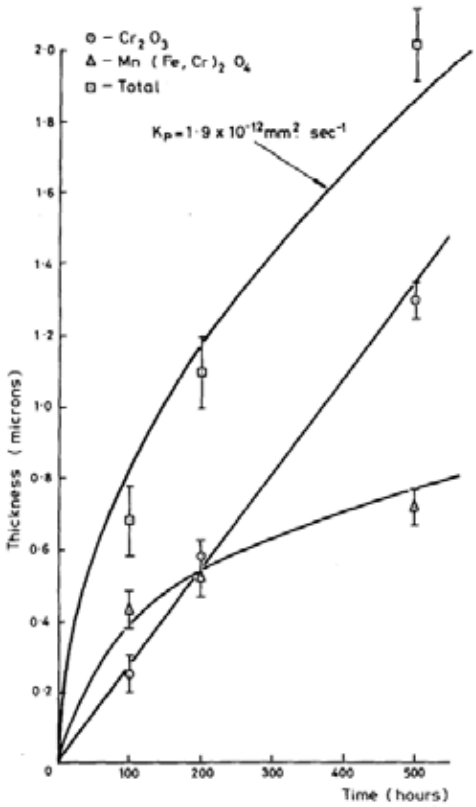

Fig. 2.4: Variation of oxide thickness with time for 20Cr/25Ni/Nb steel oxidised in 1 atm CO_2-2% CO at 850°C. *[50]*

The duplex oxide formed at ≤ 850°C consists of outer spinel and inner rhombohedral layer. Once a uniform oxide layer is formed the overall growth rate is controlled by the diffusion of the metal cation in the oxide [55]. Evans *et al.* [55] and Tempest and Wild [50] showed that the initial oxide growth obeys parabolic kinetics but deviates towards linear rates (paralinear kinetics) at a later stage. Evans *et al.* [55] have attributed the increase in oxidation kinetics to the breakdown of protective chromic oxide scale that led to rapid oxidation of the underneath alloy (mainly iron) on exposed areas that were depleted in chromium. Alternatively, Tempest and Wild [50, 40] explained that the deviation in kinetics from parabolic to paralinear during the first 500 hr oxidation at 850°C in 1 atm CO_2-2%CO was because of the different growth

rate of spinel (parabolic) and chromia layer (linear) giving an overall paralinear kinetics. This is shown in Fig. 2.4. They suggested that the growth of spinel layer is controlled by the outward diffusion of cations, giving a parabolic kinetic, whereas the linear growth mechanism of chromia layer is the solid-solid reaction between the spinel and the alloy.

As the secondary chromia forms beneath the spinel layer, the growth mechanism of chromia must be either anion diffusion from the gas-oxide interface to the oxide-metal interface or the transfer of oxygen must take place at the base of the oxide via a solid-state reaction. Diffusion of anions through an oxide layer would suggest parabolic kinetic growth of chromia. Since the chromia growth did not pertain to parabolic kinetic growth, Tempest and Wild [50] argued that the solid-state reaction between the alloy and the spinel is more likely to be the growth mechanism of chromia. They proposed [40] that 20Cr/25Ni/Nb steel oxidises (in >1 atm CO_2 at 500°C-850°C) initially by forming an iron-rich spinel layer at the surface. Chromium then reduces the iron-rich spinel to mixed Fe-Cr spinel which is also reduced by chromium to Cr_2O_3:

$$Fe_3O_4 \xrightarrow{+Cr} FeCr_2O_4 \xrightarrow{+Cr} Cr_2O_3 \qquad (1)$$

Similar reasoning was presented by England *et al.* [52] on the formation of the chromia layer via a solid-state reaction.

The early growth rate is controlled by the grain boundary diffusion of cations through the spinel layer. However, once the chromia has attained a certain thickness (after more than 500 hr) the rate-control changes from interface kinetics to slower cation diffusion through the chromia layer.

At higher temperature (> 850°C) the solid-state reaction occurs rapidly, and iron-rich spinel is quickly reduced to thick chromia in a short time and controls the diffusion of the cation. At

lower temperature (< 500°C) the formation of the Cr_2O_3 layer takes a very long time. As a result, at high and low-temperature parabolic growth kinetics are expected to pertain since the rate-control is cation diffusion predominantly through a single phase.

Thermodynamically, the formation of chromia at the expense of spinel is the result of a high free energy of formation of Cr_2O_3 [40]. Since the free energy of formation of SiO_2 is even larger, it is possible that the Cr_2O_3 is reduced by the silicon, present in the alloy at <0.6 wt%, to form the SiO_2 at the metal-oxide interface. This proposal is consistent with the work of Bennett *et al.* [53, 52] who suggested that the silica layer grew laterally underneath the Cr_2O_3 layer by the oxidation at an oxygen partial pressure governed by the Cr/Cr_2O_3 equilibrium. The silicon diffusion occurred via grain boundaries in the alloy, Fig. 2.5. Eventually, the fully formed silica would control the overall oxide growth rate by slowing down the cation diffusion through the silica layer.

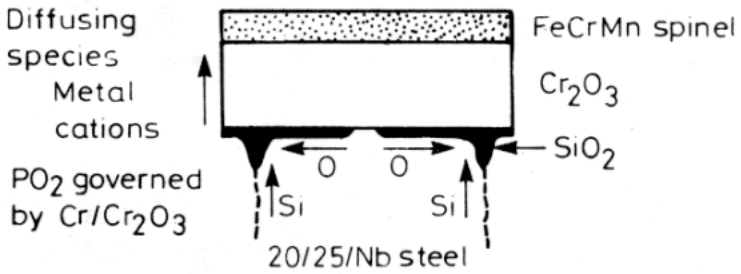

Fig. 2.5 Schematic illustration of the mechanism for silica formation *[52]*.

2.3. Filamentous Carbon Deposition

Carbonaceous deposits are commonly found on metal surfaces when exposed to the carbon bearing gases in a number of commercial processes. The deposits have a complex structure with various growth forms. They are categorised into three types: amorphous, filamentous and graphitic shell-like and they are collectively known as “coke” [56, 57]. Since the current

work is on the study of filamentous carbon, subsequently, only the literature of this carbon is reviewed below.

In the literature carbon deposits with a filamentous morphology [58] were identified as carbon filaments, carbon whiskers, filamentous carbon, carbon nanofibers and more recently, as carbon nanotubes (CNTs). For the current study, the term carbon filament and filamentous carbon have been used to identify the carbon deposit.

The discovery of filamentous carbon dates to more than a century ago. In 1889, it was first reported in a patent [59] that carbon filaments are produced from hydrocarbon in metallic crucibles. In 1890 a paper [60] was submitted to French Academy of Sciences reporting the growth of filamentous carbon. The first TEM observation of a carbon filament formed by CO decomposing on an iron substrate appeared in 1952 [61]. It was not until the advances in electron microscopy technique in the 1970s and 1980s that led to the understanding of growth mechanisms and structural details of carbon filaments.

Filamentous carbon is formed by the catalytic decomposition of carbon-bearing gases (such as CO, C_xH_y) on metal nanoparticles. The appearance of filamentous carbon has been observed in various industrial practices including nuclear reactors [1, 2], Fischer-Tropsch [3, 4], steam-reforming [5, 6], steam-cracking [7, 8, 9], methanation [5] and Bosch-process [62]. Originally, the occurrence of carbon filaments in the various industries was considered a nuisance – an unwanted by-product. The presence of carbon filaments has an undesirable effect such as blockage of reactors, reduction of heat transfer properties and destruction or deactivation of the catalyst. This has motivated workers to understand the growth mechanism and the prevention of carbon deposition. However, since the discovery of new allotropes of carbon called carbon nanotubes (CNT) in 1991 [63], the trend has shifted to optimizing the growth of filamentous carbon. This cylindrical nanostructured material has unique electrical,

magnetic, mechanical and thermal properties, making it technologically important [64]. This has boosted the interest in filamentous carbon deposition since the mechanism for the synthesis of CNT is similar to the original mechanism proposed for the formation of filamentous carbon.

In the past 60 years considerable research has been done on filamentous carbon and the main area of research were the morphology of the deposit [65, 66, 67, 68, 57, 69], the catalytic growth mechanism [70, 71, 67, 72, 73, 74, 75, 76], the driving force for carbon diffusion [71, 72, 77, 78, 73, 74, 75, 58, 76], the thermodynamics of formation of filamentous carbon [70, 71, 67, 79, 62, 72, 76] and the inhibition/suppression of carbon deposition [67, 80, 81, 8].

2.3.1. Growth Mechanism: Bulk diffusion

The early successful model explaining the growth of carbon filaments was proposed by Baker and co-workers [78, 66, 75]. They successfully applied the controlled atmosphere electron microscopy (CAEM) technique to directly observe the growth of filamentous carbon on various metal (including nickel, iron, cobalt and chromium) surfaces when reacted to hydrocarbon environments. Using this pioneering technique, they were able to obtain detailed insight into the growth characteristics of carbon filaments and also obtain the kinetics of the process. By continuous observation, they were able to show that the filament grew with the deposition of carbon at the rear face of an advancing particle. The size of the particle dictated the width of the filament. The catalyst particle was encapsulated by layered carbon on the filaments that had ceased to grow. An example of a typical filament with the particle at the tip is shown in Fig. 2.6 (a).

Based on these observations, the following mechanism was proposed to describe the carbon filament formation process, as outlined in Fig. 2.7: the hydrocarbon is adsorbed on the ‘front’ surface of the metal particle followed by catalysed decomposition of the hydrocarbon to

hydrogen and carbon species. The carbon then dissolves and diffuses through the particle and precipitates at the other end. As the carbon deposit grows, the metal particle is detached from the bulk surface and remains at the tip of the filament. Excess carbon can build up at the exposed faces and is transported by surface diffusion around the peripheral surfaces of the particle to form the outer skin of the filament. During the filament growth, the front face of the particle remains free of deposit and the growth ceased when the leading face was encapsulated by carbon, thus preventing further hydrocarbon decomposition. This 'classical' model is known as a *tip-growth mechanism*.

It was proposed that the bulk diffusion of carbon through the particle is the rate-determining step. This is based on the remarkable finding that the activation energies of the filament growth correlate with those for diffusion of carbon through the corresponding particles. This is listed in Table 2.2. Furthermore, Baker and co-workers found that the rate of growth of carbon filaments was inversely proportional to the square root of the particle size, which was thought to be the implication of bulk diffusion-controlled mechanism [75].

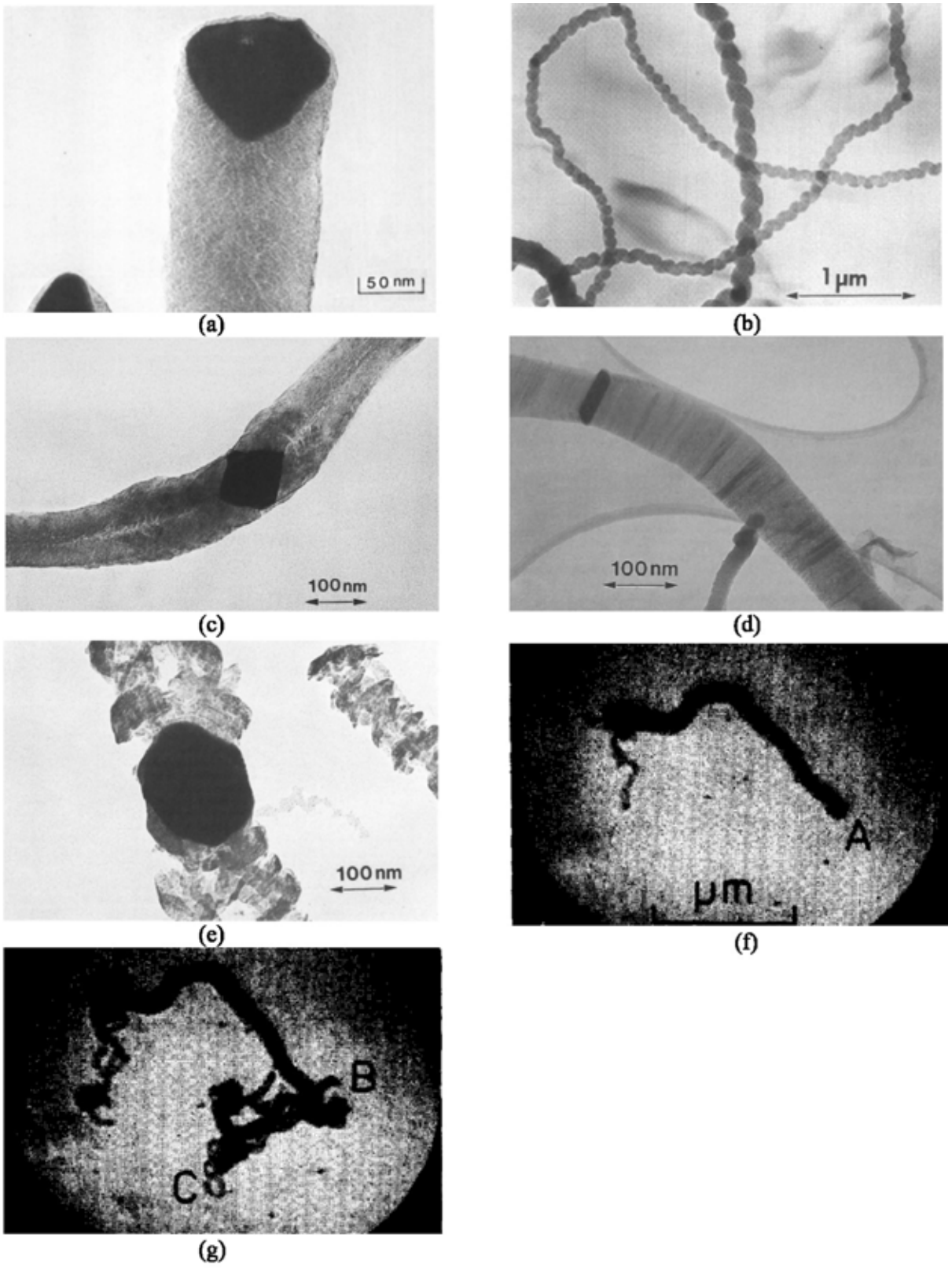

Fig. 2.6: Transmission electron images of different types of growth observed in catalytically-produced carbon filaments. (a) Whisker-like *[82]*. (b) Spiral *[69]*. (c) and (d) Bi-directional *[57]*. (e) Multi-directional *[57]*. (f) The growth of whisker-like filament from particle 'A' which fragmented into (g) particle 'B' and 'C', and subsequent secondary filament growth, i.e., Branched-filament *[66]*.

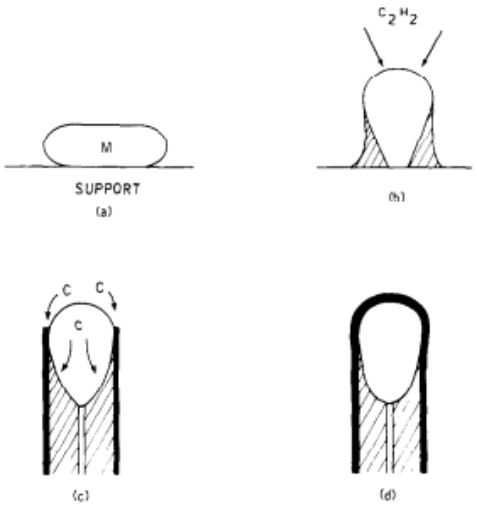

Fig. 2.7: Growth mechanism for 'whisker-like' carbon filament *[78]*.

It was suggested that the driving force for carbon diffusion is the temperature gradient across the catalyst particle created by the exothermic decomposition of hydrocarbon (acetylene) at the leading face of the particle and endothermic precipitation of carbon on the rear face.

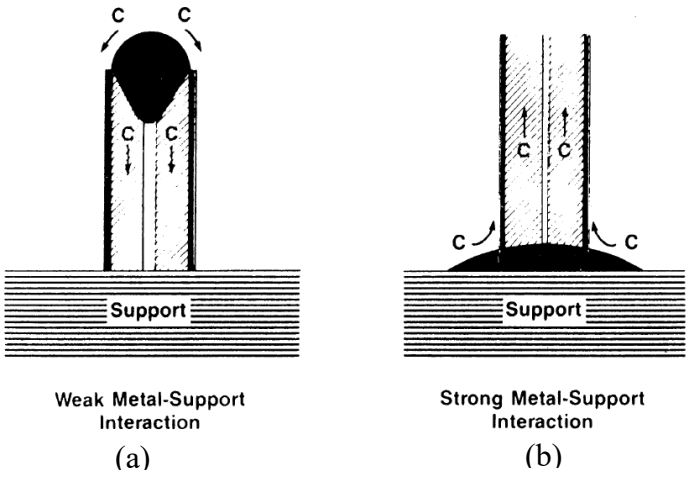

Fig. 2.8: Influence of the metal-support interaction on the mode of growth of filamentous carbon *[82]*. (a) Whisker-like growth. (b) Extrusion growth mode.

Baker *et al.* [56, 75] also suggested the influence of the catalyst-support interaction on the mode of filament growth mechanism. If the particle has a weak bond with the support, then the particle can be detached and filaments grow via the *tip-growth mechanism*. However, if the interaction is strong the filament is formed via extrusion mode, also known as *base-*

growth or root-growth, where the particle remains anchored to the surface, Fig. 2.8. In both growth modes, the critical steps remain carbon solubility and diffusion through the catalyst. Examples of extrusion growth mode can be found in [83, 84, 85].

The importance of carbon solubility and diffusivity through the catalyst particle was further highlighted by Deck and Vecchio [86] who studied the growth of carbon filaments using a variety of transition metals, in the form of metallocenes and chlorides. Only Fe, Ni and Co were able to catalyse the growth of carbon nanotubes. The other elements, consisting of Cr, Mn, Zn, Cd, Ti, Zr, La, Cu, V, and Gd, were found to be inactive. They explain this observation in terms of the carbon solubility in metals: Fe, Ni and Co had carbon solubility limits of 0.5 to 1.5 wt% carbon, while the unsuccessful catalysts had either negligible carbon solubility, or multiple carbides were formed, making it difficult for the carbon diffusion required for nucleation and growth of nanotubes. Note that, while Cr and V are found to be inactive by Deck and Vecchio, however, Baker *et al.* [66, 84] (see Table 2.2) have successfully catalysed the growth of carbon filaments from these metals. The difference can be attributed to the use of different reactants. Deck and Vecchio reacted Cr and V as chloride with benzene, while Baker *et al*. reacted pure Cr and V with acetylene.

While this bulk-diffusion model successfully explains the growth mechanism of the whisker-like filament (single straight filament with a single catalyst particle at its tip), it has a number of drawbacks that demands modification of this model [75]. A major criticism of this model is the driving force for carbon diffusion as it fails to account for the formation of filaments from the endothermic decomposition of hydrocarbon such as methane. Alternatively, the concentration/activity driven carbon diffusion mechanism is proposed. This is discussed below in section 2.3.4. Likewise, there is a controversy with regards to the chemical state of the catalyst. Various authors have credited the metallic phase as a catalyst, while others

argued that the active state is carbide (section 2.3.3). Furthermore, the model does not predict the growth of filaments other than whisker-like morphology, as shown in Fig. 2.6.

Table 2.2. Comparison of measured activation energies for carbon filament growth with those for carbon diffusion in the corresponding metal catalysts *[56]*.

Catalyst	Activation energy for filament growth[a] (kcal/mol)	Activation energy for diffusion of carbon (kcal/mol)
Nickel	34.7	33.0-34.8
α-iron	16.1	10.5-16.5
γ-iron	33.9	33.3-37.4
Nickel-Iron	33.6	34.0
Cobalt	33.0-33.3	34.7
Vanadium	27.6	27.8
Molybdenum	38.8	41.0
Chromium	27.1	26.5
[a]Directly measured by *in-situ* electron microscopy.		

Several alternative mechanisms have been proposed to account for the observed different filament morphology. For spiral-helical type filament (e.g. Fig. 2.6 (b), Boehm [68] has suggested the mechanism based on diffusion path length. This is shown schematically in Fig. 2.9. If the particle has an angular shape, a curved carbon filament would grow from an active face due to the different diffusion path lengths. This would result in a helical growth form and if two adjacent faces are active, double helices are formed.

Rodriguez *et al*. [87] and Baker *et al*. [57] have discussed the influence of catalyst particle morphology on the resulting structural characteristic of carbon filaments. They use bimetallic particles consisting of a combination of iron, nickel, cobalt and copper in either C_2H_4/H_2 or CO/H_2 system. A schematic representation of various morphologies of bimetallic particles during the interaction with the selected gas environment and the morphology of carbon filament generated from the corresponding particles are shown in Fig. 2.10 and 2.11, respectively. If the catalyst is the rhombic or diamond shape (Fig. 2.10 (a)), the graphite

platelets constituting the filaments are aligned at an angle to filament axis with a “herring-bone’’ appearance, Fig. 2.11 (a). This is a type of bi-direction filament as shown in Fig. 2.6 (c). In this case, two faces are active in the decomposition of the reactant gases and the other four faces are responsible for the precipitation of graphite. If the catalyst particle adopts a rectangular crystallite (Fig. 2.10 (b)) then four faces participate in the decomposition reaction and carbon is deposited on the other two faces, Fig. 2.11 (b). This is another type of bi-directional filament (see Fig. 2.6 (d)). Finally, for the particle that acquired hexagonal-shaped morphology (Fig. 2.10 (c)), two faces are involved in the decomposition reaction and carbon precipitation occurs at the other six faces, giving it multi-directional appearance, Fig. 2.11 (c). An example of the multidirectional filament is shown in 2.6 (e).

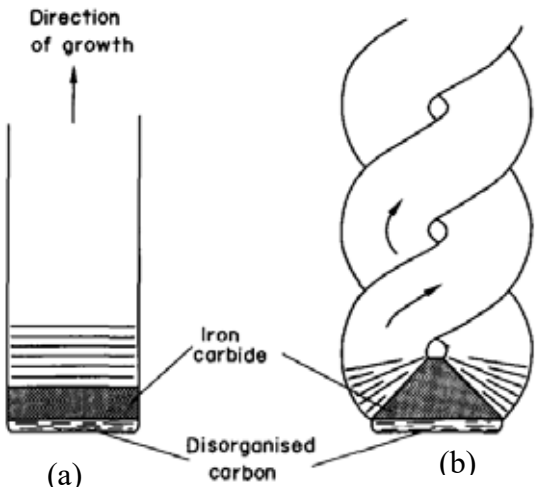

Fig. 2.9: Schematic of the growth mechanism of filamentous carbon on iron carbide. (a) On rectangular carbide particle. (b) On the carbide particle with two active faces at oblique angles *[68]*.

Secondary filament growth along the sides of the primary filament has been reported [66, 81]. This ‘branching’ can occur (Fig. 2.6 (g)) when the primary catalyst particle, Fig. 2.6 (f) is fragmented and subsequently, a secondary filament is grown from the fragmentary particles. Fragmentation of a parent particle can either occur in a single explosive act, creating many smaller particles that proceeded to generate finer filaments, or small particles will split

continuously from the main particle. The latter mode will result in the growth of secondary filaments at intervals along the sides of the primary filament [81, 82].

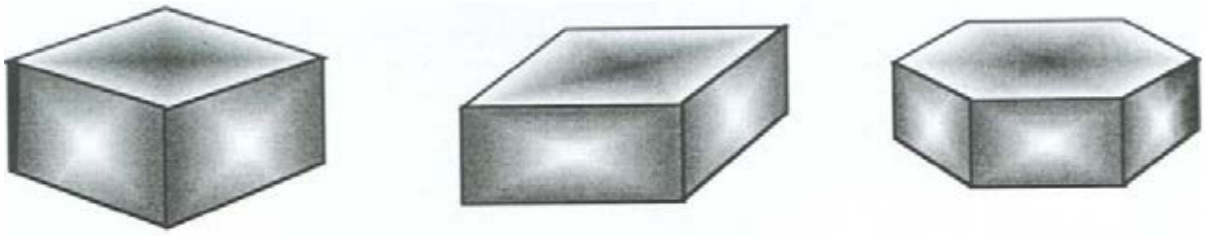

Fig. 2.10: Schematic representation of the observed morphological characteristics of various bimetallic particles during the interaction with selected gas environments. (a) an Fe-Ni (5:5) particle undergoing reaction in C_2H_4/H_2 (4:1) at 500°C, (b) a Cu-Fe (2:8) particle heated to 475C in the presence of CO/H_2 (4:1), and (c) a Cu-Co (1:3) particle treated in C_2H_4/H_2 (4:1) at 525°C *[57]*.

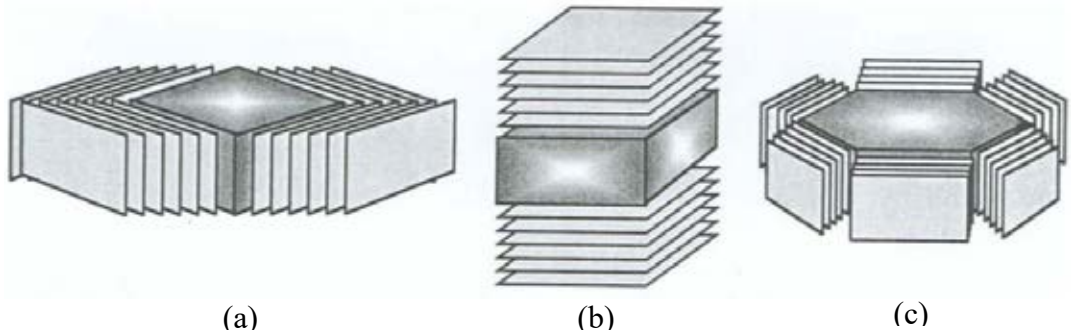

Fig. 2.11: Schematic representation of the different arrangements of graphite platelets generated from the three systems in Fig. 2.10 *[57]*.

Snoeck *et al*. [76] have proposed a model to describe the formation of hollow filament: At low temperature, the nucleation rate for carbon filament is slower than the diffusion rate, as a result, uniform nucleation occurs at the particle/carbon interface. The particle is lifted from the bulk by the growing *full* filament, Fig. 2.12(a). However, at high temperature, the nucleation (once metal is supersaturated with carbon) is instantaneous. The difference in diffusional path length meant that rapid carbon deposition occurs at the particle/carbon interface that is closer to the gas/particle interface. This is followed by a sharp drop in carbon concentration in the metal to the saturation concentration of filament, thus no driving force exists. Hence, no carbon deposition occurs at places with high diffusional path length and as the process continues, a hollow carbon filament is formed, Fig. 2.12 (b).

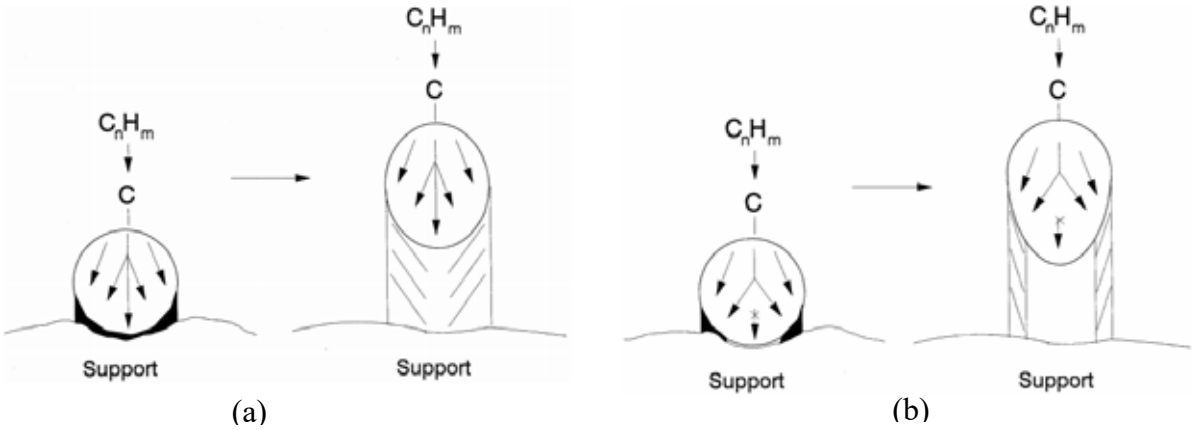

Fig. 2.12: Schematic representation of the formation of (a) full filament at low temperature and (b) hollow filament at high temperature *[76]*.

2.3.2. Carbon transport: Surface diffusion

The alternative to bulk diffusion mechanism for carbon transport in the formation of filaments is surface diffusion [88, 89]. Baker *et al*. [78] hypothesise that surface diffusion is responsible for the formation of outer skin to the growing bulk filament. It was Baird *et al*. [88] who first suggested that the growth of carbon filament might be due to surface migration of adsorbed 'metal-metal hydrocarbon' across the surface to metal-carbon interface, where these species decompose. This mechanism was elaborated by Oberlin *et al*. [89] and it is illustrated in Fig. 2.13. The 'metal-metal hydrocarbon' species diffuse on the surface and dissociate at the contact angle between metal and the substrate, and the carbon shell is formed at the contact. New metal hydrocarbon species decompose at its edge and the carbon filament develops by lateral growth while lifting up the catalyst particle. The rear side of the catalyst is protected from surface diffusion by a carbon layer which results in the hollow channel at the centre. Sacco [90] remarked that while this model is interesting, it requires more quantitative evidence before it can be accepted. He suggested that it is likely that surface diffusion of carbon or carbon species is involved, however, the measured activation energy for filament growth (Table 2.2) indicates its contribution to the growth process is small.

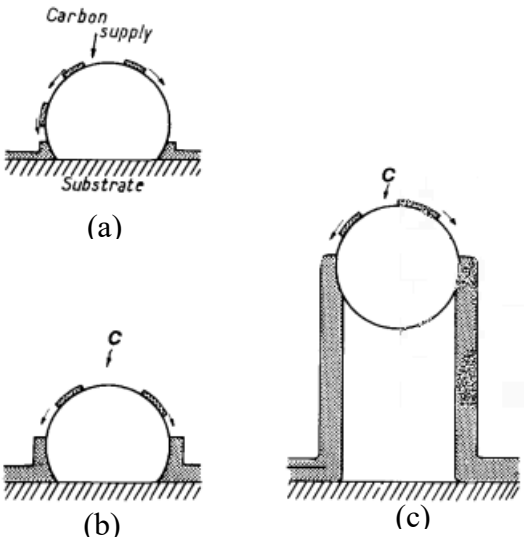

Fig. 2.13: Schematic illustration of the growth mechanism of carbon filament based on surface diffusion *[89]*.

Several workers [5, 77, 91] had initially considered the concept of surface diffusion for filament growth unlikely. Bartholomew [5], and Rostrup-Nielsen and Trimm [77] rejected the surface diffusion mechanism based on the work by Massaro and Petersen [92] who showed that the surface diffusion of carbon on nickel foil does not exist or is negligibly small in the temperature range of 350-700°C.

However, other authors have used this surface diffusion model to explain the growth process of carbon nanotubes [93, 94, 95]. Seidel *et al*. suggested that only surface diffusion of hydrocarbon can explain the fast growth rate of the single-walled carbon nanotube. Hofmann *et al*. [94] and Raty *et al*. [95] performed calculations and simulations, respectively, to show that the surface diffusion of carbon is the most probable diffusion path for nanotube growth. Perhaps, the most compelling evidence of surface diffusion of carbon was provided by Helveg *et al*. [96, 97] in 2004. With the recent advance of *in-situ* high-resolution TEM (HRTEM) technique, they directly observe the formation of the hollow filament (carbon nanotube) from the catalytic reaction between methane and nickel nanoparticles at 536°C at the atomic scale. They observed that the filament growth is promoted by the reaction-induced reshaping of the particle at its tip, from spherical to elongated and back. This elongation-

contraction process continued in a periodic manner during the filament growth. In its elongated form, the particle appears to act as a template, assisting in the alignment of graphene layers into the tubular structure as carbon atoms diffuse across its surface. A detailed study of the HRTEM movies/images showed that the nucleation and growth of graphene layers occur at single-atom step-edges that are present at the particle surface. This single-atom step-edges are formed spontaneously. A graphene layer is formed between the pair of step-edges and the layer grows as the steps move concurrently towards the end and vanish. This author concluded that this step-edge assisted graphene growth would involve surface transport of carbon and nickel atoms. This growth mechanism is illustrated in Fig. 2.14. Furthermore, this mechanism is supported by density functional theory calculation [97]. This study clearly demonstrated that surface diffusion alone suffices to explain the observed tubular filament growth, however, it is likely that bulk transport may play an important role in a different scenario. Otherwise, it would be difficult to explain the observed similarity between activation energies for filament growth and for carbon diffusion through bulk metals, Table 2.2.

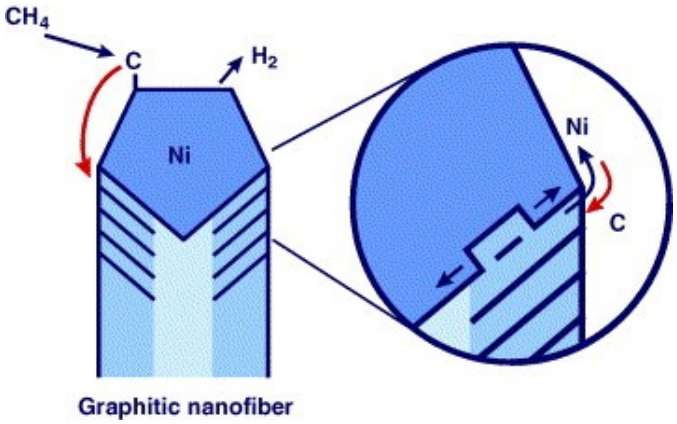

Fig. 2.14: Illustration of the growth mechanism for graphitic nanofibers formed by methane decomposition over nickel nanocrystals. The illustration highlights the surface transport of carbon and nickel atoms and the spontaneous Ni step-edge formation at the graphene-Ni interface *[97]*.

2.3.3. The Nature of the Catalyst

It is known that the transition metals catalytically decompose carbon monoxide and hydrocarbons to produce free carbon. Iron, nickel, and cobalt [98, 99, 86] have been identified as metals with the highest catalytic activity towards carbon formation. The former two metals are the major components of fuel-clad alloy, along with chromium. The catalytic activities of these three elements are discussed below.

2.3.1.1. Chromium

Of all three major alloying elements, chromium is the least catalytically active [86] and hence, there is only very little literature on this metal as a catalyst. On the study of the catalytic decomposition of carbon monoxide on nine single crystals, Kehrer and Leidheiser [98] reported that chromium does not show appreciable catalytic activity at the temperature range of 400°C-550°C. While Baker *et al*. [66] have observed carbon filament (from acetylene) catalysed by chromium, however, the catalytic behaviour of chromium is quite different from Fe and Ni. The filamentous carbon did not form until 800°C and the growth mode involved extrusion of filament from the metal particle that remains in contact with the substrate (root/base growth).

Several workers have shown that the oxidised chromium is catalytically inactive [100, 101, 102, 103, 104, 12]. Chromium, which is added to the stainless steel to protect the alloy from oxidation, can also prevent the catastrophic carbon deposition by forming inert chromia: For example, the oxidation of the 20Cr/25Ni stainless steel at 800°C for 2 hours in H_2/H_2O (50/1) produced chromium-rich oxide which inhibited the catalytic carbon deposition when exposed to CO_2/CH_4 (3/1) [101]. In their study of carbon deposition from acetone during oxidation, Durbin and Castle [103] concluded that the carbon can only be deposited in Cr-rich alloy when the hydrocarbon can penetrate the protective Cr_2O_3 layer via cracks and pores or by mechanical damage of the layer.

2.3.1.2. Iron and Nickel

Considerable work has been done to study the role of iron and nickel on catalytic decomposition of carbon monoxide and hydrocarbon, and the subsequent carbon deposition. While iron and nickel are efficient catalysts, however, the nature of the catalyst is a debatable one. Some workers suggested that the active catalytic phase is metallic [66, 105, 106, 79, 78, 107], while others claim it to be various carbides [89, 108, 109, 68, 110] and, to a lesser extent, oxides [111, 112]. This confusion over the state of the catalyst is aided by the diverse nature of systems under which the work was carried out. It may be possible that a different state is active under different conditions.

Although in the original bulk diffusion mechanism [66, 78], Baker *et al*. have never explicitly stated or confirmed the identity of the catalyst. It was implied that the active phase was metallic. The justification for this is provided by the observed correlation between activation energies for filament growth and for solid state diffusion of carbon through the respective metals.

Manning and Reid [79] studied the carbon deposition from gas mixtures containing CO, H_2, H_2O, CO_2 and CH_4 on an iron catalyst. They concluded that the carbon deposition only occurs when (a) carbon is thermodynamically favourable, and (b) the gas composition is such that the metallic iron is the stable phase, and not the iron oxides (Fe_3O_4) or carbides (Fe_3C) as neither catalyse the carbon deposition reaction. However, in another paper, Manning *et al*. [62] suggested carbon is deposited as a metastable carbide intermediate which decomposes to free metal and carbon. Tibbetts *et al*. [91, 113] have derived a model on the growth of carbon filaments from methane decomposition on iron. It was assumed that the catalytic particle was austenitic iron supersaturated with carbon.

Lin with co-workers [114] used *in-situ* ultra-high vacuum TEM to observe the growth of carbon nanotubes on a nickel particle from acetylene decomposition at 650°C. They used a selected area diffraction pattern to identify the state of catalyst both before and during the growth. It was found that the catalyst Ni particles remain metallic during growth. A similar observation was reported by Hofmann *et al*. [115] They used atomic-scale environmental TEM and *in-situ* time-resolved X-ray photoelectron spectroscopy (XPS) technique to observe the growth of carbon nanotube on a nickel catalyst from C_2H_2. HRTEM and XPS analysis showed that the catalyst was active in its metallic state.

Several workers have also identified metallic iron as an active catalyst for the formation of filamentous carbon in a phenomenon known as '*metal dusting'* [105, 116, 117, 118]. The theory of metal dusting involving Fe-based alloy can be described as follows: under the condition of high carbon activity ($a_c > 1$), metal is oversaturated with dissolved carbon, followed by formation of (metastable) carbide (Fe_3C) layer. Graphite is deposited on the surface of carbide which initiates the decomposition of the carbide into graphite and metal particle. Finally, further carbon is deposition in the form of filaments catalysed by the metal particles. Although nickel and Ni-based alloy are also susceptible to metal dusting [119], a different mechanism is involved where the metastable intermediate carbide does not form. Instead, the graphite directly grows into the alloy that is saturated with carbon. This leads to the disintegration of alloy into small metal particles which catalyse the filamentary growth of carbon.

Using in-situ TEM technique, Baker *et al*. [120] had directly demonstrated that the Fe_3C is not an active catalyst for the formation of carbon filament from ethane and acetylene. Turkdogan and Vinters [121] and Walker *et al*. [122] found that the carbon deposition from CO decomposition ceased when most of the iron was converted to cementite. Thus, they credited metallic iron as active catalyst and cementite were considered inactive in

dissociating CO. This observation was consistent with the work performed by Chatterjee and Das [123] who claimed that carbon was deposited only on metallic iron, and not on carbide when CO was passed over it. Furthermore, they claimed that carbon was deposited when the carbide was reduced in hydrogen (which produce iron powder) prior to the exposure in CO. A Similar conclusion was made for hydrocarbon (benzene) decomposition by Yang and Yang [124] who demonstrated that the surface of cementite was essentially inactive; however, in the presence of hydrogen, high activity was achieved because a metallic surface was maintained.

In contrast, others have claimed that carbide does play an active role on filamentous carbon deposition either as bulk carbide [89, 108, 109, 68] or *surface carbide* [72, 125, 126]. Oberlin *et al*. [89] had identified the particle at the filament tip as Fe_3C. Similarly, Sacco *et al*. [73] reported that filament growth occurred only in the thermodynamic region where the Fe_3C is the stable phase. Kock *et al*. [71] claimed that high iron intermediate carbide (ϵ-Fe_2C, ϵ'-$Fe_{2.2}C$) contents are a *prerequisite* for the nucleation of carbon filament. They suggested that filament grows by continuing formation and decomposition of these metastable carbide intermediate. Cementite was also formed; however, it was stable and it was considered to be an inactive by-product. Several authors [127, 128, 129, 130] studying nanotubes, have reported the formation of intermediate metastable carbide (including Fe_3C) and its subsequent decomposition prior to the growth of the nanotube. This has led Ni *et al.* [130] to consider the decomposition of intermediate carbides as elementary steps of carbon nanotube synthesis. Kharlamova [131] has written an excellent review of the intermediate carbide and the other aspects of the growth of CNT.

Originally, in (iron) metal dusting, catalytic particles in filamentous carbon were identified as (iron) metallic. However, using electron diffraction technique, Toh and his co-worker [132, 133] showed that along with metallic phase particle, the catalytic particles in metal dusting

could also be carbides. They studied the role of carbide on a metal dusting of iron-based alloy in CO-26H_2-6H_2O mixture. While the metal dusting proceeded via unstable intermediate metal carbide M_3C (M = Fe, Ni), the identity of the particle located at the filament tip varied with the alloy composition: these were shown to be Fe_3C for Fe/25Cr, Fe/25Cr/2.5Ni and Fe/25Cr/5Ni, and a mixture of austenite (Fe/Ni) and $(Fe, Ni)_3C$ in Fe/25Cr/10Ni and Fe/25Cr/25Ni. Bradley *et al*. [134] have also identified the filament catalyst particles as both metallic and carbide. Using an electron diffraction technique, they have identified $(Fe, Cr)_{23}C_6$ and γ-iron as the catalyst particle when pyrolysis of natural gas (~97% methane) occurred in stainless steel and plain carbon steel tube, respectively. While the particles found on the filament tips during metal dusting of iron or iron-based alloys can be both metallic and carbidic, however, in the case of a metal dusting of nickel, only metallic nickel particles were identified [135]. This is because nickel carbide is highly unstable compared to iron carbide.

With regards to this confusion over the identity of the catalyst particle, Baker and Harris [136] have warned that using room temperature analytical procedures to identify the nature of particle can be complicated if cooling-induced phase transformation of the particles has occurred. This concern was also echoed by Tibbetts *et al*. [113] who suggested that the carbide particles that were identified as a catalyst by others [73, 89] could be formed when supersaturated austenite particles are cooled. Thus, subsequent *post-mortem* analysis does not necessarily identify the active phase. Furthermore, they reasoned that it would be hard to explain the observed growth rate of filament based on the low diffusivity of carbon (about 10^{-4} of that in Fe [137]) in Fe_3C.

However, using *in-situ* environmental high-resolution TEM, Yoshida *et al*. [138] have directly observed the nucleation and growth process of CNTs from Fe_3C nanoparticles. Furthermore, based on their atomic-scale observation, they suggested that the carbon atom migrates via bulk diffusion through the carbide.

As an alternate to bulk carbide, surface carbide has been suggested to play a role in carbon formation and some authors [58] considered it to be less controversial than bulk carbide. Based on the experimental observation that carbon formed in a region where cementite is thermodynamically stable and literature survey suggesting cementite as inactive phase, Sacco *et al*. [73] speculated that catalyst might exist as two-phase metal-carbide. Alstrup [72] proposed a similar model where a 'surface carbide' is formed on the leading face of catalyst, at which the surface reaction takes place to produce carbon for filament growth. Bianchini and Lund [125] further expanded the notion of surface carbide. They claimed that the formation of surface carbide depends on the carbon activity of the gas phase. At low carbon activity, a_c (gas phase) < a_c (surface carbide), at which the surface carbide cannot form thermodynamically, the catalyst particle is composed of a single phase, Fig. 2.15 (a). However, at higher carbon activity of the gas phase, the catalyst is composed of surface carbide and bulk phase, shown in Fig. 2.15 (b), as suggested by Alstrup. The apparent support for surface carbide mechanism was provided by Bonnet *et al*. [126] who studied the metal dusting on reduced iron and iron oxide in 30%iC_4H_{10}-30%H_2-40%Ar. They found that the catalytic particle in the filaments tips was composed of surface carbides (Fe_3C and Fe_2C) and bulk metallic iron.

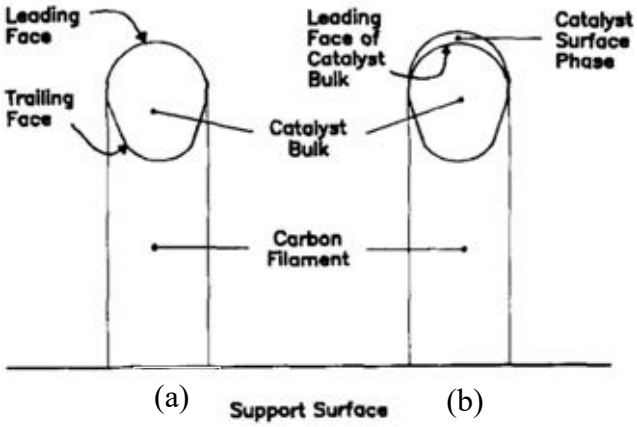

Fig. 2.15: Schematic representation of two different morphology of the catalyst particle in carbon filaments. (a) For low gas phase a_c, the particle is single phase throughout, whereas (b) for high a_c, a thin surface carbide is present on the leading face of the catalyst separating the bulk of the catalyst from direct contact with the gas atmosphere *[125]*.

In these models (surface carbide), the rate-determining step for filament growth is the diffusion of carbon through the bulk catalyst, however, a concentration gradient is considered as the driving force for diffusion. This is discussed in section 2.3.4.

Although there are few reports of oxide being an active catalyst [111, 112] however, it is generally accepted that an oxide scale, if thermodynamically stable, is inactive and can retard carbon deposition. Wolf and Grabke [139] have measured the solubility of carbon in the various oxides, including FeO and Fe_3O_4 and found it to be negligible (immeasurably low, < 0.01 ppm even at 1000°C). At this level, carbon cannot diffuse significantly in iron oxides and thus, it cannot act as nucleation sites for carbon filaments [86]. However, under reducing and carburising environment, iron oxide plays a significant role as *precursors* in carbon deposition.

Baker *et al*. [120] studied the catalytic reactivity of Fe (metallic), FeO and Fe_2O_3 precursors for the formation of filamentous carbon from ethane and acetylene. They concluded that the order of activity is FeO > Fe ~ Fe_2O_3. It was suggested that the extremely high catalytic activity of FeO could be attributed to the formation of the iron-rich sponge-like region on the

surface i.e., FeO acts as a precursor for *in situ* formation of high surface area Fe catalyst. Furthermore, small metallic particles are formed from the FeO precursor that leads to rapid filamentous carbon formation. In comparison, the metallic particle formed from the Fe_2O_3 is much larger. This leads to the growth of the small number of wider carbon filament at a slower rate. A similar result was found by Tokura *et al*. [140]who studied carbon deposition on the preoxidised iron sample in 15%CH_4-H_2 gas atmosphere. Heavy carbon deposition was observed. The deposition increased with longer preoxidation of samples. It was interpreted by the formation of an active ‘’metallic’’ surface obtained by the reduction of oxide scale in the CH_4-H_2 gas mixture. Likewise, Seturbaut *et al*. [141, 142] investigated the carbon deposition on Fe-Ni-Cr alloy under cycling oxidising-reducing conditions. They showed that the carbon deposition was due to the reduction of Fe-Cr-Ni spinel which was formed in the oxidising environment. The carbon deposition increased with repeated oxidation and reduction that produce more, finer (Fe, Ni) particles.

2.3.4. Bulk Diffusion Mechanism: Driving Force

2.3.4.1. Temperature Gradient

Table 2.3: Variation of filamentous carbon yield with various hydrocarbons *[143]*.

Hydrocarbon	Enthalpy (at 730°C)	Carbon Filament yield relative to that from Acetylene
Ethylene	-9.21	0.01
Benzene (with H2 as carrier gas)	-14.82	0.03
1-3 Butadiene	-22.74	0.10
Allene	-43.23	0.16
Methyl Acetylene	-41.53	0.59
Acetylene	-53.29	1.00

In their original mechanism, Baker and his co-workers [78, 66] had suggested that the driving force of the bulk diffusion of carbon through the metal particle is the temperature gradient

created by the exothermic decomposition of acetylene and endothermic precipitation of carbon. Furthermore, they measured the carbon deposition rate from various unsaturated hydrocarbon/cobalt systems [143]. The deposition rate increased in the same order as the exothermicity of the hydrocarbon decomposition reaction. This is shown in Table 2.3. This temperature driven force on carbon diffusion is challenged by the work of many authors [67, 88, 99] who had shown that carbon can be deposited from the hydrocarbon that decomposes by an endothermic reaction.

Direct evidence for the temperature-driven carbon diffusion mechanism was provided by Yang and Yang [144, 145]. They exposed two-dimensional thin nickel films (400 Å) at 700°C to methane, *n*-hexane, benzene and toluene, respectively. It was found that the carbon formed from methane and *n*-hexane (*endothermic*) was deposited on the front, exposed face, whereas, for the *exothermic* decomposition of benzene and toluene, the carbon was deposited at the rear, non-exposed face. This finding was interpreted as confirmation of temperature-driven carbon diffusion.

To explain the observed filament growth from endothermic decomposition on catalyst particles, Yang and Chen [74] suggested that heat is transferred to the surroundings of the gas/catalyst interface by radiation, thus compensating for the endothermic reaction. With this hypothesis, the condition for *exothermality* is made redundant.

Two other possible explanation has been proposed to explain the formation of filamentous carbon from the endothermic decomposition of hydrocarbon (such as methane and propane). Robertson [146] suggested that carbon formation during endothermic decomposition of methane should be credited to the exothermic decomposition of impurities of hydrocarbon. A similar conclusion was made by Evans *et al*. [147] who showed that the formation of filamentary carbon from the pyrolysis of methane depends on the purity of the gas. They

reported that the carbon filaments were formed from commercial grade methane, but not with high purity methane at a temperature below 900°C.

The other explanation was proposed by Keep *et al*. [148] who studied the decomposition of propane (*endothermic*) over nickel. It was found that the filamentous carbon is formed by the exothermic decomposition of intermediate products ethylene, propylene and benzene which are formed from the pyrolysis of propane. The major by-product, methane, did not contribute to carbon deposition. A similar reasoning was used by Baker *et al*. [120] to account for the formation of carbon filament from ethane decomposition. Here, ethylene was suggested as the decomposition product of ethane that gave rise to the filamentary carbon.

2.3.4.2. Concentration Gradient

Table 2.4 shows the list of enthalpies for carbon forming reactions, including endothermic decomposition reaction. This has led several authors to propose concentration-driven diffusion mechanisms.

Rostrup-Nielsen and Trimm [77] suggested that there is a difference in carbon activities (and hence, the solubilities) at the metal/gas interface and at the metal/carbon interface. This activity/solubility difference creates a carbon concentration gradient across the particle that acts as a driving force for the diffusion. A similar conclusion was made by Snoeck *et al*. [76] and Tibbetts *et al*. [113]. Furthermore, Tibbetts *et al*. calculated the temperature gradient across a nanoparticle of less than 10^{-5} K. Such negligible temperature difference are unlikely to drive the carbon diffusion. They reported at least a 1 K temperature difference is needed for diffusion. Instead, they suggested and supported by calculation, that the supersaturation of carbon at the gas/metal interface would be able to create a concentration gradient required for the diffusion of carbon.

Table 2.4: Enthalpies of Reaction for Carbon-Forming Reactions *[77]*.

Reaction	ΔH° (kcal/mol); temp (K):		
	600	800	1000
$CH_4 \rightarrow C + 2H_2$	+19.90	+20.82	+21.43
$C_2H_2 \rightarrow 2C + H_2$	-53.9	-53.6	-53.3
$C_2H_4 \rightarrow 2C + 2H_2$	-10.60	-9.8	-7.2
$C_3H_6 \rightarrow 3C + 3H_2$	-2.00	-0.7	-0.3
Butene-1	+3.7	+5.1	+5.95
cis-Butene-2	+5.82	+7.48	+8.45
trans-Butene-2	+6.38	+7.89	+8.73
$CO \rightarrow C + 1/2\ O_2$	+26.330	+26.512	+26.768
$2CO \rightarrow C + CO_2$	-43.34	-44.85	-46.42

The driving force due to supersaturation has been questioned by some authors [74, 144, 90]. Yang and Chen [74] reviewed the literature and noted that the carbon filament growth seems to occur on all transition metals whereas supersaturation does not.

Alternatively, carbon gradient due to (surface) carbide formation has been proposed. Sacco *et al*. [73] have observed that the carbon filament from CO only formed considerably in a region where the formation of carbide (Fe_3C) was thermodynamically favoured. They also noted that Baker *et al*. [120] have shown that the Fe_3C particles were catalytically inactive for the growth of filamentous carbon from acetylene. Based on these two observations with apparent disagreement, they speculated that either Fe_3C is inactive towards decomposition of acetylene, however, active towards CO decomposition, or the catalyst has two-phase Fe_3C/α-iron and the mass flux is driven as the result of difference in solubility of carbon at the α-iron/Fe_3C interface and α-iron/filament interface.

In a series of articles on the thermodynamics, mechanism and the morphology of filamentous carbon formed from CO and CH_4 on iron and nickel, de Bokx *et al*. [70], Kock *et al.* [71] and Boellaard *et al*. [149] suggested that metastable carbide (ϵ-Fe_2C and ϵ'-$Fe_{2.2}C$) are continuously formed and decomposed during filament growth. They suggested that the

catalyst is a single carbide phase (e.g. Fig. 2.15 (a)) with a nonhomogeneous composition such that the carbon concentration in the carbide increases towards the gas/particle interface (i.e. leading face). This non-stoichiometric carbide establishes the carbon gradient required for bulk diffusion.

However, Alstrup [72] suggested that the unstable carbides observed by previous authors [70, 71, 149] are not bulk but surface carbide (Fig. 2.15 (b)). Based on the kinetic results for the formation of carbon filament and the results from the literature, Alstrup proposed a model where a surface carbide is formed on the leading face of the catalyst. The carbon atoms produced by the surface adsorption-decomposition reaction diffuses rapidly through the carbide, fixing the carbon concentration just below this carbide layer. This creates the concentration gradient that causes the migration of carbon atoms to the rear end of the particle.

The survey of the literature suggests that there is a case 'for' and 'against' for both temperature and concentration-driven diffusion of carbon through the catalyst, with the latter being more favourable. It is likely that a combination of both mechanisms is involved in the actual process.

2.3.5. Effect of Surface Structure on Carbon Deposition

Previous studies [150, 151, 152, 153, 154] have shown that the catalytic activity of metals on carbon deposition is dependent on the crystal planes exposure. LaCava et al. [150] showed that the carbon deposition from benzene is preferentially deposited on {111} planes of nickel. Similar results were reported on the catalytic decomposition of CO on Ni [151, 152, 153, 154]. The extent of carbon deposition on Ni followed the following order in decreasing preference

$$\{111\} > \{110\} > \{100\}.$$

Using the selected area electron diffraction (SAD) technique on carbon filaments formed on Ni, Yang and Chen [74] showed the existence of {111}, {311} and {220} planes at the graphite/metal interfaces. Furthermore, they performed extended Huckel molecular orbital (EHMO) calculations to provide information on the epitaxial relationship between graphite and different Ni planes. The calculation showed that the {111} planes provide the strongest binding to graphite and hence are the most stable for binding with graphene.

EHMO calculations were also performed to determine the relative catalytic activities of these four Ni faces for the decomposition of CO. The degree of activation follows the order

$$\{110\} > \{100\} > \{111\} > \{311\}.$$

This calculation is consistent with the experimental observation of decomposition of methane on various Ni faces: Ni{110} was more active for decomposition of CH_4 than {100} and no activity was shown by {111} [155].

Blakely and others [156, 157] have studied the precipitation of carbon from a solid solution of carbon in metal as it is cooled. They have observed that as graphite precipitate at saturation temperature, the underlying Ni surfaces reconstructed to primarily {111} and {311} faces to provide epitaxial fits with the {0001} graphite plane. Based on this result and their own results on TEM-SAD and EHMO calculations, Yang and Chen [74] suggested that the faceting of the metal particles is likely caused by the surface reconstruction upon graphite precipitation.

While it is clear that Ni{111} is the most active face for carbon deposition, Grenga and Lawless [153] and Presland and Walker [158] showed that topographical imperfection such as surface kinks and steps were the preferred sites for nucleation. Furthermore, on the study of carbon on Ni surfaces, Dost et al. [159] have observed that nucleation sites for carbon were found to be associated with stepped surfaces vicinal to the {111} and {110}. After extensive

carbon deposition, these regions were completely covered by carbon while the {100} plane and vicinal surfaces remained free of such deposits.

The importance of the steps sites in atomic scale was shown by DFT calculations [160] and confirmed by in-situ HRTEM observations of carbon nanotube growth [96, 97]. DFT calculations [160] showed that adsorbed atomic carbon has much higher stability at the steps than at the terraces. As a result, step sites are more favourable for graphene nucleation than the terraces. The HRTEM study [96] revealed that the nucleation and growth of graphene layers occurred at the single-atom step-edges at the nickel surface. These single-atom step-edges are formed spontaneously. A graphene layer is formed between the pair of step-edges and the layer grows as the steps move concurrently towards the end and vanish. This is illustrated in Fig. 2.16. Furthermore, on the study of graphene nucleation on Ni(111) surface using quantum chemical molecular dynamics (QM/MD) simulations, Wang and others [161] have shown that in the absence of a step-edge defect, the nucleating graphene precursor will actively transform the Ni surface to form one.

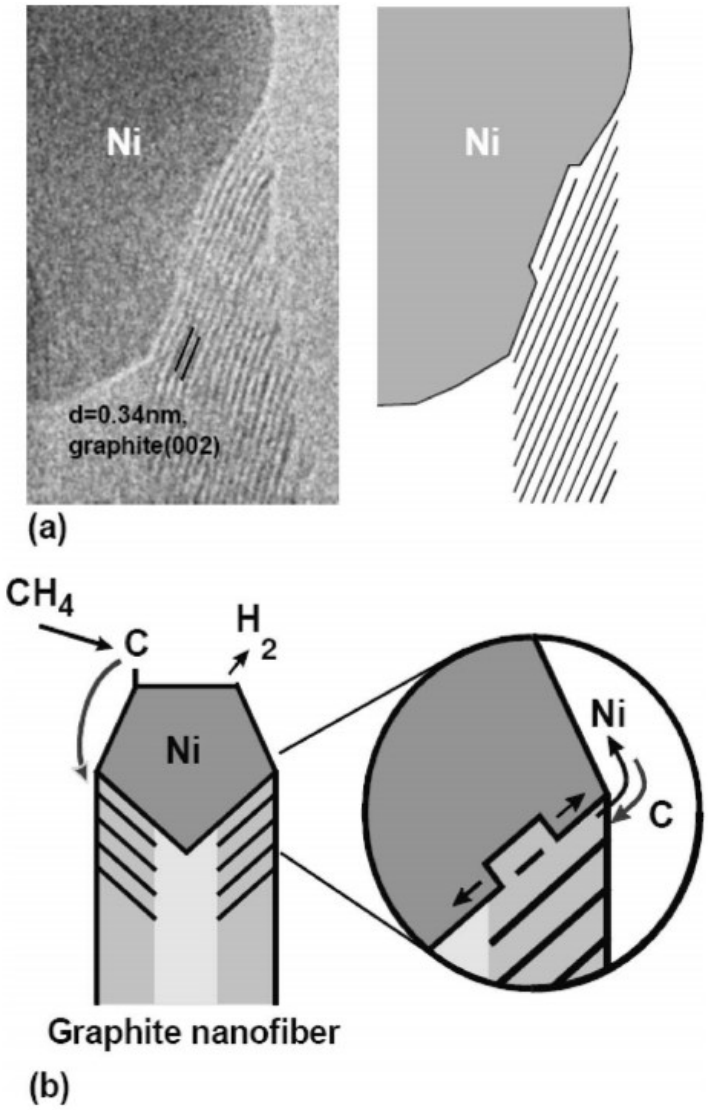

Fig. 2.16: (a) (left) In situ high-resolution transmission electron microscopy image, obtained during carbon nanofiber growth, showing the interface between the nickel nanoparticle and the carbon whisker and (right) schematic presentation of the graphene-nickel interface specifying the growth of a graphene layer between monoatomic Ni step sites at the nickel surface. (b) Illustration of the growth mechanism for carbon nanofibers established from the interplay of in situ HRTEM observations and DFT calculations *[162]* (adapted from *[96]*).

2.4. Carbon Deposition on AGR Fuel Clad

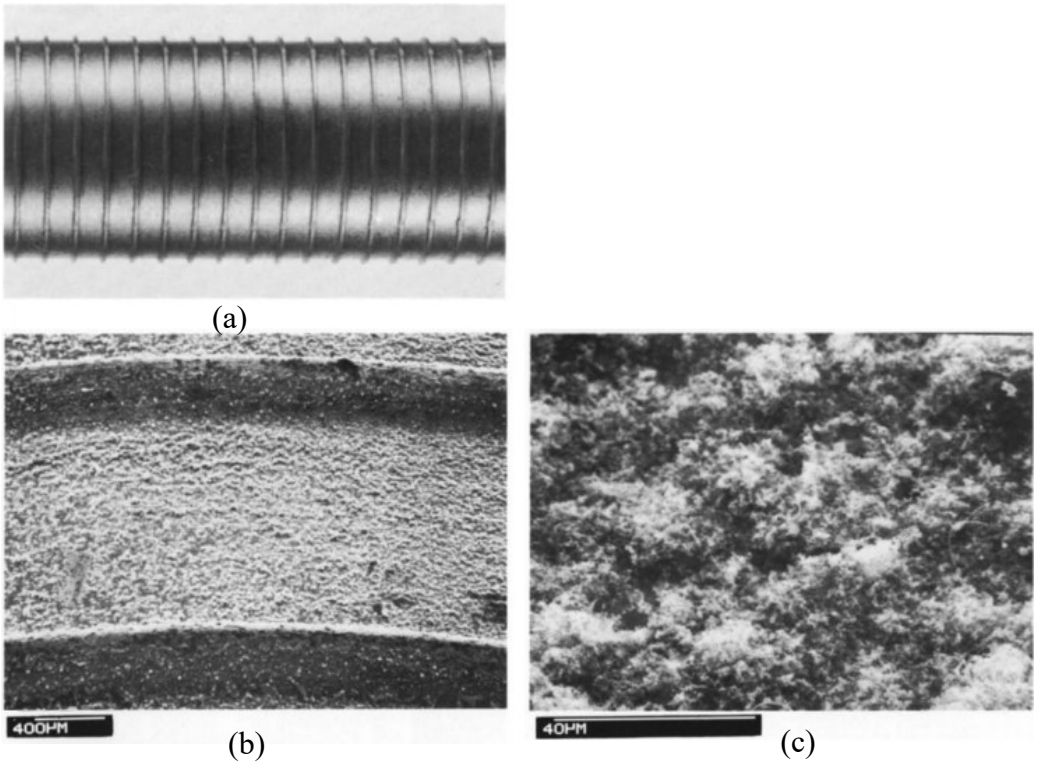

Fig. 2.17: Carbonaceous deposition from simulated AGR coolant. (a) Virgin cladding; (b) nodular deposit formed on fuel clad surface and ribs by irradiation in gamma facility, (c) filamentous microstructure of deposit *[163]*.

The UK's Advanced Gas-Cooled Reactors (AGR) are graphite moderated and carbon dioxide cooled nuclear reactors. Carbon dioxide was selected as a coolant as it has good heat transfer properties, low neutron capture cross-section, stable under radiation and it is cheap and readily available [164]. Under intense radiation, CO_2 decomposes to give carbon monoxide and other oxidising species "O" that are highly reactive [10, 11]

$$CO_2 \xrightarrow{\text{irradiation}} CO + \text{"O"} \quad \text{(Radiolysis)} \tag{2}$$

Usually, these dissociated products would recombine quickly (hence, its stability towards radiation)

$$CO + \text{"O"} \longrightarrow CO_2 \qquad \text{(Recombination)} \tag{3}$$

However, it is possible for "O" (produced near graphite) to escape recombination and reach the graphite surface (C_g) where it will oxidise the surface of the moderator, $C(O)$

$$C_g + "O" \longrightarrow C(O) \quad \text{(Graphite Surface Reaction)} \qquad (4)$$

The surface oxide will eventually form gaseous CO resulting in the weight loss of the graphite [165]. Since the moderators are not designed to be replaced, the oxidation of graphite must be minimal so that the lifetime of the moderator, and hence the lifetime of the reactor can be maximised.

Radiation-induced oxidation of graphite can be suppressed by CO (which is formed by graphite oxidation and radiolysis of CO_2) by competing with graphite for oxidising species. In AGR, a small concentration of CO (0.9% to 1.2%) is allowed to build up. To inhibit the radiolytic oxidation of graphite much higher concentration is needed, however, this would result in the excessive carbon deposition on the hot metal surface (such as the fuel clad or boiler surface) via the Boudouard reaction

$$2CO \longrightarrow CO_2 + C \quad \text{(Boudouard reaction)} \qquad (5)$$

Further protection to the graphite is provided by the addition of methane which deposits carbon (via radiolysis disintegration of methane) on the graphite surface that acts as 'sacrificial carbon layer' [166]. However, radiolytic decomposition of methane can lead to undesirable carbon deposition on the surface of the fuel clad (and boiler tubes) [167], Fig. 2.17. Thus, a balance must be made between the beneficial effect of the inhibitor (CO, CH_4) on the graphite and the detrimental effect of carbon deposition.

2.4.1. Irradiation Studies on Carbon Deposition on AGR Fuel Clad

Several small-scale irradiation rig experiments were carried out in the 1970s. The experience and the knowledge acquired led to the development of prototype AGR at Windscale (WAGR)

and the results obtained from the prototype were fed to the commercial AGRs (CAGR). Campion [167] has reviewed the series of irradiation works on carbon deposition reaction on fuel clad at small-scale and prototype AGRs. Some of the important results are highlighted below.

DMTR 7H1 loop [168]

- Carbon deposition on fuel clad from $CH_4/CO/CO_2$ coolants mix was a result of the radiation-induced process.
- For the CH_4 concentration of the order of 1000 ppm, carbon deposition only occurred when the CO concentration was at or above 2.5%.

CEGB Berkeley gamma irradiation source [169]

- There was evidence for deposit arising from surface catalysis, producing a filamentous carbon.
- The deposition rate was primarily related to methane concentration.
- Deposition apparently occurred via radiolytic decomposition of ethylene (C_2H_4) which was formed from the destruction of CH_4.
- Deposition potential (a) from methane was highest at high [CH_4] and low but non-zero [CO], and (b) from CO at high [CO] and high [CH_4].

Dido 6V3 loops [170]

- The deposition was via surface catalysis; deposits were largely filamentary.
- Deposition arose from a gaseous deposit precursor, which was derived from methane. A chemical model was developed which identified ethene as the precursor.

Windscale AGR large loops [167]

- No deposition was observed below 4% [CO], however, very rapid deposition occurred at and above this concentration.

Windscale AGR small loops [167]

- The higher deposition rate was observed in these loops than in the reactor.
- This higher rate was attributed to the presence of nickel tetracarbonyl, $Ni(CO)_4$ which were formed during low temperature (shut down) condition in the presence of CO.

AGR Prototype [167]

- The heavy deposition was observed for high CH_4 (700-900 ppm)/1% CO and 350 ppm CH_4/4% CO.
- Deposition ceased when CH_4 was reduced from 350 ppm to 150 ppm in the presence of 4% CO, suggesting that the CH_4 was important to initiate deposition process.

In summary: these irradiation studies indicate that methane is the most important coolant component for *radiation*-induced carbon deposition with filamentary morphology. The deposition was the result of surface catalysis and ethylene, which are formed from the radiolysis of methane, plays the role of gas phase precursor to carbon deposition. The effect of methane on fuel clad deposition is influenced by CO.

2.4.2. Non-Irradiation Studies on Carbon Deposition on 20Cr/25Ni/Nb Steel

2.4.2.1. Earlier Studies: Pre-2001 work

Earlier work on carbon deposition on fuel clad was studied using the decomposition of either hydrocarbons or CO.

Keep *et al*. [100] studied the effect of surface pre-treatment on the growth of carbon on 20Cr/25Ni/Nb from propane. Less carbon was deposited on steel pre-oxidised in oxygen than on untreated steel. It was suggested that chromic oxide was most likely to form on oxygen

treated sample and it is less active, hence giving less deposition than untreated steel. Surprisingly, more carbon was deposited on steel that was preoxidised in CO_2 than that on the previous two samples. It was suggested that the deposition enhancement was probably due to the incorporation of carbon during CO_2 pre-treatment. Furthermore, the gas analysis showed that the propane was decomposed into methane and ethane (saturated), ethene/ethylene, propene and benzene (unsaturated). Only the unsaturated hydrocarbons reacted with steel to produce a carbon deposit. This was in agreement with Baker's exothermic growth model of carbon filament as discussed above.

Bennett *et al*. [171] studied the filamentary carbon deposition on pre-oxidised 20Cr/25Ni/Nb from acetone decomposition. Cementite was formed as by-products. It was suggested that iron was the most active element in promoting deposition, and nickel to a lesser extent. However, the active phase was never identified.

When the steel is exposed to carbon monoxide, carbon can be deposited by the catalysed Boudouard reaction, eq (5). This has been observed by Jepson *et al*. [48] where filamentary carbon was formed on 20Cr/25Ni/Nb that was exposed to CO/CO_2 mixture. It was argued that iron and nickel are unlikely to react with CO to form oxides, and since carbon deposit contains more iron than nickel, it was suggested iron carbide was the catalyst.

In 1987, a series of studies [172, 173, 174, 13] were conducted to investigate the carbon deposition behaviour on 20Cr/25Ni/Nb steel exposed to CO/CO_2, with CO content varying from 2-100%, over the temperature range of 650-850°C. The deposition was filamentary in nature and it was suggested that such filamentary deposition was due to catalytic decomposition of CO (Boudouard reaction). TEM examination of the filaments showed that the particles located at the end of filaments were iron-rich. Based on the thermodynamic calculation, it was suggested that both iron (and nickel) are not expected to oxidise in a high

CO environment (75-100%). It was concluded that the observed carbon deposition was not catalysed by nickel/iron oxides, instead, it was suggested that deposition was catalysed by the metallic iron or iron carbide.

The study [172] also demonstrated that the 20Cr/25Ni/Nb alloy with finer surface grain size possessed higher resistance to carbon deposition. It was suggested that this observation was associated with the rate of formation of a protective chromium oxide layer over the alloy surface. It was argued that the initial chromia was formed on the grain boundary (due to the fast diffusion of chromium to the surface along the boundary), followed by the lateral spread of chromia across the surface. During this transition, the iron-rich grain centres which were left unprotected acted as catalytic sites for carbon deposition. Therefore, coarse surface grain sizes which would achieve late surface protection resulted in poor resistance to carbon deposition.

It was also reported that the resistance to carbon deposition can be enhanced by cold working [174] on the 20Cr/25Ni/Nb alloy, prior to exposure, which promotes chromia formation, or by adding silicon to the alloy [13], which forms a protective silica layer.

2.4.3. Recent Studies: Post-2001 work

The above work [172, 173, 174, 13, 48] was based on a very high CO/CO_2 ratio (i.e., reducing condition) such that iron carbide formation was favoured over iron oxide. However, under AGR conditions, only about 1% of CO is present in the coolant (CO/CO_2 ratio ~ 0.01). This gas composition favours the formation of stable iron oxide over the iron carbide and it is not expected that iron carbide would take part in the observed catalytic deposition process in AGRs.

In the early 2000s, Millward and his co-workers, [12, 14] based on the University of Birmingham, studied the carbon deposition on 20Cr/25Ni/Nb steel using simulated AGR

coolant gas mixtures. These studies were performed by exposing the steel sample to gas mixtures consisting of 1000 ppm C_2H_4/1 vol. % CO/ CO_2 at 550°C. Under this test condition, the high carbon activity ($a_c > 1$) needed for the deposition was obtained from the dissociation reaction of ethylene (C_2H_4). At 1% concentration of CO, the carbon deposition via Boudouard reaction was not expected [172].

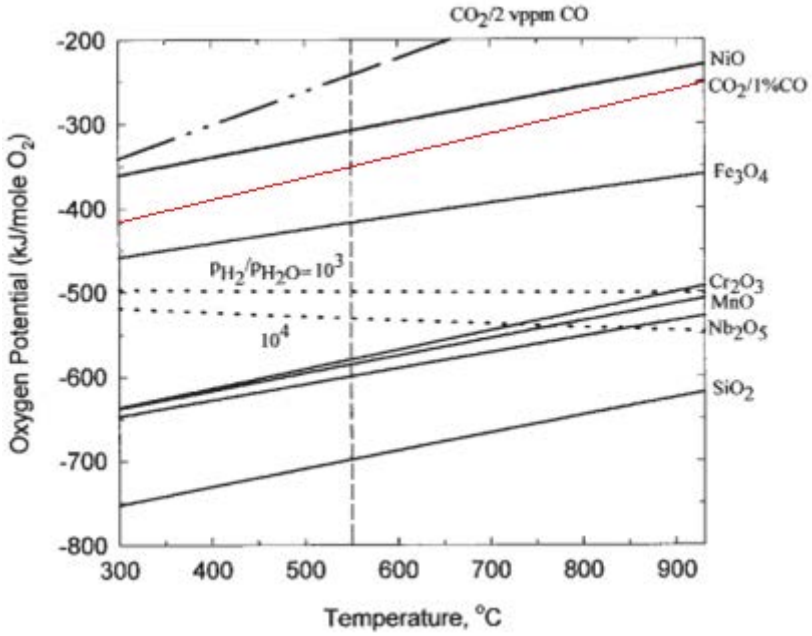

Fig. 2.18: Ellingham diagram for oxide formation. The red line represents the oxygen potential in 1%CO/CO_2 atmosphere at various temperatures. Iron and Chromium are expected to oxidise as the oxygen potential is high enough for the oxides to be stable. For 1%CO in CO_2, oxygen partial pressure is low for NiO to form *[12]*.

The oxygen potential (i.e., oxygen partial pressure) of this mixture was determined by the CO_2/1%CO equilibrium ratio. The corresponding Ellingham diagram for oxide formation is shown in Fig. 2.18. From this, it can be seen that the only metallic phase that can exist under these conditions is nickel, all the other alloying elements including iron and chromium are expected to be oxidised.

After only 1-hour of exposure [12], significant carbon filaments were deposited on the surface of the alloy. Grain boundaries at which a protective chromia was formed were generally free from deposited carbon. Particles of 10-20 nm diameter size were found at the

tip of individual filaments. An example of a filament with catalyst particles is shown in Fig. 2.19. Using high-resolution TEM image and EDS analysis, the particle was identified as metallic nickel. In agreement with the thermodynamics, no carbide was detected. Furthermore, iron-rich and chrome-rich oxide did not catalyse the carbon formation.

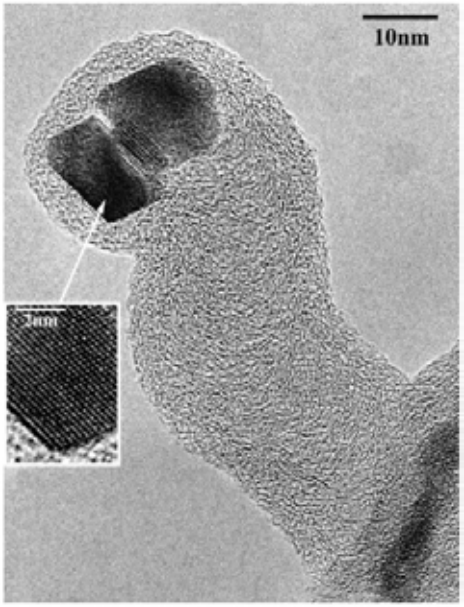

Fig. 2.19: HRTEM micrograph of carbon filament with two nickel particles at its tip *[12]*.

It was postulated that these nickel particles were formed during the early stages of exposures when the protective chromia has not fully formed across the surface and, while iron and chromium were oxidized, nickel was not. This eventually led to the formation of a metallic-nickel nanoparticle within the sub-surface oxide layer. This mechanism is shown schematically in Fig. 2.20. Supporting evidence for this model was provided by HRTEM and EDS analysis of cross-section through the sample, Fig. 2.21. It was suggested that the gas access to this sub-surface nickel particle is possible because of the porous nature of the iron-rich oxide on the surface. Based on these out-of-reactor studies, nickel has been credited as the major metallic species that plays a significant role in the carbon deposition in AGR nuclear reactors.

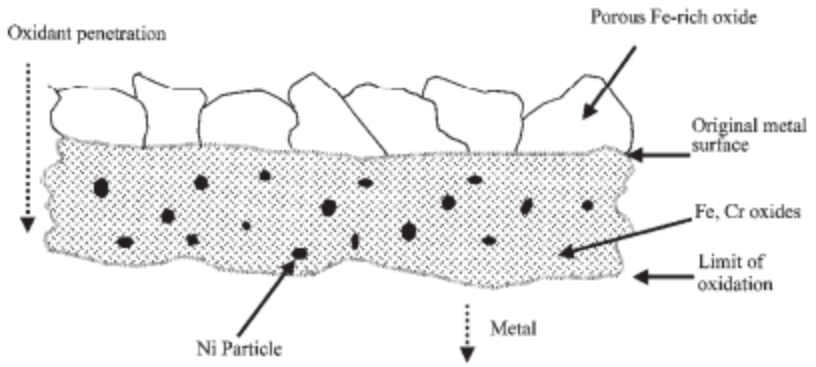

Fig. 2.20: Schematic representation of the mode of nickel nanoparticles *[14]*.

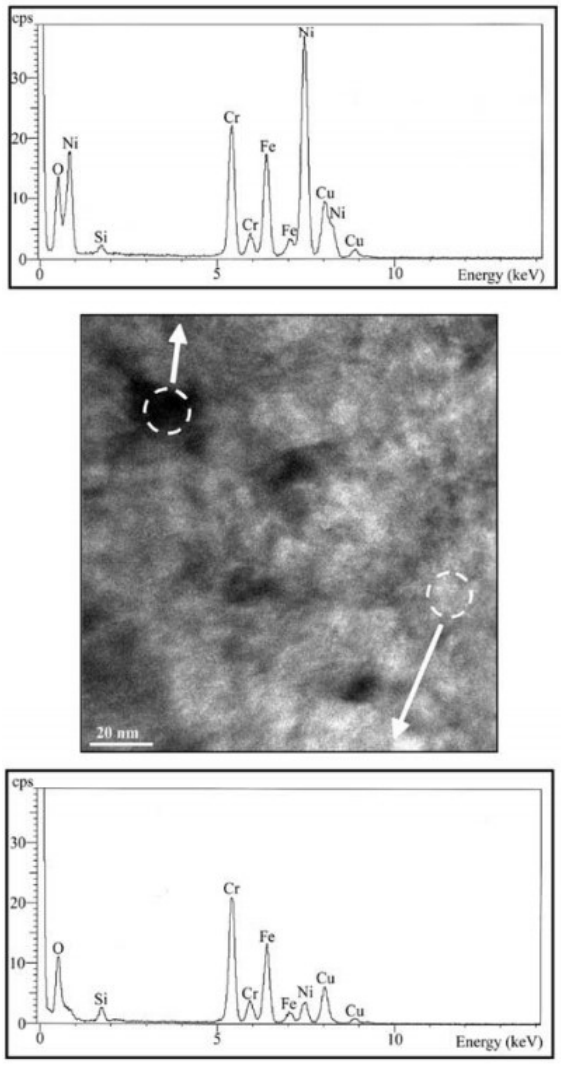

Fig. 2.21: A HREM image of the subsurface zone of a specimen oxidised for 4 hours at 550°C in CO2/1%CO. EDS analysis shows the dark particles to be highly Ni-rich *[14]*.

2.4.2. Morphologies of Deposit Found in AGR Fuel Clad.

The detailed mechanism for fuel-clad deposition in AGR is described in ref. [175]. The summary of the deposition mechanism and deposit characterisation is presented below. The carbonaceous deposit in fuel-clad is classified by thickness and density in three categories: uniform, granular and columnar.

Methane is added to the coolant to prevent the oxidation of the graphite moderator [176]. Under intense gamma radiation, methane decomposes into unsaturated hydrocarbons, primarily into ethylene (C_2H_4) [177] which will decompose further into carbon and hydrogen if the suitable pathway exists. This pathway is provided by the nickel particles, which are formed within the sub-surface oxide layer, because of internal oxidation of fuel-clad in CO/CO_2 (~ ratio 1/99) atmosphere. The iron-rich oxide is porous and allows coolant to reach these nickel particles where unsaturated hydrocarbon decomposes, and filamentous carbon is formed. The deposit is referred to as an intrinsic deposit.

In the presence of the effective catalyst poison, there will be no filamentary growth and the surface of the clad will be covered with *uniform* amorphous carbon, as shown in Fig. 2.22(a). Such deposit has a smooth shiny appearance. Typically, it has less than 10 μm thickness and 0.9-1.8 g cm^{-3} density. This uncatalysed carbon deposit is the result of decomposition of highly unsaturated or radical hydrocarbons.

With no effective catalyst poisoning, the nickel particle facilitates the growth of clumps of filamentary carbon on the surface. However, this filamentary deposition process is limited as the catalyst has a finite life (i.e., deactivated after it is encapsulated by carbon film), and there is the only finite amount of nickel in the sub-surface oxide layer. These filamentary growths and the surrounding clad is, then covered with uncatalysed amorphous carbon. An example is shown in Fig. 2.22(b). Such deposit is composed of grains or nodules with 50-200 um apart

and it is classified as *granular* (sometimes, nodular) deposit. It has a similar density (~ 0.9 g cm^{-3}) to uniform deposit but thicker, typically 10-50 um. Like a uniform deposit, granular deposit also has a smooth shiny appearance. These two types of deposit are also known as an intrinsic deposit.

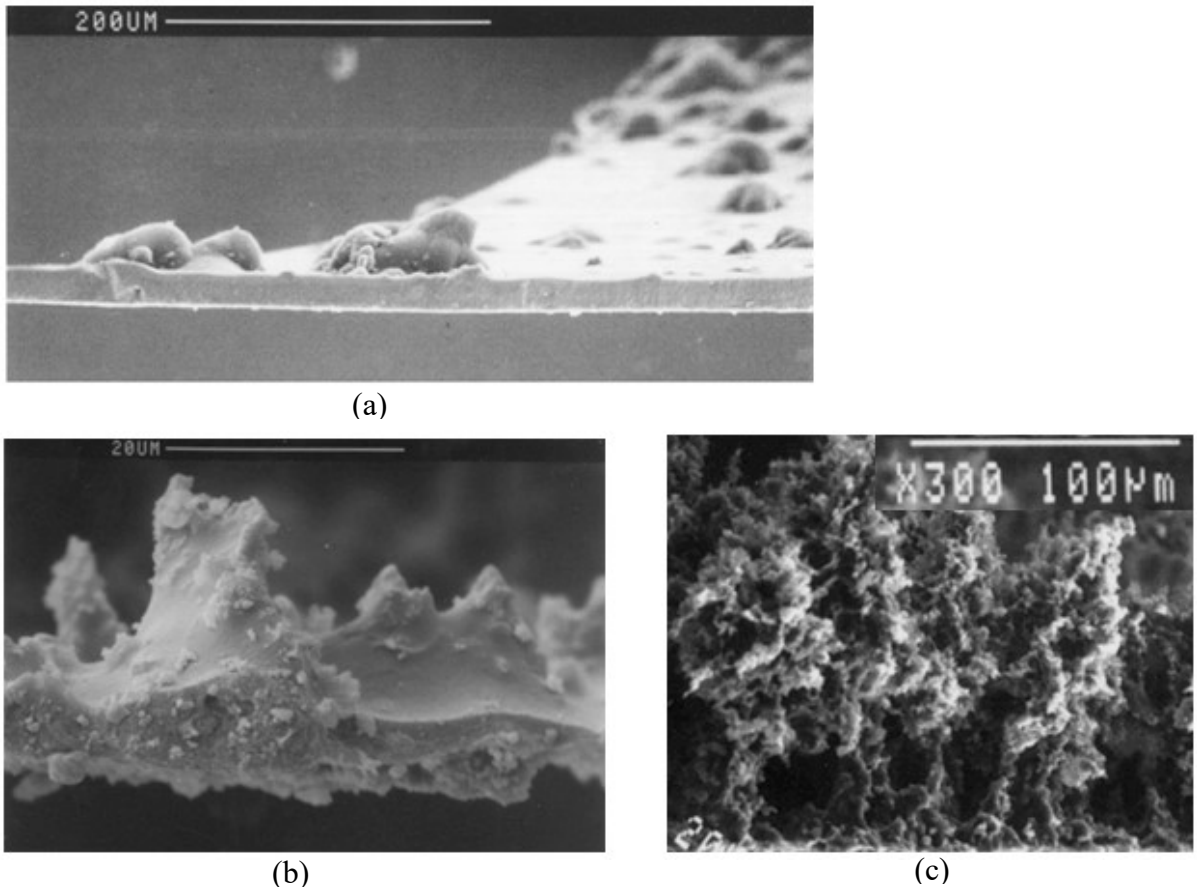

Fig. 2.22: Electron Micrograph of (a) Smooth Deposit: side view of a deposited layer, with occasional grains on top; (b) Granular Deposit and (c) Columnar Deposit: side view of compact columns on top of a thin base layer *[175]*.

In the presence of an external source of nickel, the filamentary deposition process can continue further, giving rise to a third deposit, known as a *columnar* deposit. Gaseous nickel tetracarbonyl, $Ni(CO)_4$, are formed in cool parts of the AGR gas circuit by the interaction between carbon monoxide in coolant and nickel-containing alloys. At higher temperature region, the $Ni(CO)_4$ thermally decomposes and liberates nickel atoms which aggregate on the intrinsically-catalysed deposit to form fine nickel particulates of between 10-100 nm sizes [178]. These fresh nickel particulates then promote further carbon deposition, leading to

branching and expanding mass of deposit, forming *columns*. The columnar growth ends once the nickel supply is terminated.

As this *extrinsically* catalysed deposition continues, the uncatalysed deposition tends to cover the columnar growths, giving it shiny appearance. Columnar deposits that are free from uncatalysed deposition has matt appearance. An example is shown in Fig. 2.22(c). The deposit is, typically, 50-200 um thick and has a density of 0.3-0.7 g cm^{-3}. The columns are 50-200 um apart and can merge together to form a much more complex structure.

From these studies, it is clear that the severe carbonaceous deposit on fuel-clad is the result of the formation of filamentary carbon. As a result, the current work is limited to study the growth mechanism and prevention of filamentous carbon formation.

2.5. Inhibition of Filamentary Carbon Deposition

The work done on inhibition of carbon filament growth on metal surfaces has been driven by the need to prevent the excessive build-up of carbon deposit. Baker *et al*. [81] have studied the possibility of inhibiting filamentous carbon formation by introducing various oxide additives to the catalyst particle such that it might retard the rate of the key steps involved in the growth process, namely carbon solubility and diffusion through the particle. The additives influenced the growth rate of the filament by (a) either, shielding the catalyst towards gas-phase adsorption and decomposition reaction, (b) or by reducing the solubility of carbon in metal and promoting encapsulation and premature deactivation of the catalyst; (c) or, by decreasing the carbon diffusion rate through the catalyst particle.

Vogt *et al*. [179] argued that the growth of carbon filament can be prevented by alloying the active metal (iron and nickel) with a metal (copper and platinum) that are not readily capable of forming a carbide. This was based on the assumption that the formation of intermediate metal carbide is a prerequisite for the growth of carbon filaments. They reviewed the result of

the earlier work where it was observed that the alloying nickel with platinum (above 10 at. %) resulted in the suppression of filament growth [180]. Similarly, when nickel was alloyed with copper the filamentary growth was suppressed [179]. At 30 at. % of copper, almost complete suppression was achieved.

The work done by the Horsley and Cairns [101] has demonstrated that the *prior surface treatment* of the steel before exposing to the gas mixtures of 75% CO_2/ 25% CH_4 at 650°C for 5.5 h has a significant influence on the amount of carbon deposited on the surface of the steel. The 20Cr/25Ni/Nb steel, that was dry annealed in H_2 at 930°C for 1 h, was severely covered with carbon filaments. The amount of carbon deposited on the steel was reduced on a sample that was dry H_2 annealed at 930°C, followed by selective oxidation in 50/1 H_2/H_2O mixtures at 800°C. The unannealed (cold worked) steel was less prone to deposition and the unannealed steel that was selectively oxidised were free from deposition. They concluded that various pre-treatments resulted in a different surface elemental composition that subsequently controlled the extent of deposition; by selectively pre-oxidising steel, a surface which is free from (principal catalyst) iron or nickel is formed and hence, less prone to deposition. In addition to selective oxidation of steel, it is also possible to inhibit carbon deposition by coating steel with inert silica [181].

2.5.1. Effect of Sulphur on Carbon Deposition

Perhaps the most extensively studied method to inhibit carbon deposition in many catalytic processes is the use of sulphur [182, 183, 184, 21, 22]. Karcher and Glaude [182] demonstrated that the addition of SO_2 in $CO/H_2/Ar$ resulted in an immediate inhibition of carbon deposition on iron and steel surfaces. Their study also showed that a short 1-hour pre-treatment of iron (at 500°C) with 500 ppb SO_2/Ar was sufficient to completely suppress the carbon deposition for an extended period (307 hr). This inhibition was explained by the formation of iron sulphide (FeS) that covered the catalyst surface.

A study [80] of the effect of sulphur on steam reforming of methane showed that the inhibition for the carbon deposition on nickel could be achieved if about 70% sulphur coverage ($\theta_s > 0.7$) on nickel (adsorption) was achieved. At this coverage, while the carbon formation was eliminated, the steam reforming reaction continued. This was explained by assuming that a large number of catalytic sites were required for the nucleation of carbon filament than for the steam reforming reaction.

Bennett *et al*. [22] studied the effect of sulphur poisoning on catalytic carbon deposition on pre-oxidised 20Cr25NiNb steel due to decomposition of acetone at 600 °C and 700 °C. Two approaches were considered: Surface pre-treatment, where the oxidised (in CO_2 for 1000 h at either 600 or 700°C) steel was sulphided by H_2S, either, for 24h at room temperature or, for 1 h at 600-625°C; The second approach was to use various sulphur compounds (thiophene, H_2S, SO_2 and COS) which would be adsorbed on the catalytic sites that are preferred for acetone decomposition. Under the condition used in that work, iron was the primary catalyst.

Initially, sulphiding ($Fe_{1-N}S$) in H_2S reduced the deposition by a factor of 4-560 less than that with untreated steel. However, the protection was lost on extended exposure. It was suggested that loss of protection was not caused by sulphur removal, but due to the generation of new active sites. Gas phase poison also inhibited carbon deposition by their preferential adsorption on catalytically active sites. The organic sulphide, thiophene (C_4H_4S) was found to be more effective, possibly due to its larger molecular size blocking several adjacent active sites.

A similar result was found by Tan and Baker [21] who showed that in the range of 25-250 ppm range, organic sulphide (dimethyl sulphide - CH_3SCH_3 and dimethyl disulphide - CH_3SSCH_3) suppressed the carbon deposition process on Fe-Ni particles from ethane. In contrast, under the identical condition, H_2S was found to promote carbon deposition.

This effective poisoning of organic sulphide on various catalysts has been investigated on various catalytic reactions, other than carbon deposition. For example, in hydrogenation reactions on Pt and Ni catalyst, Maxted and Evans [185] found the relative toxicities increases with molecular size: H_2S < CS_2 < thiophene (C_4H_4S). Curtis and Baker [186] found that dimethyl disulphide, t-butyl mercaptan and n-propyl sulphide was more effective poisoning than thiophene for hydrogenation of 1-hexene on Pt.

From the above studies, it can be seen that the sulphur can deactivate the catalyst either by converting active catalyst (metallic or carbide) into inert sulphide (e.g. FeS, Ni_3S_2) or by poisoning via adsorption. Inhibition of carbon deposition by bulk sulphiding is only possible in a system with high-sulphur content, whereas for low-sulphur content (in the range of ppm), inhibition of deposition is interpreted in term of sulphur adsorption on the metal surface [187].

Various sulphur compounds (including H_2S, COS, SO_2, thiophene, CS_2) have been known to poison the catalyst. These compounds have unshared electron pairs which can lead to very strong chemisorption on the metal surface. Typically, the adsorption on the surface is dissociative, leaving a strongly bonded sulphur atoms to the surface [187]. There are two ways by which sulphur can poison the catalyst: blockage of catalytic active surface sites (geometric effect) [188, 189], and by altering the catalytic activity of the metal caused by strong metal-sulphur interaction (electronic effect) [190, 191, 192]. The geometric effect dominates in high-sulphur coverage, whereas the electronic effect is important at low coverage. At low coverage, single sulphur adatom can poison more than four metal surface atoms (electronic effect) and at high coverage, sulphur atom blocks about two catalytic sites per adsorbed sulphur atom.

Another aspect found with the effect of sulphur on the catalyst is the possibility of reconstruction or faceting of the metal surfaces [187]. This phenomenon has been used to explain the apparent enhancement of carbon deposition when sulphur was introduced to the system. It has been shown that both pre-treatment or continuous addition of 5-150 ppm H_2S to cobalt, nickel and iron-nickel particles undergoing reaction with ethylene and ethane has a drastic increase in the amount of carbon deposition [183, 184, 21]. It is assumed that at low-level sulphur coverage a strong metal-sulphur interaction weakens the bonding between the surface and next lower metal layer, allowing for reconstruction of the metal surface to the one that favours adsorption-decomposition reaction of hydrocarbon. Gardner and Bartholomew [193] has also observed an increase in the rate of carbon formation on sulphur-poisoned nickel particles from the methanation of CO. It was suggested that the sulphur has a higher tendency to poison the dissociative adsorption of H_2 than dissociative adsorption of CO, thereby preventing the hydrogenation of surface carbon and increasing the rate of carbon formation.

2.5.2. Inhibition of Carbon Deposition on AGR Fuel Cladding by COS.

In AGR gas circuit, carbonyl sulphide (COS) arises naturally from both impurities in the core graphite and oil ingress [194]. In addition, COS is directly injected in AGR to maintain the concentration of around 100 ppb [175].

Millward *et al*. [15] study the effect of COS on filamentary carbon deposition on 20Cr/25Ni/Nb steel. The study showed that the addition of 240 ppb COS at 550°C to the gas mixture (1000 ppm C_2H_4/ 1 % CO/ CO_2) that was known to deposit carbon [12] led to a sharp decrease in the amount of carbon deposited. The inhibition continued even after the COS-containing gas mixtures was replaced by COS free mixtures with high carbon activity. This latter finding suggested that the inhibition effect was due to the surface modification by the COS rather than the changes in gas phase kinetics. The study concluded that, because of the

porous nature of the oxide layer, COS mixtures interacted directly with the metallic nickel particles to deactivate their catalytic properties. It was suggested that the nature of Ni-S interaction was sulphur adsorption on nickel particles.

Recently, Taylor *et al.* [20] studied the effect of concentration of COS and temperature on carbon deposition on Si-free 20Cr25NiNb stabilised steel. The samples were exposed for 4 hours to gas mixtures containing 1000 ppm C_2H_4/ 1 % CO / CO_2 with COS concentrations between 0-1460 vpb at 500-725°C. It was found that with no COS addition in ethylene (C_2H_4) bearing gas carbon filaments were observed over the temperature range of 550-700°C. No carbon filament was formed at 500°C. This was attributed to slow oxidation kinetics with insufficient time for a catalyst to form. With COS addition to the reactant carbon deposition was suppressed and, in some cases, (higher COS concentration), complete inhibition was achieved. Furthermore, as the temperature increased, the COS concentration required for complete inhibition also increased. For example: at 600°C, complete inhibition was achieved at 234 ppb COS, whereas at 650°C and 675°C, COS concentration of 513 ppb and 1460 ppb was required, respectively. The inhibition effect of COS was attributed to the poisoning of the nickel catalyst surface by sulphur adsorption.

2.6. Thermodynamics of Ni-COS System

McGurk [195] has considered the thermodynamics of Ni-S interaction and proposed a model to measure the effectiveness of COS for inhibiting carbon deposition.

2.6.1. Bulk-Sulphiding

Ni_3S_2 is the most stable species that can be formed from metallic nickel and gaseous sulphur [187]. It was originally considered that high levels of COS would deactivate the nickel catalyst by converting nickel into nickel sulphide. However, under AGR conditions thermodynamic consideration for the reaction

$$COS + 1.5Ni \rightarrow 0.5Ni_3S_2 + CO \quad (6)$$

showed [195] that, at *best estimate*, the equilibrium COS concentration was too high (150-570 vpb) for a temperatures range of 450-580°C to explain the inhibition effect of [COS] at ~ 100 ppb in an AGR. Furthermore, the fraction of Ni that would react with 100 ppb COS to form Ni_3S_2 was calculated to be as low as 0.01. It was concluded that the inhibition effect of COS observed in the reactor cannot be explained by the formation of Ni_3S_2 on its own. Inhibition was most likely to be, at least in part, due to the adsorption of sulphur on the nickel particle surface.

2.6.2. Adsorption Model

For sulphur adsorption, a simple approximate model was proposed [29] where two competing surface adsorption processes on nickel were considered:

$$COS + Ni\ (surface) = CO + S_a, \qquad (Sulphur\ adsorption) \quad (7)$$

$$CO_2 + Ni\ (surface) = CO + O_a, \qquad (Oxygen\ adsorption) \quad (8)$$

S_a and O_a are the adsorbed sulphur and oxygen atom.

Based on the Langmuir-Hinshelwood approach, the following expression of fractional surface coverage of sulphur, θ_S was derived (Appendix A)

$$\theta_S = \frac{K_S[COS]}{K_S[COS] + K_O + [CO]} \quad (9)$$

where the concentrations are in ppb. The equilibrium constant for sulphur K_S and oxygen adsorption K_O were given by

$$K_S = 3.17 \times \exp\left(\frac{18380}{T}\right) \quad (10)$$

$$K_O = 13 \times \exp\left(\frac{-3127}{T}\right) \quad (11)$$

It was assumed that $\theta_S = 0.8$ was required to inhibit carbon deposition over the 450-580°C temperature range. Then for 1% CO, the above expressions (9) predicted that inhibition would occur at less than 1 ppb COS. This value is substantially less than the plant observations.

The expression (10) for K_S was originally derived using the S-Ni binding energy of 462 kJ/mol which in-turn was derived from the adsorption enthalpy of reaction (at 500 °C)

$$H_2S + \text{Ni (surface)} = H_2 + S_a \quad (12)$$

where S_a is an adsorbed sulphur.

It was argued that the discrepancy in the calculated COS concentrations and the plant observation arises because the above model does not consider the fact that sulphur binding energy decreases with increasing sulphur coverage. This is due to the electrostatic repulsion that exists between co-adsorbed sulphur atoms. Furthermore, increasing the sulphur coverages will modify the electronic structure of the surface Ni atoms, which result in the decrease in the adsorption energy (weaker bonding) [196].

To agree with the plant observation (inhibition with 100 ppb COS), the expression for K_S was revised to

$$K_S = 3.17 \times \exp\left(\frac{13000}{T}\right) \quad (13)$$

which was equivalent to a reduction in sulphur binding energy by 45 kJ/mol.

The assumption of 80% sulphur coverage is arbitrary, and no justification was provided. However, Rostrup-Nielsen [80] has shown that at 70% coverage, inhibition for the carbon deposition on nickel is achieved. Based on this finding, the assumption of 80% coverage can be considered reasonable in the above model.

Table 2.5: Comparison of experimentally observed result with predictions from both bulk-sulphiding and surface poisoning *[16]*.

	Temperature (°C) up to which inhibition occurs for a given [COS]		
COS (ppb)	**Experimental value** [20]	**Bulk-Thermodynamics, (Best Estimate)**	**Adsorption Model**
113	550-600	460	584
234	600-650	505	618
513	650-700	557	659

Table 2.5 [16] compares the maximum temperature, up to which inhibition occurs for a given COS concentration, obtained with the bulk thermodynamic and adsorption model predictions with an approximate experimental value inferred from Taylor *et al* [20]. Clearly, the bulk-thermodynamics calculation underestimates the temperature at which inhibition can occur for a given COS concentration. However, the prediction from the adsorption model is in line with the experimental data.

2.7. Sulphur Speciation in AGR coolant

The above adsorption model and thermodynamic calculations assume that COS is the only sulphur species that exist in the gas phase in AGRs i.e., [COS] ~ [S]. However, other forms of sulphur species including H_2S and SO_2 are known to exist. Recently [16], further evidence has been provided from the reactor measurements of total sulphur and COS concentration. It was found that the average [S]/ [COS] ratio is 1.22 which strongly suggest the existence of other forms of sulphur species. Thermodynamic calculation suggests that COS and H_2S are the most prevalent sulphur species [17]. Other sulphur species such as SO_2, CS_2, HS, H_2S_2, S_2 and CH_3SH are also likely to exist in trace amounts [18, 19].

3. Aims

While the role played by metallic nickel has been correctly identified, however, these catalyst particles has not been fully characterised. This is particularly true for the nickel-rich particles embedded within the oxide layer.

To explain the role played by sulphur in deactivating nickel particles from catalysing carbon filament growth, two possible mechanisms [15] have been suggested, namely bulk sulphiding and surface poisoning by sulphur adsorption. However, no experimental evidence supporting either mechanism has been obtained previously [15]. The previous study relied on characterisation techniques such as scanning electron microscopy (SEM) which however was not able to analyse the chemical information of the individual nickel-rich particles due to their small sizes.

Furthermore, as mentioned above (section 2.7.) various forms of sulphur compounds can exist in the AGR reactor. As discussed in section 2.5.1. the amount of carbon deposition suppressed by sulphur depends not only on the concentration but also on the chemical nature of the sulphur species. It is important therefore to understand the influence of other sulphur species on the catalytic properties of a nickel catalyst.

The aims of the current work are:

(a) To characterise and study the mechanism on the formation of nickel-rich particles in 20Cr/25Ni/Nb steel.
(b) To improve the understanding of the inhibiting role of sulphur on the carbon deposition: to identify the distribution of sulphur within the steel.
(c) To examine the effect of different sulphur compounds (COS, H_2S and CH_3SH) on the catalytic behaviour of nickel-rich particles.

Hydrogen sulphide was selected because, besides COS, H_2S is the most dominant sulphur compound that can exist in the reactor and methanethiol (CH_3SH) was chosen because the complex organic sulphide (larger molecular size) has been known to be more effective poison than the simpler sulphur compound like H_2S, COS and CS_2.

The work will be carried out at 600°C which is an intermediate fuel clad temperature in AGR and, with around 200 ppb of the sulphur compound.

4. Experimental

4.1. Material: 20Cr-25Ni Nb Stabilised Stainless Steel

The alloy used in this work was 20Cr/25Ni/Nb steel with the nominal composition shown in Table 4.1. Previously [12] it was shown that the standard 20Cr/25Ni alloy with 0.56 wt % Si had a tendency to retard the carbon deposition. As a result, silicon free alloy was selected for the current work to study the retardation effect on the carbon deposition process due to the addition of sulphur compounds to the deposition gas.

Table 4.1: Alloy Composition, wt. %.

Cr	Ni	Mn	Nb	C	Fe
19.0	26.5	0.67	0.6	0.051	Bal.

4.2 Sample Preparation

The alloy was available as cold-worked 0.4 mm thick sheet. Rectangular samples with dimensions of approximately 10 mm x 20 mm were cut out and glued to an aluminium stub so that it was easier to hold during grinding and polishing of the samples. The material of 50 – 100 µm thick was removed from the surface by grinding with wet silicon carbide abrasive paper with grit the sizes of 240, 400, 800 and 1200 successively. This was followed by polishing with 6 µm and 1 µm diamond paste and final finishing with an oxide polishing (colloidal silica). The polished samples were detached from the aluminium stub by dissolving the glue in acetone and finally, cleaned with ethanol.

Along with these rectangular samples, several discs of 3 mm diameter were also prepared: An as-received sample was mechanically thinned down to less than 0.2 mm using coarse silicon carbide paper (either 120 or 240 grit) and then discs of 3 mm diameter were punched, and subsequently annealed (see section 4.3.) at 930 °C. These annealed discs were electro-

polished using a Struers Tenupol twin-jet electro-polishing unit until perforation in an electrolyte containing 10 % perchloric ($HClO_4$) acid in ethanol (C_2H_6O) at -5 to -20 °C and 12 V. The polished discs were thoroughly cleaned with ethanol and were later used for carbon deposition and direct TEM analysis to study any carbon filaments formation at the surface of the specimen near the hole without the need for any further sample preparation.

4.3. Heat Treatment

After the final polish of the bulk rectangular samples and mechanical grinding of 3 mm discs, the samples were annealed at 930 °C for half an hour in a reducing atmosphere (5% H_2 in Ar) to achieve a uniform surface grain size of approximately 13 µm. During this stage, the samples were wrapped in a tantalum foil to prevent any oxidation that might occur due to the presence of residual oxygen. Fig. 4.1 shows an SEM image of the typical microstructure of the surface of (a) the rectangular sample and (b) TEM disc following the heat treatment. Annealing twins are a common feature in these heat-treated samples. The particles present on the surface were identified as chromium-manganese oxide and niobium carbide. These particles were present on the sample prior to the heat treatment stage. No oxygen peak was found on the EDS spectrum collected from the 216 µm by 170 µm area, Fig. 4.2, which suggests that the oxygen partial pressure was low enough (also the protection provided by tantalum) to prevent oxidation of the samples. The smooth surface of the TEM disc is the result of electro-polishing after the heat treatment.

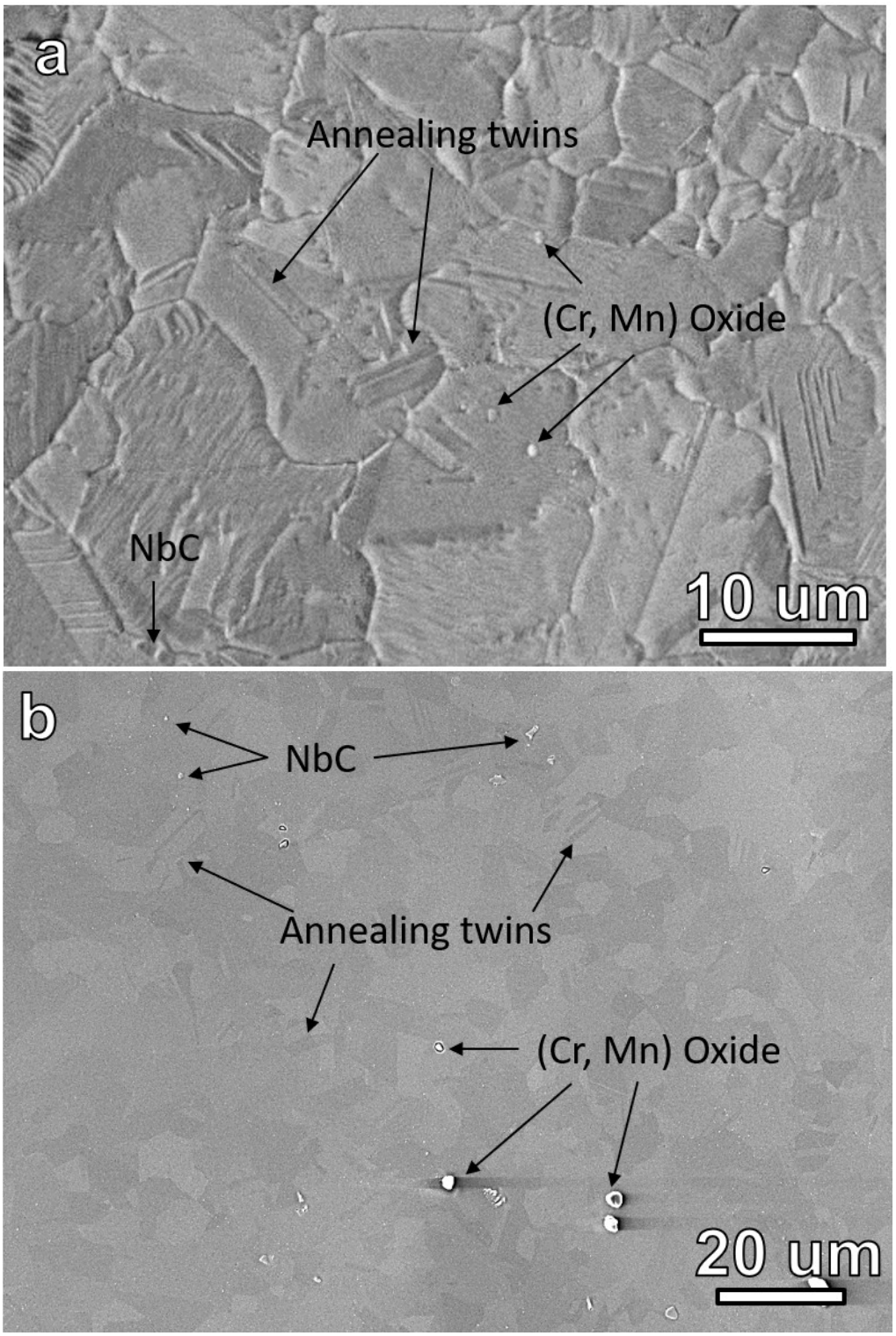

Fig. 4.1: SEM images obtained from the surface of samples after the annealing at 930 °C for 30 mins. (a) Bulk-Rectangular Sample. (b) Twin-jet polished TEM disc. Cr-Mn oxide and NbC were found on both samples. These particles were present in the alloy prior to the heat-treatment.

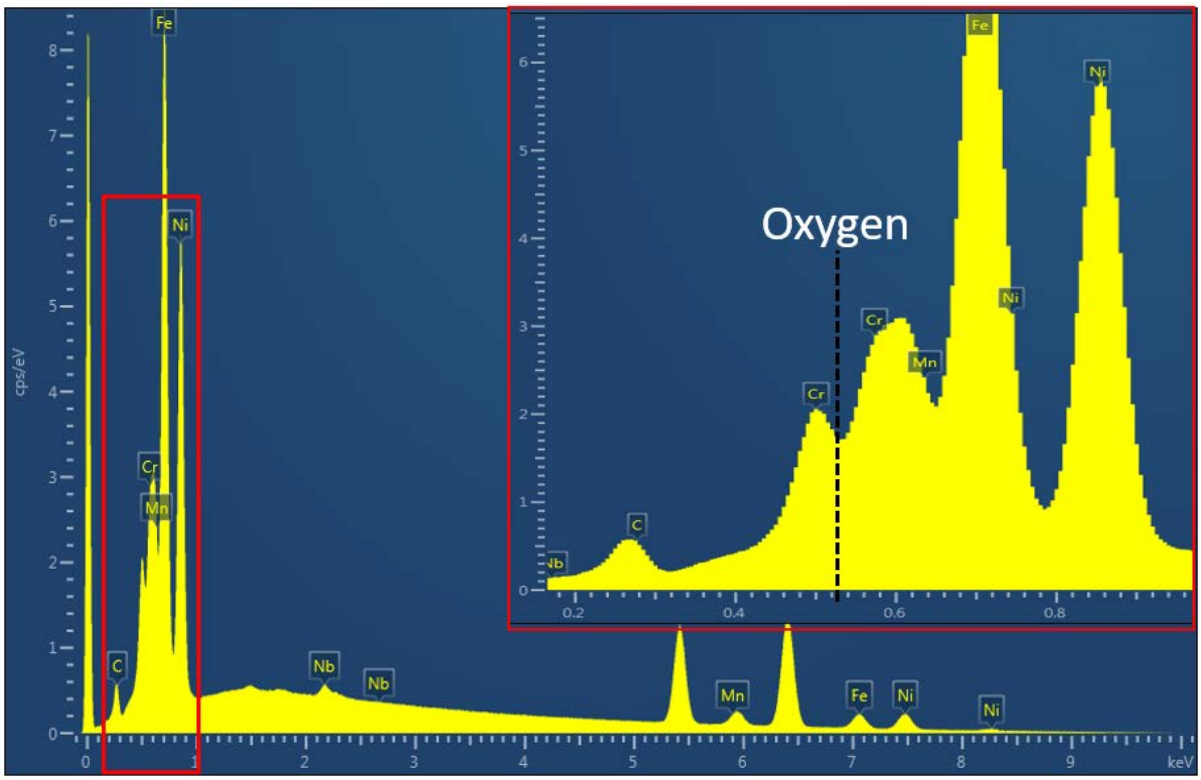

Fig. 4.2: EDS spectrum collected from the heat-treated rectangular sample. No oxygen peak was found. Inset: zoom-in view of the spectrum from the highlighted red box, showing the location of an oxygen peak if it existed.

4.4. Deposition Experimental Procedure

As illustrated in Fig. 4.3, the test rig system used for this study consists of two horizontal furnaces connected in series and connected with two gas bottles, one was an inert gas with 5% H_2 in Argon and the other was a deposition gas mixture bottle. Each furnace has a cool zone and a hot zone. Cool zones are located at each end of the furnace and the hot zone is located at the centre. During the experiment, the central hot zone of the treatment furnace was held at 600 °C, while the end zones were maintained at less than 200 °C. The specimens were placed in an alumina boat, as shown in Fig. 4.4, and transferred to the front-end (cool zone) of the treatment furnace. Ar gas (containing 5% H_2) was used to purge through for 2 hours. The pre-treatment furnace where clean titanium foils were stacked as the oxygen getter, was then heated up to 700°C at 20°C per minute and maintained at this temperature for 20 minutes. While maintaining the 5%H_2/Ar gas flow, the treatment furnace was then heated up

at 25°C per minute to 600 °C and maintained for 20 minutes. Using the Fe-Cr wire attached to the alumina boat, the samples were moved to the central hot zone. The 5% H_2/Ar gas flow was stopped, and the selected deposition gas mixture bottle was switched on and this marked the start of the deposition experiment. After 4 hours, the treatment furnace was switched off and the samples were moved to the rear-end (cool zone) of the treatment furnace and left to cool for 10 min. The gas supply was then switched back to the 5% H_2/Ar. One hour later the pre-treatment furnace was also switched off, and the rig system was cooled overnight to room temperature under the inert gas. The sample was taken out from the furnace in the following morning for analysis.

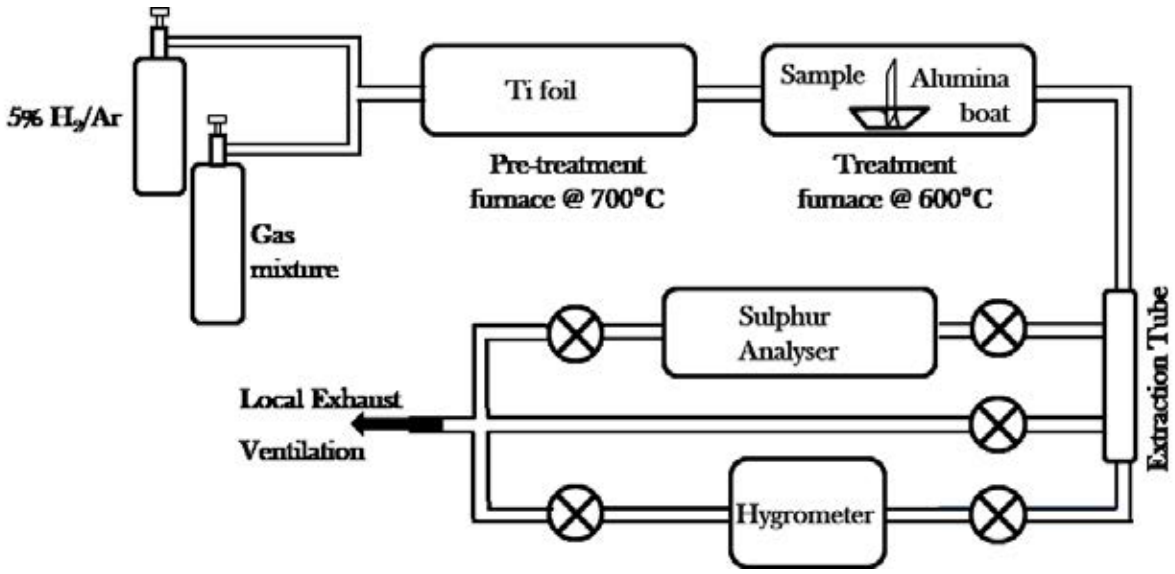

Fig. 4.3: Schematic diagram of the furnace rig system.

During the experiment, the gas flow rate was maintained at 0.5 Litre /min for the inert gas and 1 Litre/min for the deposition gas. The test was operated at atmospheric pressure. When the inert gas was following through the rig the moisture content of the system was monitored by using a Vaisala hygrometer which was installed in series after the treatment furnace. With the help of the fitted valve, it was possible to avoid the hygrometer when the gas was switched to the deposition gas to avoid damaging it.

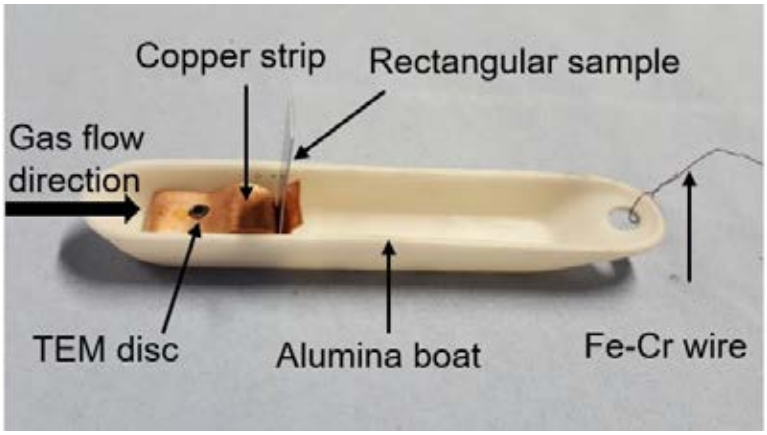

Fig. 4.4: Alumina boat with the rectangular sample and 3 mm TEM disc.

4.5. Dew Point

During the purging and cooling stage with 5%H_2/Ar, the partial pressure of oxygen P_{O_2} will be dominated by the following reaction:

$$2H_2 + O_2 = 2H_2O \qquad (14)$$

When the treatment furnace was at 600°C, the dew point (DP) was in the range of -69°C to -35°C. For the reaction (14) the partial pressure of oxygen at temperature T in K is given by the following formula [197]:

$$1/2\log_{10}P_{O_2} = 3.00 - 13088/T + \log_{10}\left(P_{sat-H_2O}/P_{H_2}\right) \qquad (15)$$

where P_{sat-H_2O} is the saturation vapour pressure of water and P_{H_2} is the partial pressure of H_2. The partial pressure of water vapour can be calculated using the following formula [198]

$$\log_{10}P_{sat-H_2O} = 9.80\frac{DP}{273.8 + DP} - 2.22 \qquad \text{for } DP \leq 0℃ \qquad (16)$$

For 5% H_2/Ar in 1 atmospheric pressure, $P_{H_2} = 0.05$ atm. Thus, using equation (15) and (16) the oxygen partial pressure for given dew points was obtained in the range of 10^{-47} to 10^{-42} atm. At this range of oxygen partial pressure, none of the major elements (Fe, Cr and Ni) will oxidise [199].

4.6. Sulphur Analyser

The sulphur content of the deposition gas (with a sulphur compound) was monitored using the T108 Total Sulphur analyser, supplied by Teledyne Technologies. The setup of the instrument in the rig system is shown in Fig. 4.3. This instrument was used only during the 4 hours deposition period.

The analyser is designed to measure the mixed sulphur concentration (known as Total Sulphur, TS) in the air or CO_2 carrier gas. The model T108 consists of a T100 SO_2 analyser and a M501TS thermal oxidiser. The sample gas (in this case, deposition gas) is directed into the analyser (T108) where the gas is mixed with air which acts as the source of oxygen. The mixture is then passed on to the thermal oxidiser (M501TS) where the sulphur compounds are heated at 1000°C and oxidised into SO_2. The mixture is then sent back to the analyser where it is exposed to ultraviolet light which causes SO_2 to excite and subsequently decay into the lower ground state by fluorescence. The analyser measures the amount of the fluorescence and converts it to the amount of SO_2 (i.e., Total Sulphur) present in the sample gas.

Since the T100 analyser is designed to measure SO_2, it is possible to measure only the SO_2 content by by-passing the converter.

The calibration of the instrument was done with high purity (CP Grade) CO_2 gas for zero calibration and with deposition gas with the known amount (certified value) of sulphur compound for span calibration. Since the conversion efficiency of the different sulphur species into SO_2 is different, for deposition tests with different sulphur species (COS, H_2S and CH_3SH), the instrument is calibrated with the same carrier gas as used in the test.

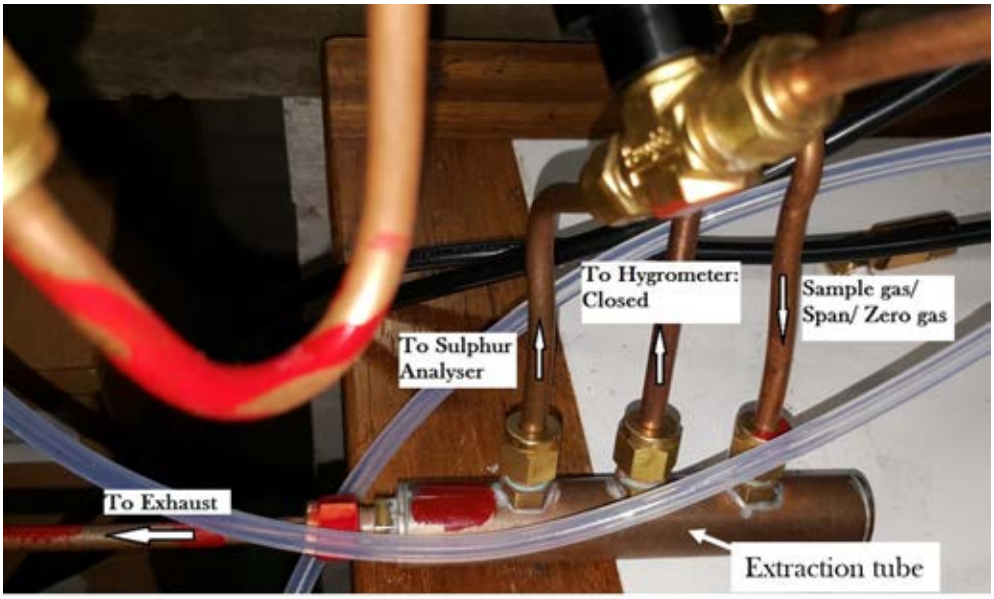

Fig. 4.5: Extraction junction with three outlets connecting with a hygrometer, sulphur analyser and LEV. During the deposition stage, the outlet to hygrometer is closed.

The early test showed that the instrument is very sensitive to the flow rate of the gas. Increasing the flow rate will give higher Total Sulphur reading. While collecting the data it is important to keep the flow rate the same as the flow rate that was used during the calibration of the analyser. This is achieved by passing the gas into the extraction junction (Fig. 4.5) before it is passed to the analyser. The extraction junction has three outlets connecting to the analyser, hygrometer and to the local exhaust ventilation (LEV) system. During the deposition stage, the outlet to the hygrometer is closed while the other two outlets remain open. The internal pump inside the analyser will draw the required amount of gas into the analyser and the remaining gas is sent to the LEV. This way the problem associated with the flow rate can be mitigated.

The instrument was connected remotely to an external computer for data logging purposes using *APIcom* software which can be downloaded from [200]. The software runs on 32-bit Microsoft Window XP or older operating system.

4.7. Deposition gases

Table 4.2: Composition of the deposition gas as supplied by BOC.

Gas mixture	C_2H_4 ppm	CO %	COS ppb	H_2S ppb	CH_3SH ppb	CO_2
1	1045	0.96	-	-	-	Bal.
2	1048	0.99	215	-	-	Bal.
3	1044	1.00	-	259	-	Bal.
4	5200	1.01	-	-	-	Bal.
5	5397	0.99	188	-	-	Bal.
6	5229	1.01	-	246	-	Bal.
7	5157	1.00	-	-	260	Bal.

The nominal composition of the deposition gas was 1000-5000 ppm C_2H_4, 1% CO, the balance of CO_2 with or without (nominally) 200 ppb of the sulphur compound. The pre-mixed deposition gas bottles were supplied by BOC. The actual composition (certified values) of each gas bottle is shown in Table 4.2. The oxygen partial pressure of these gases is controlled by the CO_2/CO equilibrium of the following reaction:

$$2CO + O_2 \longrightarrow 2CO_2 \tag{17}$$

and the partial pressure of oxygen can be estimated by the following relation:

$$P_{O_2} = \frac{P_{CO_2}^2}{P_{CO}^2} \exp\left(\frac{\Delta G^o{}_{17}}{RT}\right) \tag{18}$$

where P_{O_2}, P_{CO_2} and P_{CO} are the partial pressure of O_2, CO_2 and CO respectively, $\Delta G^o{}_{17}$ is the standard free energy change for the above reaction (17), R is the gas constant and T is the temperature in K. Using the standard free energy formation of CO and CO_2 obtained from ref. [201], the value for $\Delta G^o{}_{17}$ = -408.614 kJ/ mol can be calculated. For 1% CO/CO_2 the estimated partial pressure of oxygen was 3.5×10^{-21} at 600 °C. At this value, Fe and Cr are expected to oxidise, but not nickel [12].

The carbon activity, a_c, for the depositing gases arises from the dissociation reaction of ethylene (C_2H_4) with CO and CO_2 and the various possible reactions have been identified [12]:

$$C_2H_4 + 2CO_2 \longrightarrow 2C + 2CO + 2H_2O \quad (19)$$

$$C_2H_4 + 2CO \longrightarrow 4C + 2H_2O \quad (20)$$

$$C_2H_4 + CO_2 \longrightarrow 3C + 2H_2O \quad (21)$$

The standard free energy changes [12] for these reactions are shown in Table 4.3. These values were used to estimate the equilibrium constant, K_i,

$$K_i = \exp\left(\frac{\Delta G_i^o}{RT}\right) \quad (22)$$

and from which the carbon activities for each of these reactions was calculated (Table 4.3) at 600 °C for both 1000 ppm and 5000 ppm C_2H_4 bearing gases. The estimated carbon activities for the 1000 and 5000 ppm bearing depositing gas mixture are in the range of $10^1 < a_c < 10^6$ and $10^1 < a_c < 10^7$ respectively.

Table 4.3: Estimates of free energy changes *[12]*, equilibrium constant and carbon activities at 600 °C.

Reaction	ΔG_i^o (J/mol) [12]	Equilibrium constant, K_i	a_c from 1000 ppm C_2H_4	a_c from 5000 ppm C_2H_4
(19)	-87246	1.7×10^5	6.4×10^6	1.4×10^7
(20)	-40404	2.6×10^2	5.1	7.6
(21)	-113825	6.5×10^6	5.4×10^3	9.3×10^3

While the actual value of a_c depends on which reaction is favourable and how close to the equilibrium is reached, nonetheless, a high carbon depositing environment (i.e. $a_c > 1$) is expected for the current work.

4.8. Rig Modification

When the H_2S (certified value of 246 ppb) bearing deposition gas bottle was passed through the furnaces (both at operating temperature) the measured TS was only 114 ppb. It was realised that more than 100 ppb of sulphur content was lost within the rig system.

Both furnaces in the rig system contain alumina tubes. It was suspected that these alumina tubes might have trapped sulphur species. These alumina tubes were replaced with quartz furnace tubes, Fig. 4.6. Quartz was chosen because it was used in the M501TS thermal oxidiser which gave the extra confidence in using a quartz tube. The TS reading for the same H_2S bearing gas bottle passed through the modified rig was 207 ppb. Although the reading was lower than that certified, however, it is an improved result than the previous reading with an alumina tube. This new modified rig system was used for the work done in Chapter 6 which involved using deposition gases with and without COS, H_2S and CH_3SH.

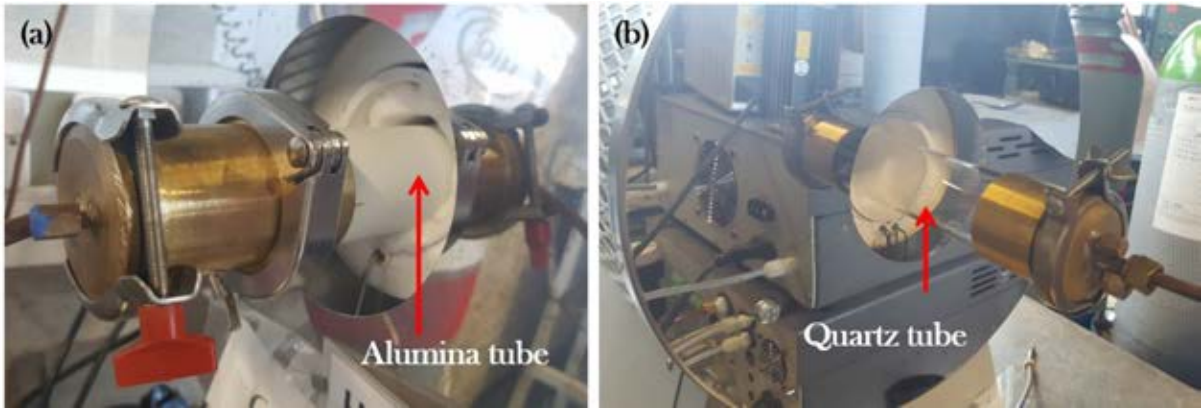

Fig. 4.6: (a) Alumina furnace tube. (b) Quartz furnace tube.

For the work presented in Chapter 5, the deposition experiments were done with alumina furnace tubes. This work is still valid as the amount of sulphur lost within the rig (with alumina tubes) for COS bearing gas (certified value 215 ppb) was only about 10 ppb.

4.9. Characteristic Techniques

The samples were examined using various electron microscopy techniques: SEM, SEM-EDS, TEM, TEM-DP, STEM, STEM-EDS.

4.9.1 Scanning Electron Microscope (SEM)

The SEM used for the current work was TESCAN-MIRA3. It is a high-performance Schottky field emission SEM with very high resolution and low-noise, and with accelerating voltage in the range of 200 V – 30 kV. It is equipped with various detectors including Secondary Electron (SE), Back-scattered Electron (BSE), and Energy Dispersive X-ray (EDS) detector. The EDS detector is an 80 mm^2 X-Max^N silicon drift detector (SDD) supplied by the Oxford Instruments plc. EDS (point analysis, line profile and elemental mapping) were carried out using Aztec software that has a unique built-in function (called Tru-Q, Truline and TruMap) that automatically removes X-ray background or any artefact and correct any overlapped peaks for false element identification.

Following the carbon deposition experiment, the samples were transferred to the SEM. No further sample preparation was needed. The bulk rectangular samples were mounted on aluminium stub with carbon conductive adhesive. The 3 mm TEM discs were placed directly on the stage without using adhesive. This is done to protect the TEM discs that were later used in S/TEM. SEM was operated at 10 kV for imaging and the EDS data were acquired either at 10 or 5 kV.

4.9.2. Transmission Electron Microscope (TEM)

3 mm TEM discs and TEM foils prepared by the focused-ion beam (FIB) were analysed under various S/TEM. Nano-beam electron diffraction (NBED) analysis and TEM-bright field (BF) imaging were carried out on a JEOL-2100 TEM. STEM imaging and nano-probe EDS analysis were acquired using an FEI Tecnai F20 and a TALOS F200X S/TEM. Tecnai

F20 was fitted with X-Max^N 80 TLE silicon drift x-ray detector (SDD) which is operated using Aztec software, both supplied by Oxford Instruments plc. TALOS F200X is equipped with four SDD (30 mm^2) detectors which are located symmetrically around the sample stage. This allows the operator to acquire EDS without needing to tilt the stage at a specific angle to collect the maximum signal. All S/TEM was operated at 200 kV.

4.9.3. Sample Preparation for TEM Using Focused Ion Beam (FIB)

Along with 3 mm TEM foils, several site-specific thin TEM foils were also prepared using a focused ion beam – scanning electron microscope (FIB-SEM) technique. FIB-SEM is a dual beam system that uses electron beam for imaging and high energy ion beam (usually Ga^+) for fast material removal from the sample surface via ion-sputtering. The ‘’milling’’ of the sample can be controlled down to nanometre scales with relatively low damage to the sample and preserve the microstructure of the sample.

FIB-TEM foils were prepared from the bulk rectangular samples using an FEI Quanta 3D FEG FIB-SEM. This method allows the examination of the cross-section of the oxide layer. The stages required to prepare TEM foils using FIB are shown in Fig. 4.7. First, a 3 µm thick layer of platinum was coated onto the surface of the area of interest. This provided protection to the surface (and the oxide layer) during milling and gave some rigidity to the final TEM foil. Using a high current Ga^+ ion beam at 30 kV, ‘in-situ’ bulk milling was done on either side of the coated area to produce a foil that was approximately 1 - 2 µm thick. The foil was then extracted from the bulk sample and transferred to the standard TEM copper grid using a micro-manipulator (omniprobe). Finally, the foil was thinned further and cleaned using a lower ion beam current until it was less than 200 nm thick.

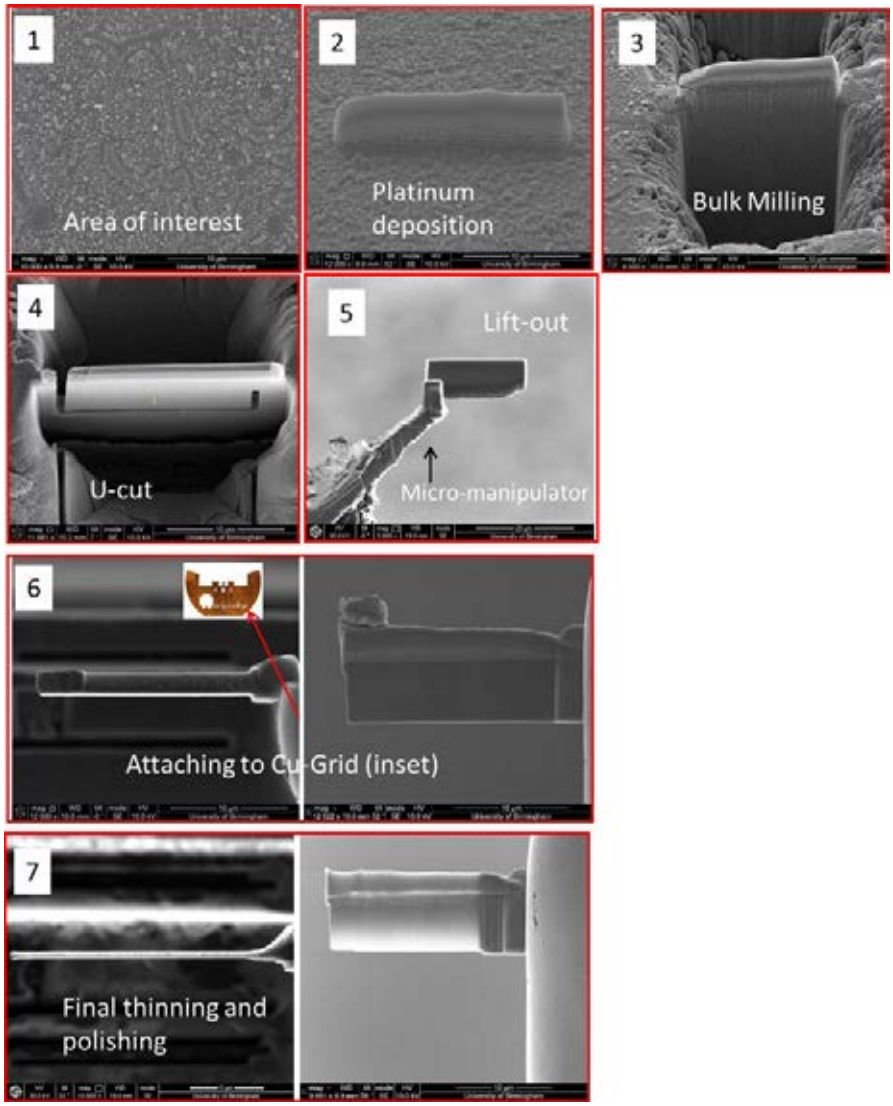

Fig. 4.7: SEM images showing various stages of the TEM foil preparation by FIB: (1) Selecting area of interest. (2) Platinum deposit. (3) Bulk milled. (4) Undercut. (5) Lift out. (6) Attached to the copper grid (inset). (7) Final thinned and polished. Stage 6 and 7 are shown in top and side view.

5. Formation of Nickel-Rich Particles and the Inhibition Role of COS on Carbon Deposition

5.1. Sulphur-Free Carbon Deposition

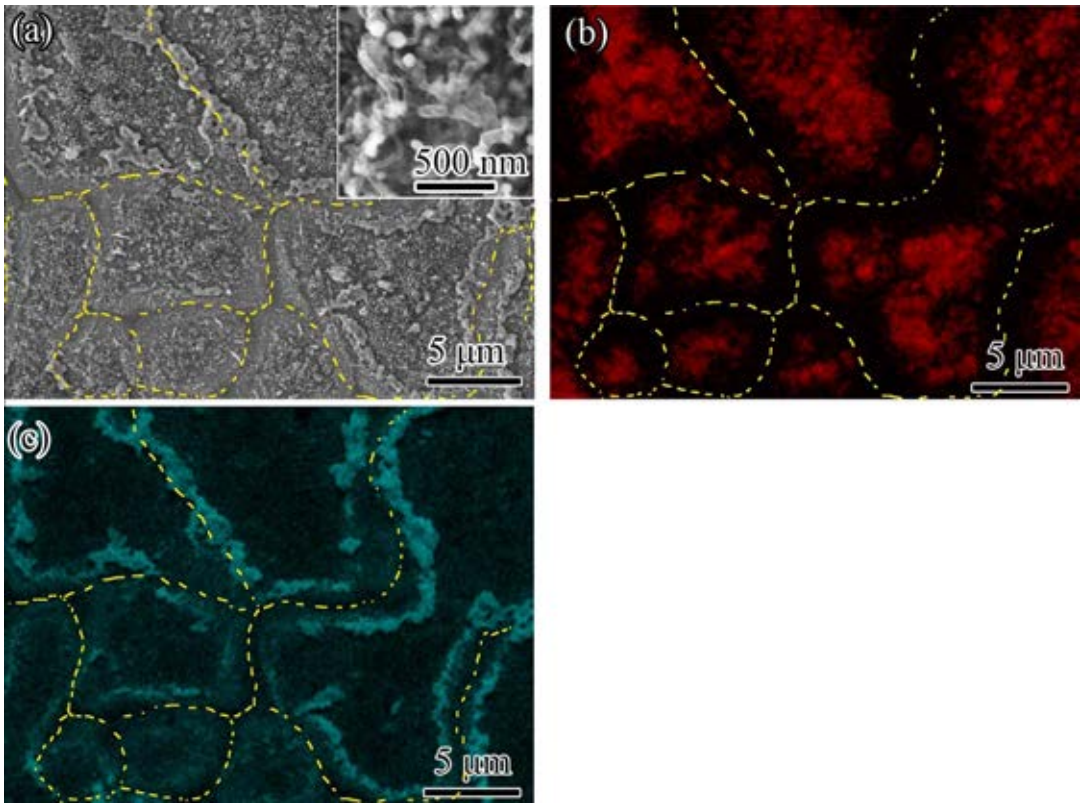

Fig. 5.1: (a) SEM image showing the surface of the sample following the 4 hours exposure at 600 °C to the sulphur-free deposition gas mixture. The inset shows a high magnification SEM image of individual carbon filaments. The corresponding EDS elemental map of carbon and iron are shown in Fig. 2(b) and Fig. 2(c) respectively. Yellow dashed lines outline the grain boundary.

Fig. 5.1a shows the typical surface structure of the sample following the test in the sulphur-free gas mixture. The surface was covered with carbon deposits which were filamentary in nature as seen in the inset. The distribution of carbon and iron on the surface of the sample is shown by the EDS elemental maps in Fig. 5.1b and 5.1c. It clearly demonstrates that the deposition was concentrated at the grain centres. In Fig. 5.1, the grain boundaries were outlined by the yellow dashed lines. This lower carbon deposition at grain boundaries was probably provided by the protective chromia layer [12, 20], which preferentially forms at grain boundaries [172] during the early stage of oxidation, due to the fast diffusion of

chromium via these paths to the surface of the alloy. Adjacent to the grain boundaries, long and continuous particles of a few micrometres in size were observed. EDS analysis showed that these particles were iron-rich (Fig. 5.1c). Although the formation of metallic Fe particles under 1% CO/CO_2 is thermodynamically unfavourable [12], it is possible that the iron-rich particles were formed via a reduction reaction occurring during the cooling stage under the 5% hydrogen in argon.

At high magnification, it was observed that the carbon filaments consisted of a bright particle at their tips (Fig. 5.1a, inset). The nature of the particle was studied using TEM. Fig. 5.2a and 5.2b show carbon filaments projecting from the edge of a 3 mm diameter TEM disc exposed in the sulphur-free deposition gas mixture for 4 hours at 600 °C. The high angle annular dark field (HAADF) image and the EDS maps obtained (Fig. 5.2(b-e)) showed that the particles were composed of nickel and iron and connected to the sample edge by thin carbon filaments.

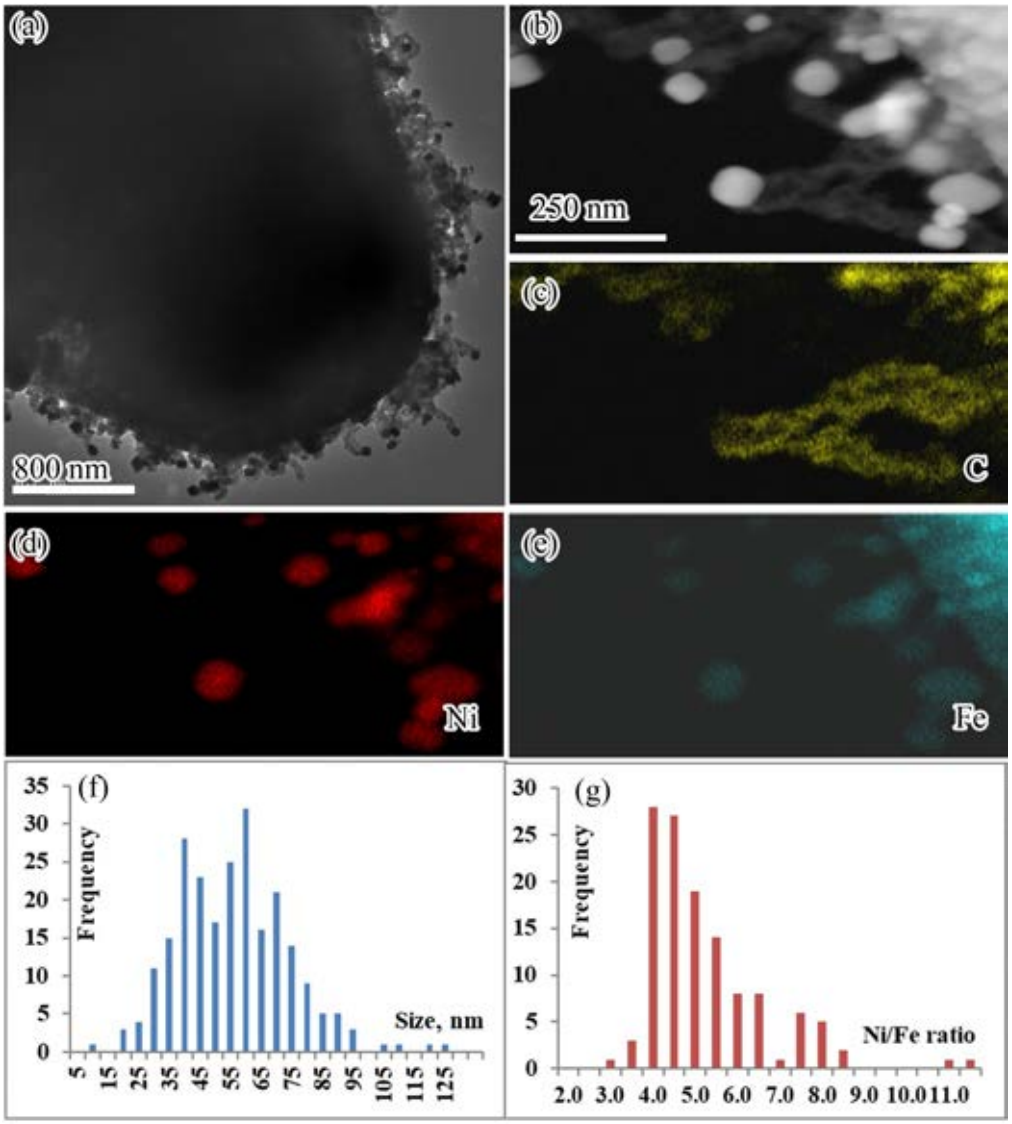

Fig. 5.2: TEM bright field (a) and STEM-HAADF (b) images showing bright small particles are attached to the carbon filaments at the edge of the sample tested in the sulphur-free gas for 4 hours at 600 °C. The particles can be seen at the tip of each filament. Elemental maps of carbon (c), nickel (d) and iron (e) from the same region as in (b). (f) The size distribution and (g) nickel-iron ratio of the particles located at the tip of the filaments.

The size and composition of these particles were measured. As shown in Fig. 5.2f the particle sizes ranged from 5 to 120 nm with an average of 58 nm. EDS spectra were collected only from those particles located at the tip of filaments projecting from the edge of the sample, in order to minimise the effect of the bulk alloy. The chemical composition determination was based on the assumption that the particles of 50 nm thick were involved without the accurate measurement of sample thicknesses in each measurement. It has been noticed that while the

thickness of the particle varied from 10 nm to 150 nm in the calculation, the nickel concentration measured varies within 0.1 at%. Therefore assuming the thickness of 50 nm is not expected to have a significant impact on the results obtained. Each spectrum was recorded for a 20 seconds dwell time which typically collected over 200,000 counts of X-ray photons. Fig. 5.2g shows that the nickel-iron ratios measured from most particles are larger than 4 (in the range of 2.9 to 11.2, with an average of 5). This result agrees well with the work of Park and Baker [202] who investigated the decomposition of ethylene over nickel-iron bimetallic particle to produce methane, ethane and solid carbon (identified as filamentous in nature). They observed that the conversion of ethylene over nickel-iron particles with a nickel content of 70% or less is extremely low. However, there was a dramatic increase in the conversion of ethylene into solid carbon when nickel concentration was greater than 75%.

Fig. 5.3 shows a series of electron diffraction patterns obtained from the Ni-rich particle in three zone axes. The diffraction patterns are consistent with the austenitic face-centred cubic (FCC) structure with the lattice parameter of about 3.6 Å. The detailed structure of the filament along with the particle can be seen in the high-resolution image shown in Fig. 5.4. It is a solid carbon with turbostratic structure, encapsulating the particle. The lattice fringes of the particle are clearly visible. The measured fringe spacing was approximately 0.2 nm, close to {111} inter-planar spacing of FCC nickel. These observations are consistent with a previous study [12].

According to the Ni-Fe phase diagram (Fig. 5.5), the Fe-Ni alloy with a nickel content of 75 to 90 at% will have a disordered γ- FCC (austenite) structure at 600 °C and at temperatures below circa 500 °C, the disordered γ- FCC phase will begin to transform into $L1_2$ structured $FeNi_3$ (Prototype: Cu_3Au [203]). Since superlattice reflections were absent on the diffraction patterns taken from the particle (Fig. 5.3), this suggests that the Ni-rich particles do not

assume the ordered structure. This is not unexpected as the phase transformation in Ni-Fe alloys is very slow below the critical temperature (~ 500 °C) [204]. Furthermore, at temperatures below 400 °C, the diffusion process is extremely slow such that the phase transformation is too sluggish to form ordered $FeNi_3$ in any appreciable degree at the laboratory time scale. Liu et al, [205] have studied the kinetic of order-disorder phase transformation of $FeNi_3$ in the Fe-Ni system. They showed that only circa 5 vol. % of disordered γ- FCC is converted into ordered $FeNi_3$ after approximately 10 hours of annealing Fe-Ni alloy samples with a composition of 25 at% Fe and 75 at% Ni at 475 °C. This is shown in Fig. 5.6. Clearly, for the current work where the alloy was furnace cooled in Ar from 600 °C to less than 50 °C in about 10 hours, it is unlikely that any observable $FeNi_3$ phase will have formed, as the amount of time spent in the 500-450°C temperature window where the kinetics would realistically allow this phase transformation to occur was relatively short. This is consistent with earlier observations that the Ni-rich particles have a disordered γ- FCC (austenite) structure.

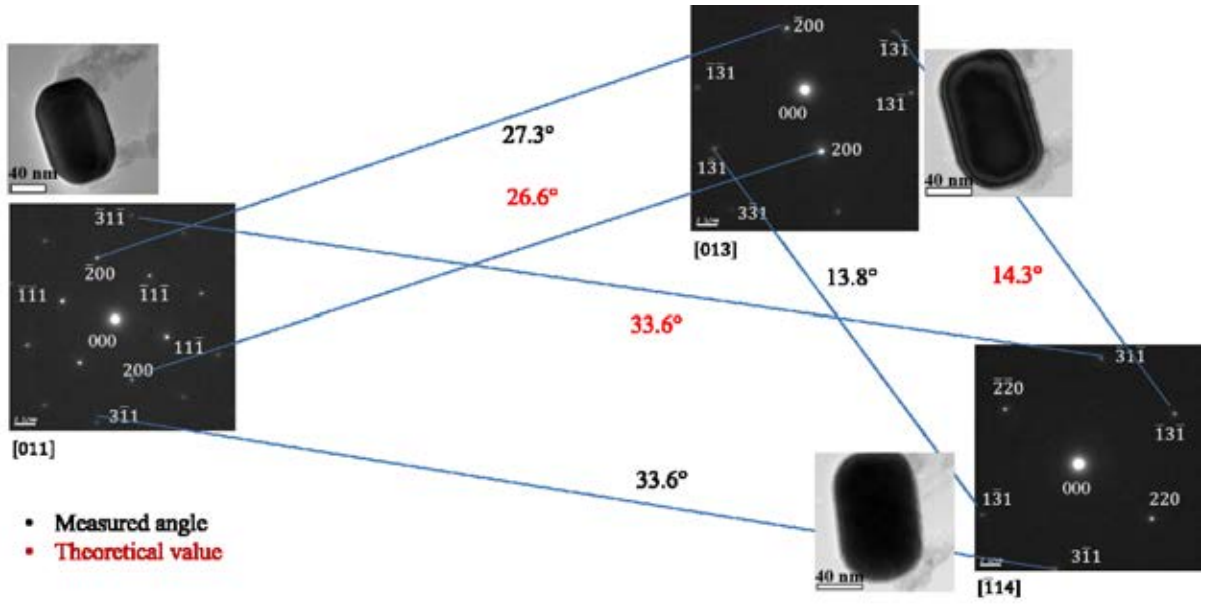

Fig. 5.3: Electron diffraction pattern obtained from the Ni-rich nanoparticle (sulphur-free) in three different zone axes. The measured tilting angle between these zone axes agrees with the

expected value confirming the particle has a face-centred cubic structure. Also, shown here are the image of the same particle in each zone axis.

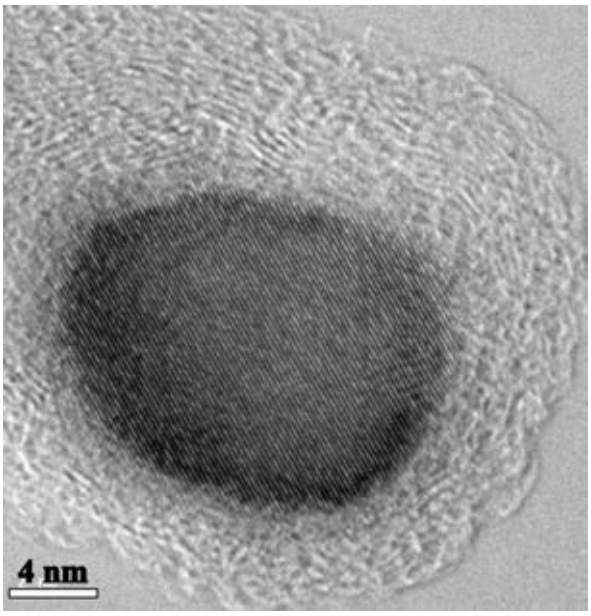

Fig. 5.4: A high-resolution image (c) showing the turbostratic carbon surrounding a nickel-rich particle with lattice spacing close to the {111} inter-planar spacing of nickel.

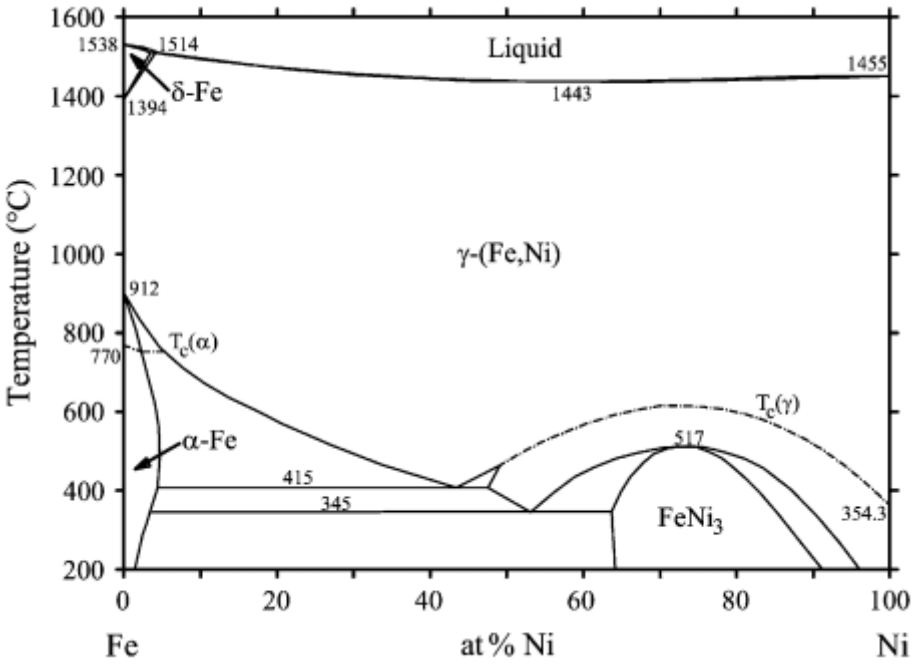

Fig. 5.5: The assessed Ni-Fe phase diagram based on the experimental investigation of meteoritic samples that were cooled slowly over millions of years [206].

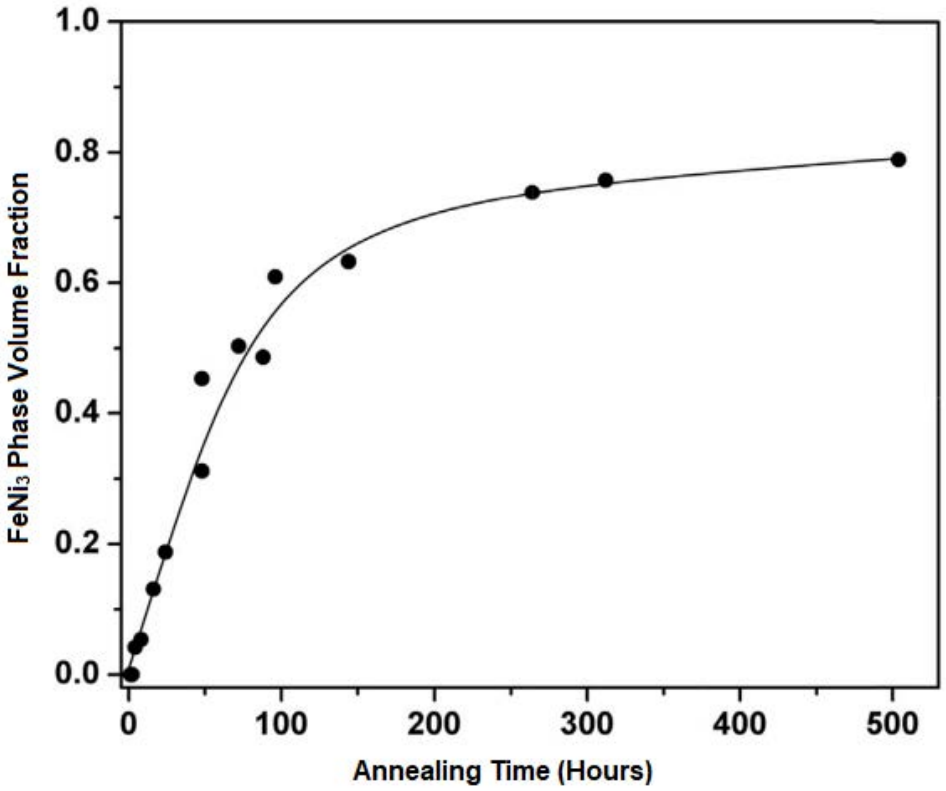

Fig. 5.6: Volume fraction of ordered $FeNi_3$ in Fe-Ni alloy with a composition of 25 at% Fe and 75 at% Ni following annealing at 475 °C for times between 0 to 500 hours. Prior to annealing, all alloys had a fully disordered austenitic FCC structure [205].

5.2. Effect of Carbonyl Sulphide on Carbon Deposition

After the exposure in the gas mixture containing 215 ppb COS, no carbon filaments were observed on the sample using an SEM. Fig. 5.7a is an SEM micrograph showing the surface

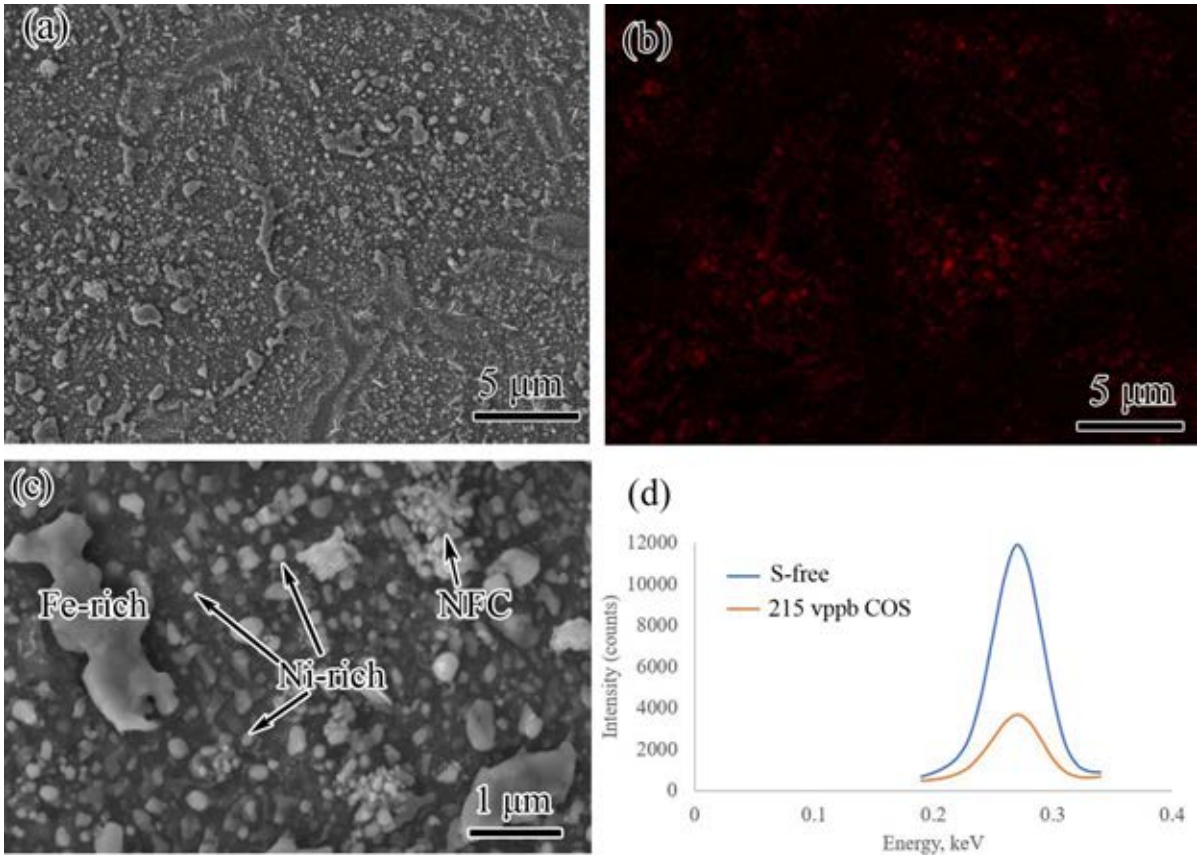

Fig. 5.7: (a) SEM image showing the surface of the sample following the 4 hours exposure to the deposition gas with 215 ppb COS at 600 °C. (b) Elemental carbon map corresponding to (a). (c) Higher magnification SEM image showing the surface covered with scattered nickel- and iron-rich white particles and carbon deposit that glued some nickel-iron rich particles into agglomeration (identified as NFC). (d) EDS carbon X-ray spectra collected from a surface area of 44 µm by 58 µm on both samples under identical electron microscope settings. The total carbon X-ray counts collected from the sulphur-free and COS-containing samples are 71k and 26k, respectively. Clearly, the addition of 215 ppb COS into the gas mixture has resulted in the significant suppression of carbon deposition.

of the sample after the test. The EDS map of carbon (Fig. 5.7b) shows only a very small amount of carbon present on the surface. The grain centres were decorated with light contrast particles which were found to be nickel- and iron-rich (Fig. 5.7c). Some of these particles were held together into clusters by non-filamentary carbon (marked as NFC in the image), consistent with the elemental carbon map. Larger micrometre-sized iron-rich particles, as described earlier, were also present. Fig. 5.7d shows the carbon X-ray peaks collected from the sample exposed in the sulphur-free gas mixture and that in the mixture containing 215 ppb COS, under otherwise identical conditions. As an estimate based on the area under the

peak, the amount of carbon on the sample treated in the COS-containing gas mixture is less than half of that treated in the sulphur-free gas mixture. In other words, 215 ppb COS has significantly reduced the carbon deposition.

5.3. STEM Analysis

5.3.1 Sample Treated in the Sulphur-Free Gas Mixture

To understand the formation mechanism of nickel-rich particles, FIB was used to extract thin foils from the samples treated in the sulphur-free gas mixture. Fig. 5.8a is a HAADF image showing the typical cross-sectional view of the sample. The region within the rectangular box 'b' was further studied and the chemical composition mapped in Fig. 5.8(b-f). As shown in Fig. 5.8b, the oxide formed above the grain boundary (g.b.) was obviously thinner (of ~100 nm) than that formed over the grain interior (of ~400 nm in Fig. 5.8g). The EDS maps (Fig. 5.8d and 8e) clearly demonstrate that the oxide is a chromium oxide. Above this oxide layer, particles of irregular shape can be observed. The iron and oxygen maps showed that iron oxides were encapsulated by elemental iron forming a core-shell type configuration (see Fig. 5.8c and 8e).

Region ''g' in Fig. 5.8a was studied and chemically mapped in Fig. 5.8(g-k). Features of bright contrast can be observed in the oxide (Fig. 5.8g) and are shown to be nickel-rich (Fig. 5.8k) with some iron (Fig. 5.8h). The gaps in the oxygen (and chromium) map corresponding to these nickel-rich features suggesting that these are not oxides. The composition of these nickel-rich features is characteristic of the particle located at the tip of the filament.

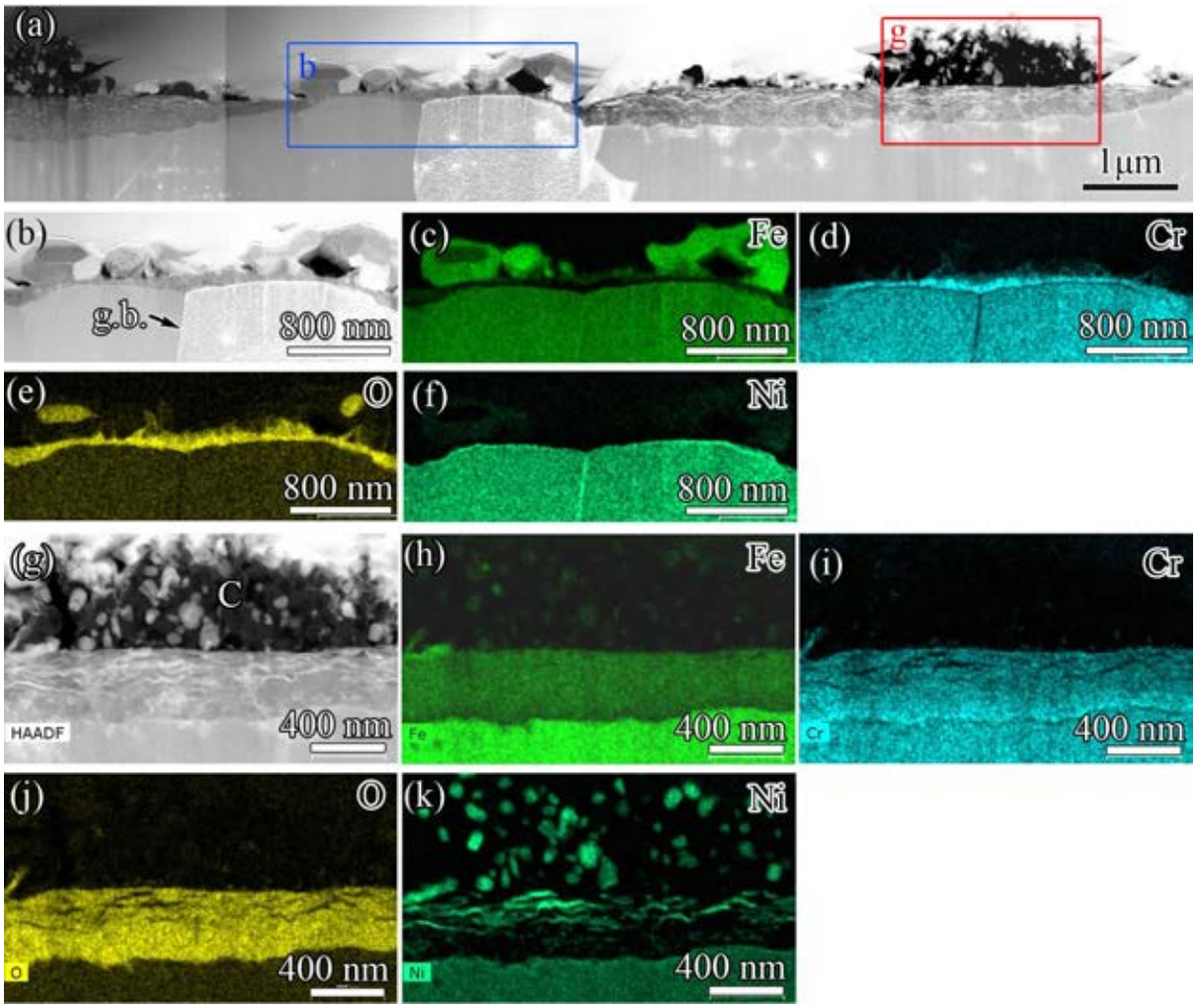

Fig. 5.8: (a) STEM image of a cross-section through the surface of a sample exposed to a sulphur-free deposition gas mixture. Region b (within the blue rectangle) and Region g (within the red rectangle) were mapped and presented in Fig. (b-f) and Fig. (g-k), respectively. (b) A higher magnification STEM image of the region in the blue box region b. The elemental maps of (c) iron, (d) chromium (e) oxygen and (f) nickel corresponding to (b). (g) STEM image of a cross-section across the grain boundary, shown in the red box in (a). The elemental maps of (h) iron, (i) chromium (j) oxygen and (k) nickel corresponding to (g). EDS maps show the presence of nickel-rich features within the (iron, chromium) oxide layer.

5.3.2. Sample Treated in the Gas Mixture Containing 215 ppb COS

Fig. 5.9a is a STEM HAADF image showing the cross-section of the grain centre in a sample treated in the COS-containing gas mixture for 4 hours at 600 °C. The elemental maps (Fig. 5.9c, 9d and 9f) show that an iron-chromium-rich oxide layer of about 100~200 nm thick has formed. Nickel-rich particles were observed (Fig. 5.9e). The nickel-rich particles within the oxide layer are elongated parallel to the metal/oxide interface of typically 20~30 nm thick

and can be of ~200 nm long and those above the oxide layer are of irregular shapes of about 50 nm in size.

The chemical information of the nickel-rich particles within the oxide layer was analysed. Fig. 5.10a shows a STEM HAADF image obtained from the sample treated in the COS-containing gas mixture for 4 hours at 600 °C. EDS point analysis of the particle and the surrounding oxide was performed and the results are shown in Fig. 5.10b and 10c. A small but noticeable sulphur peak exists on the spectrum obtained from the nickel-rich particle (Fig. 5.10b), not on that obtained from the surrounding oxide (Fig. 5.10c).

The EDS elemental maps in Fig. 5.10e and 10f clearly demonstrated that both nickel and sulphur are concentrated on the particle rather than in the oxide. An EDS linescan across the particle is shown in Fig. 5.10g and 10h for nickel and sulphur respectively. The nickel X-ray signal peaks at the centre of the particle, presumably due to the larger thickness of the particle there. It should be noted that the sulphur X-ray signal shows two peaks coincident with the edge of the particle, suggesting that sulphur is not homogeneously distributed within the particle but probably concentrated on the surface of the nickel-rich particle.

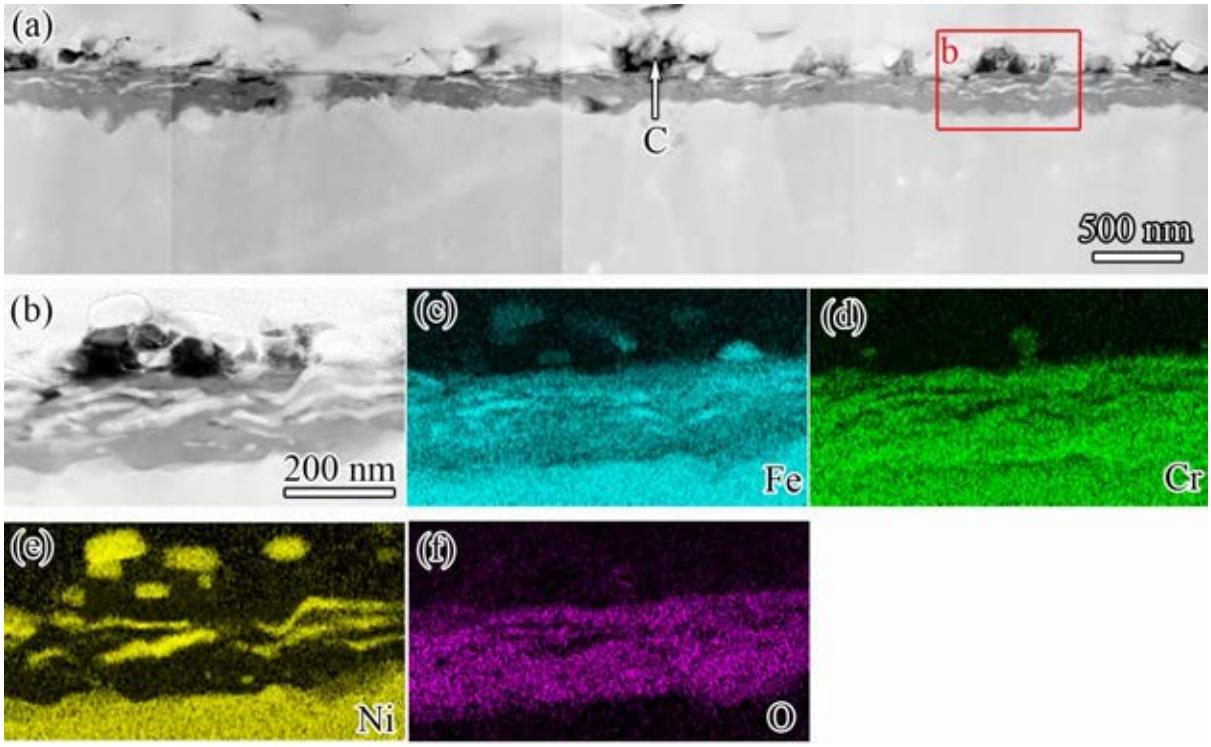

Fig. 5.9: (a) STEM HAADF image showing the cross-section of a sample exposed to the COS-containing gas mixture. (b) A higher magnification STEM image of region 'b' shown in the red box in (a) and the corresponding EDS elemental maps of iron (c), chromium (d), nickel (e) and oxygen (f).

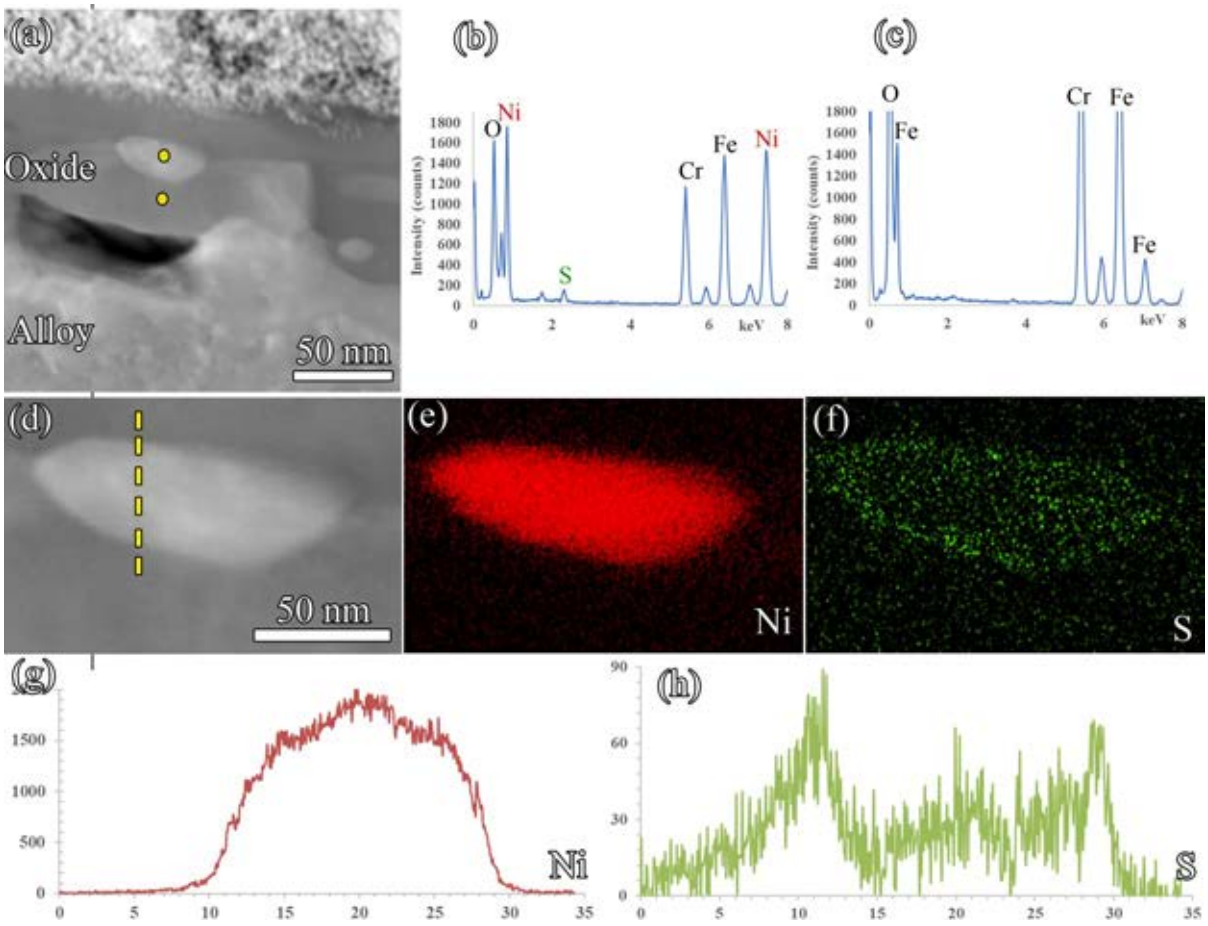

Fig. 5.10: Qualitative EDS analysis of a nickel-rich particle within the oxide layer in the sample that was exposed to the COS-containing gas. (a) STEM image of the particle within the oxide layer. Point EDS confirmed the presence of (b) sulphur in the particle, but not in the oxide (c) where the signal is at the background level. (d) Magnified image of the particle seen in (a). Elemental maps showing the distribution of (e) Ni and (f) S across the particle. (g) Ni and S line-profile across the particle shows that the sulphur is concentrated around the edge of the particle. This implies that sulphur is present on the surface of the nickel-rich particle.

5.4. Diffraction Analysis

Fig. 5.11a shows a TEM bright field image of a nickel-rich particle of about 50 nm in diameter within the oxide layer of the sample exposed to the COS-containing gas mixture for 4 hours at 600 °C. The electron diffraction patterns obtained from the steel matrix and the particle are shown in Fig. 5.11b, 11c and 11d. Identical diffraction patterns were acquired from both the steel matrix and the particle. After series tilting experiments, the nickel-rich particle was found to assume the FCC structure and also to have the same crystal orientation as the steel matrix. The diffraction patterns (Fig. 5.12) obtained from a nickel-rich particle

and the steel matrix in the sample exposed in the sulphur-free gas mixture for 4 hours also show the same relationship. Fig. 5.13a is a TEM image showing the oxide layer in the sample exposed to the COS-containing gas mixture. The diffraction pattern (Fig. 5.13b) obtained from the grain encircled in pink dashed curves confirmed that the oxide is the FCC structured $FeCr_2O_4$ spinel (chromite).

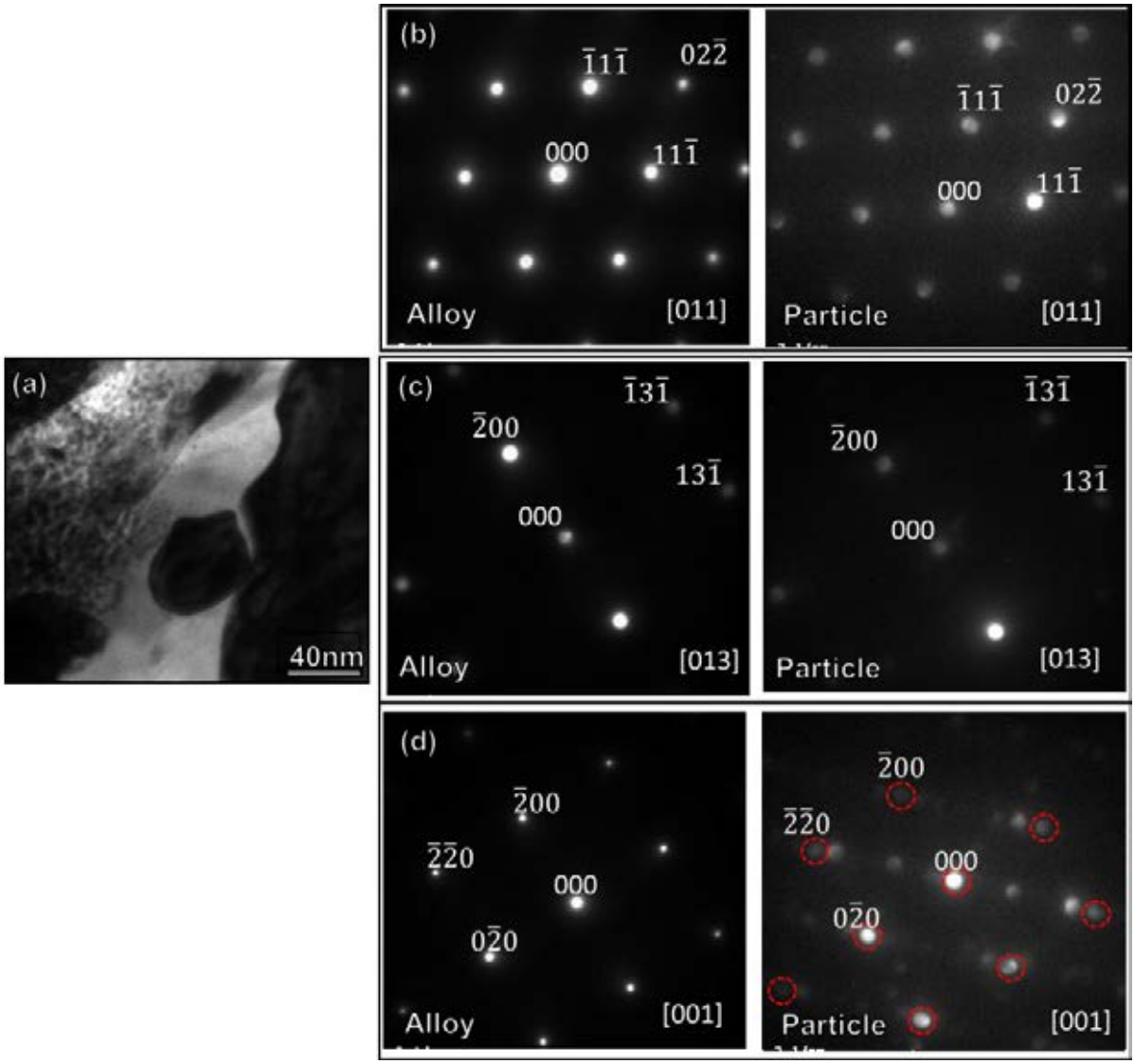

Fig. 5.11: (a) TEM-BF image of a nickel-rich particle and the electron diffraction patterns (b, c and d) at three different zone axes obtained from the alloy (left) and the Ni-rich particle (right) for the sample exposed to COS containing gas. It shows that the particle has the same crystal orientation and FCC structure as the alloy. Zone axes: (b) [011], (c) [013] and (d) [001].

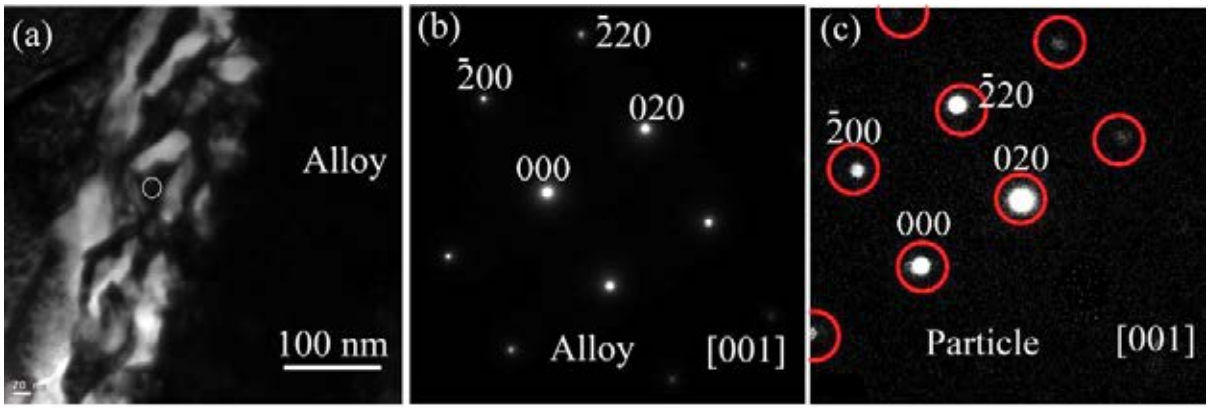

Fig. 5.12: (a) TEM-BF image of a nickel-rich particle and the electron diffraction patterns obtained from (b) the alloy and (c) the nickel-rich feature for the sample exposed to the sulphur-free gas mixture. It shows that the nickel-rich feature has the same crystal orientation and FCC structure as the alloy. The particle was positioned by the white circle in (a).

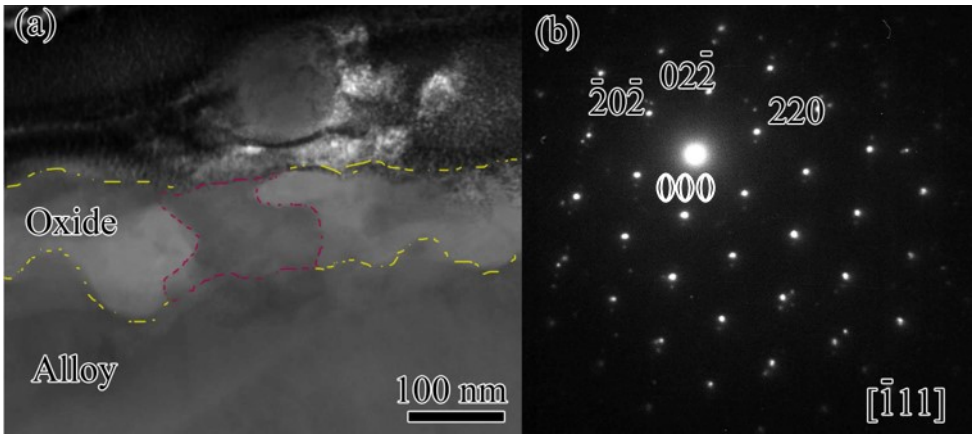

Fig. 5.13: (a) A cross-sectional STEM-BF image obtained from a sample exposed to the COS-containing gas mixture. The diffraction pattern (b) taken from the oxide grain in dark contrast (highlighted in pink) is consistent with that of the FCC structured chromite.

5.5. Oxide-Metal Interface

It is well documented [207, 208, 209, 210, 55] that the oxidation of chromium results in the depletion of chromium in the immediate vicinity of the metal/oxide interface. As shown in Fig. 5.14, the chromium depletion is coincident with the nickel enrichment at the metal-oxide interface.

At a further distance from the steel matrix, the oxide is composed of alternating layers containing varying amounts of nickel and chromium. Peaks in nickel showed a corresponding decrease in oxygen. Iron was also present within the oxide but at a more uniform distribution.

Similar nickel enrichment at the oxide-metal interface was also observed in the sample treated in the COS-containing gas mixture, as shown in Fig. 5.15. Fig. 5.15 also shows that a small amount of sulphur was present at the oxide-metal interface. It should be noted that this interfacial sulphur enrichment was only observed at the interface where nickel-enrichment occurred, but not in the oxide nor the steel matrix. No sulphur was observed in the COS-free sample, as expected.

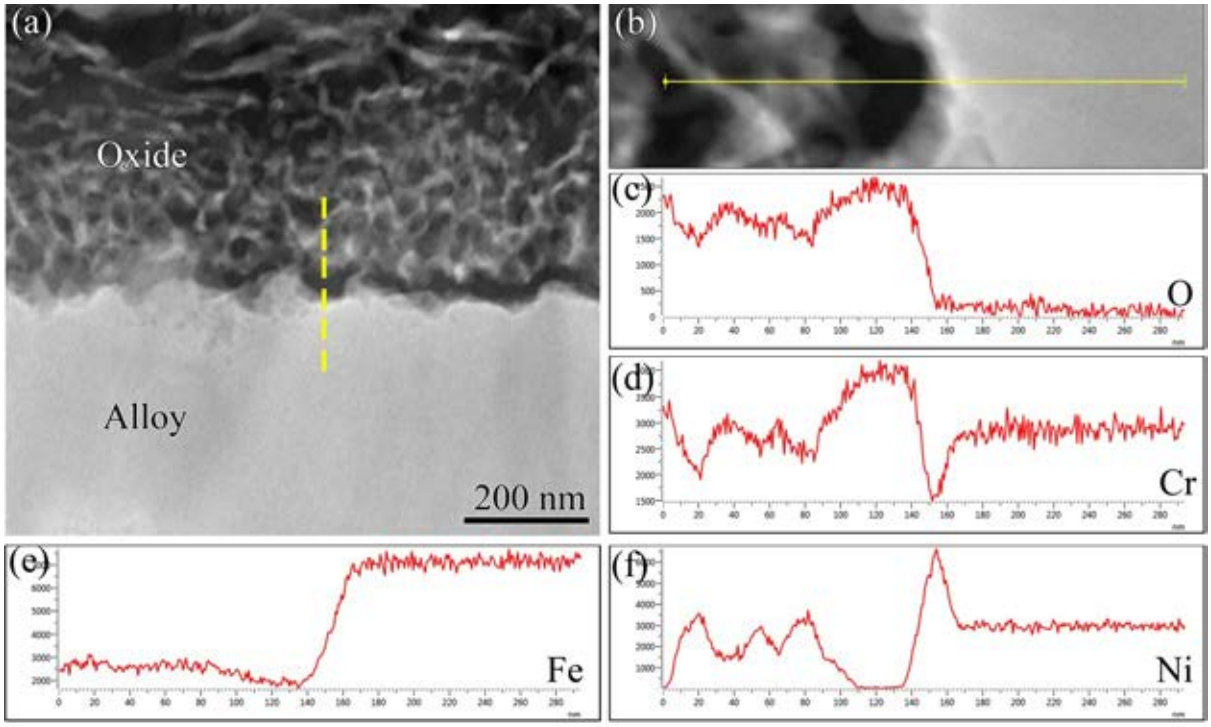

Fig. 5.14: (a) and (b) A cross-sectional STEM image of the sample exposed to sulphur-free gas mixtures. The concentration profiles of (c) O, (d) Cr, (e) Fe and (f) Ni across the oxide-metal interface.

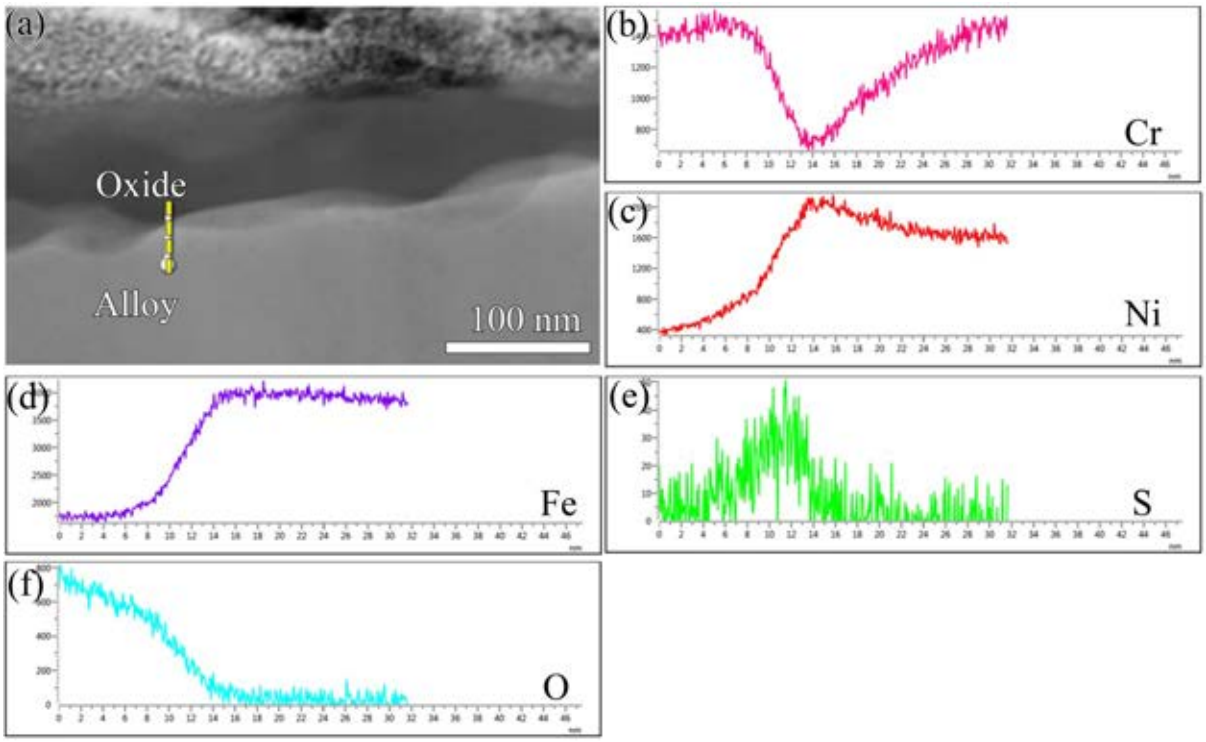

Fig. 5.15: (a) STEM image showing the cross-section of the sample exposed to COS-containing gas mixture. The concentration profiles obtained from the linescan across the oxide-metal interface following the yellow line in (a) are shown in (b) Cr, (c) Ni, (d) Fe (e) S and (f) O.

5.6. Discussion

5.6.1. Nickel-Rich Particle Formation Mechanism

Millward *et al*. [12, 14] observed nickel particles associated with carbon filaments during the oxidation of this steel and based on the fact that the only source of nickel is the steel itself, they suggested that the catalytic nickel nano-particles originated from the alloy during the oxidation process. Under the gas conditions used [12], the oxygen partial pressure was controlled by the CO_2/CO ratio such that nickel was the only alloying element that was thermodynamically stable as a metal with the other alloying elements form oxides.

The results obtained from the current study have confirmed that nickel enriched at the metal-oxide interface where chromium and iron were preferentially oxidised to form chromite. As shown schematically in Fig. 5.16a, as oxidation proceeds, the nickel-enriched regions break

up into individual particles and are left in the oxide as the internal oxidation front (oxide-metal interface) moves inward (Fig. 5.16b and 16c). This is consistent with the observation that nickel-rich particles in the oxide sometimes are elongated and parallel to the metal/oxide interface (see for example Fig. 5.8k and 5.9e). During this process, it would be expected that the nickel-rich particles formed to maintain the crystallography orientation as that of the metal matrix due to the fact that both are of FCC structure with similar lattice parameters. This was indeed confirmed by the electron diffraction patterns taken from samples treated in both the COS-free and the COS-containing gases (Fig. 5.11 and 5.12). In the current work, it seems that the orientation of these nickel-rich particles had not been altered during further oxidation. However, it was noticed that wherever the carbon filaments have been observed, the nickel-rich particles attached have very different orientations with the steel matrix likely due to the attached carbon filaments.

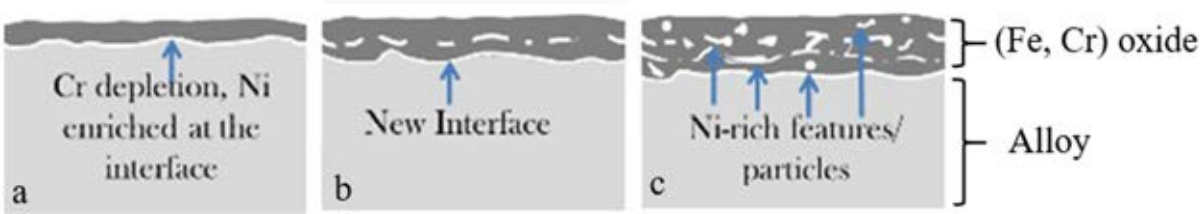

Fig. 5.16. Schematic diagrams of the mechanism leading to the formation of the nickel-rich particles within the oxide at the grain centres.

It has been found that, close to grain boundaries, the chromium oxide layer is thin (~100 nm in Fig. 5.8 for example). This is probably due to the fast diffusion along grain boundaries, chromium oxide (chromia) formed at the early stage of the oxidation was dense and slowed down the further oxidation, thus, preventing the formation of nickel enriched region. While away from the grain boundaries, the oxide layer was much thicker and it is $FeCr_2O_4$ (chromite).

In the current study, the thickness of the oxide (chromite) formed in the COS-free gas mixture was approximately 300 ~ 500 nm while that formed in the COS-containing gas mixture of about 100 ~ 200 nm. In other words, the oxidation kinetics in the COS-containing gas is slower. This is discussed in the next chapter 6.3.4.

5.6.2. Inhibition Mechanism (the Distribution of Sulphur in the Alloy)

In the present work, the filamentary carbon deposition on the sample treated in the sulphur-free deposition gas mixture was shown to be catalysed by nickel-rich particles, formed within the subsurface oxide layer. Adding 215 ppb of COS to the gas mixture with high carbon activity effectively suppressed the carbon deposition. Although nickel-rich particles were also formed during the oxidation in the COS-containing gas mixture, it seems that these particles are no longer catalytic. It was postulated [15] that there are two possible ways by which catalysts can be deactivated, *viz*. by converting metallic nickel-rich particles to sulphide or by the surface poisoning of nickel-rich particles.

According to the literature [211, 212, 213], the thermodynamically most stable form of nickel sulphide is Ni_3S_2 which assumes a rhombohedral crystal structure [214]. In this study, the EDS and diffraction analysis suggests that the sulphur concentrated at the surface of the nickel-rich particles. The nickel-rich particles assume an FCC structure with the lattice parameter of about 0.36 nm, i.e., consistent with that of metallic nickel, but not Ni_3S_2. A thermodynamic calculation showed that about 680 ppb of COS is required to form Ni_3S_2 in equilibrium with 1 % CO at 600°C [195]. In other words, a much higher COS concentration than used in the present tests would be required for Ni_3S_2 to be stable thermodynamically.

Ni_3S_4 is the only nickel sulphide binary phase assuming the FCC structure [215] however with a lattice parameter of 0.9457 nm [216], much larger than the 0.36 nm determined from the nickel-rich particles formed in this study. The diffraction analysis clearly shows the

presence of metallic (austenitic) phase in Ni-rich particles. However, it should be noted that this technique is unable to determine the chemical nature of the very thin Ni-S layer of only a few atomic layers. Therefore, strictly speaking, it is impossible to exclude that sulphidation of nickel has not occurred in the current work and further work is needed to address this issue (see Future Work, section 7).

It seems more likely that catalyst de-activation arises from the formation of an adsorbed surface layer of sulphur. In the sample exposed in the COS-containing gas mixture, sulphur was observed on the surface of nickel-rich particles and also associated with the nickel-enriched region at the metal/oxide interface. Using a Langmuir-Hinshelwood approach, McGurk [195] calculated that at 600 °C, a COS content of 160 ppb in the gas mixture would be sufficient to cover 80% of the surface of nickel-rich particles with sulphur. The 215 ppb of COS used in the present work is thus sufficient to cover the vast majority of the surface of the nickel-rich particles. The observation of sulphur adsorption to the surface of nickel-rich particles is consistent with a number of previous studies [217, 218, 219, 220] In particular, Bartholomew and Katzer [218] [218] reviewed several studies on the poisoning of nickel catalysts by H_2S in CO hydrogenation and concluded that the formation of surface nickel-sulphur bonds was significantly more favourable than the formation of bulk nickel-sulphur bonds.

6. The Effect of COS, H_2S and CH_3SH on Carbon Deposition on 20Cr-25Ni Stainless Steel

6.1. Sulphur-Free Carbon Deposition

In this work, the relative effect of ethylene concentration on carbon deposition without the presence of sulphur species was studied. The result presented here will be used as a reference to measure the poisoning effect of COS, H_2S and CH_3SH.

Exposure of the samples to sulphur-free depositing gas for 4 hours resulted in extensive filamentary carbon deposition on the surface. Fig. 6.1a and 6.1c show the surface of samples treated in (nominal) 1000 ppm and 5000 ppm C_2H_4 respectively. For a lower concentration of C_2H_4, the carbon deposit was restricted within the centre of grains and no carbon filaments were present at the grain boundaries. In comparison, for higher concentration, the deposits at the centre of grains were thicker and some of the overgrown filaments were located at the grain boundaries. Fig. 6.1b and 1d show the deposit at the edge of the samples at higher magnification. Clearly, the filaments were significantly longer and the deposits were denser in the sample exposed to higher concentration of C_2H_4. This observation is also supported by the carbon X-ray peaks collected from both samples, under identical instrumental conditions (Fig. 6.1e). The area under the peak suggests that the amount of carbon deposited on sample treated with 5000 ppm C_2H_4 is more than 2.5 times higher than that on sample treated with 1000 ppm C_2H_4. Associated with each filament were the bright contrast particles at their tips. These nanoparticles were composed of Ni and Fe and it is encapsulated by the carbon layer. Examples of the filament with nanoparticle formed from 5000 ppm C_2H_4 is shown in the high-resolution image Fig. 6.2.

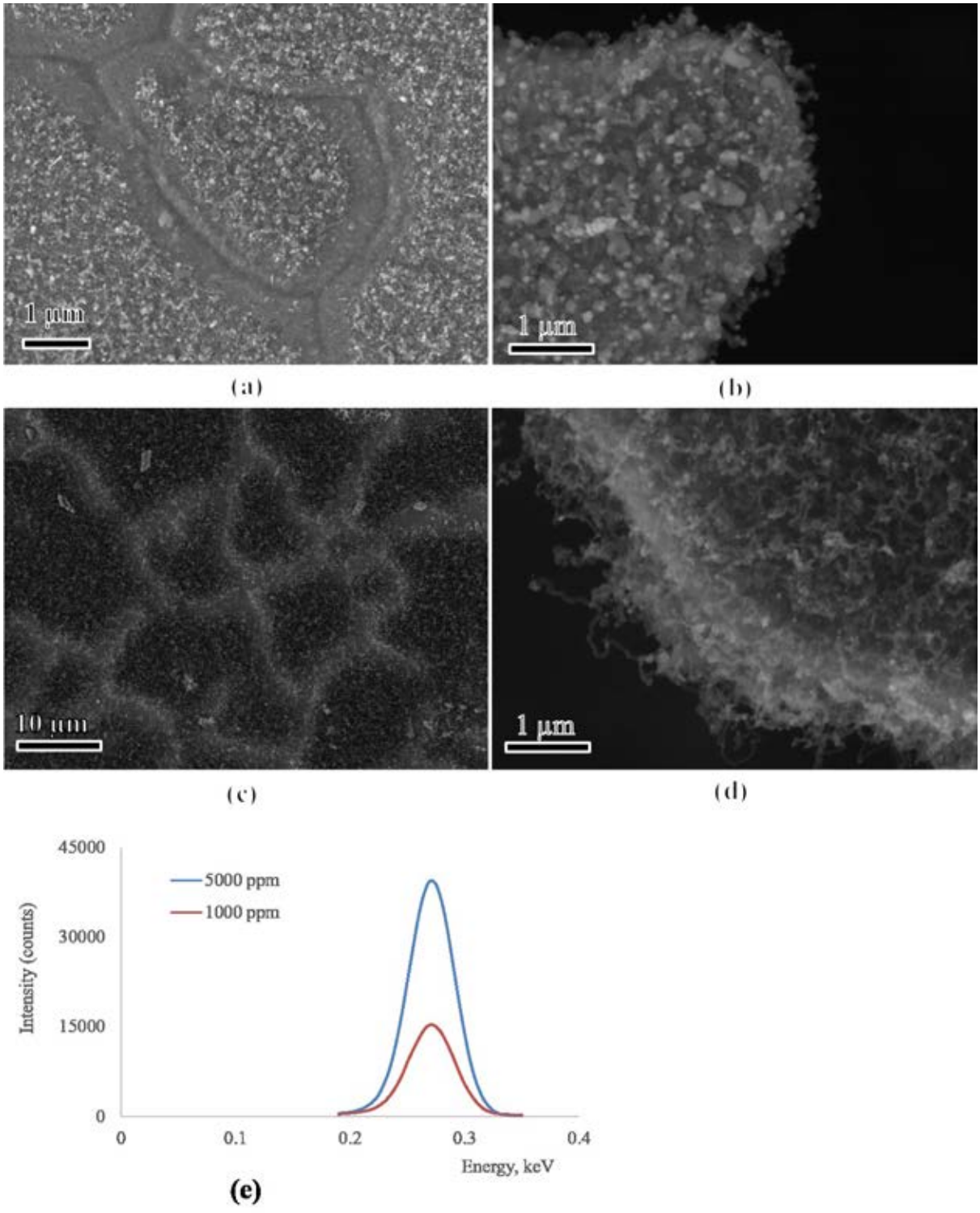

Fig. 6.1: SEM images of the surface of 20Cr-25Ni following the four hours treatment at 600°C to the sulphur-free carbon depositing gas mixture that contains, nominally (a), (b) 1000 ppm and (c), (d) 5000 ppm C_2H_4. (e) Carbon X-ray spectra collected from a surface area of 58 µm by 44 µm from both samples under identical electron microscope settings. Clearly, more carbon filaments were deposited from the gas containing a higher concentration of ethylene.

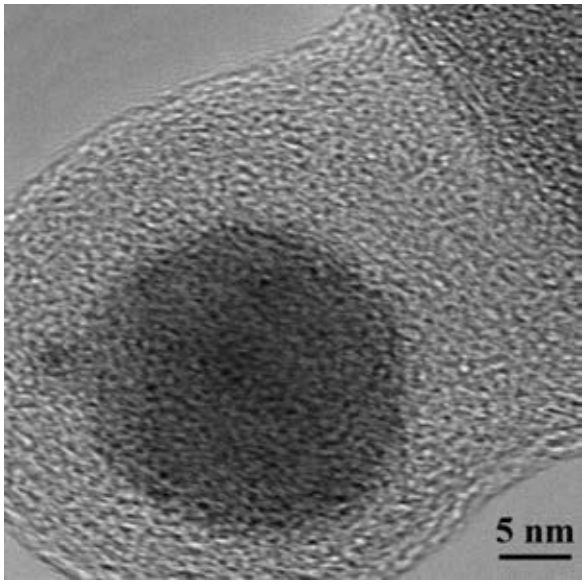

Fig. 6.2: A high magnification TEM image of carbon filament encapsulating a Ni-rich particle. The filament was produced from the sample reacted with depositing gas with 5000 ppm C_2H_4 for 4 h at 600 °C.

6.2. Effect of Various Sulphides on Carbon Deposition

The poisoning effectiveness of COS, H_2S and CH_3SH on carbon deposition on 20Cr-25Ni has been examined.

6.2.1. H_2S and COS with 1000 ppm C_2H_4

Fig. 6.3a shows the typical surface of the sample treated for 4 hours at 600 °C in 1000 ppm C_2H_4 with 215 ppb COS. No obvious carbon filaments were present on the surface. Instead, the centre of grains was scattered with faceted iron oxide and non-faceted, smaller nickel-rich particles (Fig. 6.3b). Occasionally non-filamentary carbon (noted as NFC) deposits were found with some particles attached, presumably nickel-rich. Using EDS and electron diffraction technique, the large micron-sized feature was identified as iron oxide.

A similar deposition result was obtained on a sample exposed to 1000 ppm ethylene bearing gas with 259 ppb H_2S, Fig. 6.3c. The surface was decorated with iron oxide and nickel-rich particles, and with some non-filamentary deposit Fig. 6.3d). In both cases, the carbon deposited on the samples has been reduced extensively, Fig. 6.3e and 3f. Semi-quant EDS

analysis suggests that the suppression effects of H_2S were similar to COS. The amount of carbon yield on both sulphur-containing samples relative to that from a sulphur-free deposition experiment was less than 0.07 (Table 6.1). SEM-EDS scan of the surface showed no presence of bulk sulphide.

Table 6.1: Carbon yield in the presence of sulphur species. All tests contained (nominally) 1000 ppm C_2H_4.

Gas	C X-ray Counts	Carbon Yield relative to S-free
S-free/1000 ppm C_2H_4	158000	1
215 ppb COS/1000 ppm C_2H_4	10000	0.06
259 ppb H_2S/1000 ppm C_2H_4	11000	0.07

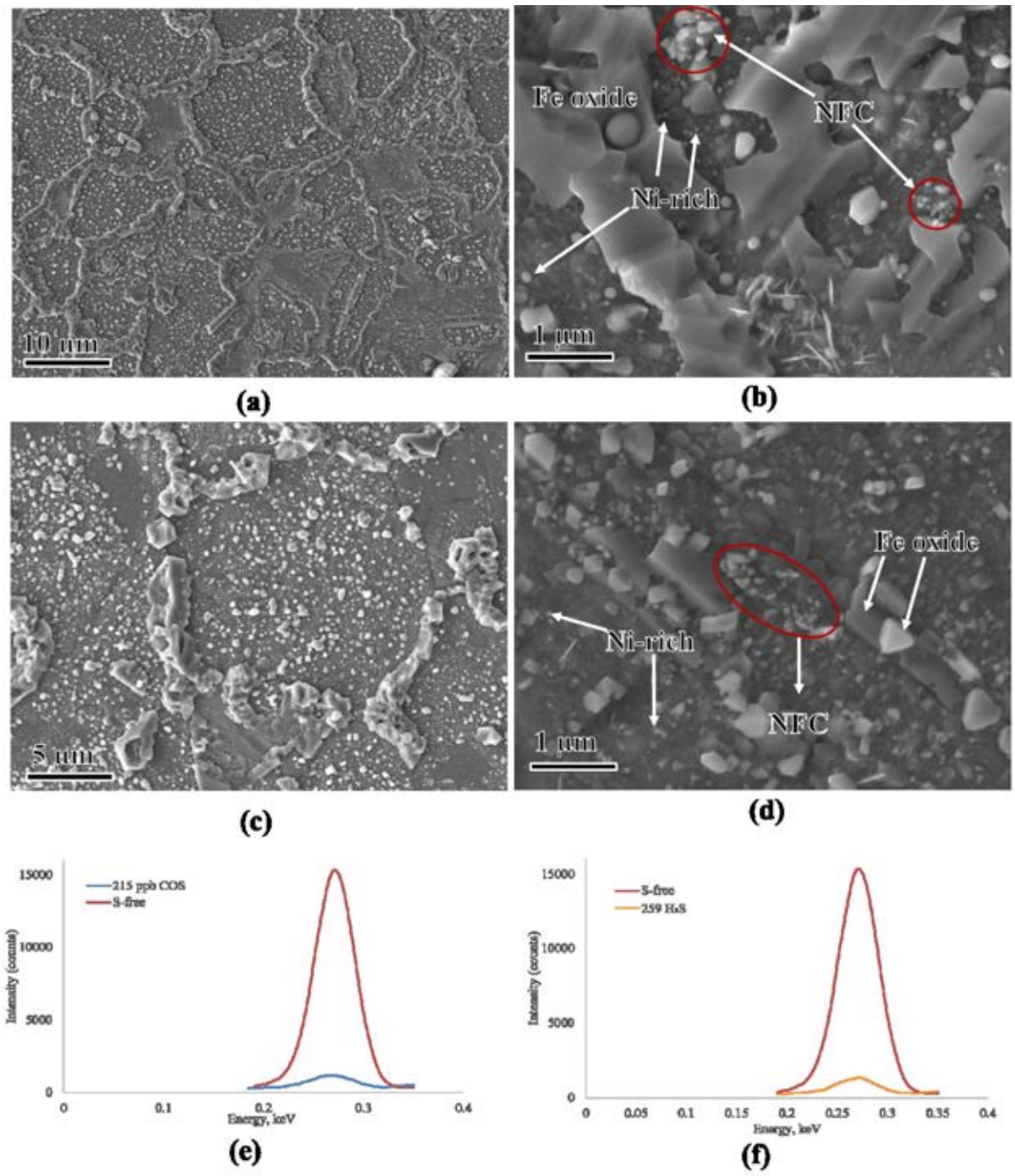

Fig. 6.3: SEM images of the surface of the sample following the 4 h exposure to sulphur-containing deposition gas with 1000 ppm C_2H_4 at 600 °C: (a), (b) 215 ppb COS; (c), (d) 259 ppb H_2S. (b) and (d) Higher magnification image showing the surface covered with Ni-rich particles and iron oxides. Some Ni-rich particles were held together by carbon deposit (noted as NFC). Carbon X-ray spectra collected from a surface area of 58 µm by 44 µm from both samples under identical electron microscope settings: (e) 215 COS and (f) 259 H_2S. For comparison, carbon X-ray spectra collected from the sulphur-free sample is also included.

6.2.2. H_2S, COS and CH_3SH with 5000 ppm C_2H_4

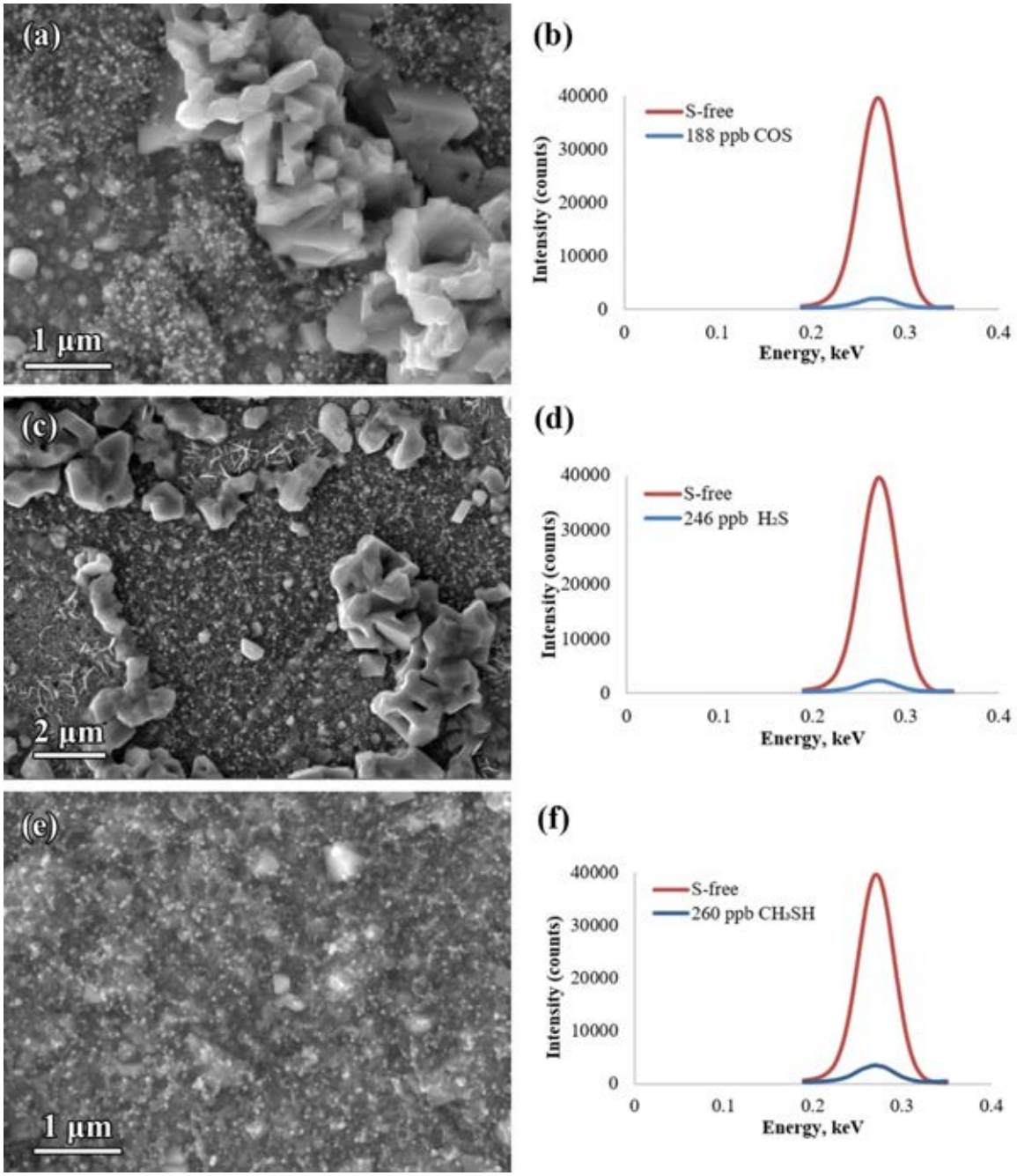

Fig. 6.4: SEM images of the surface of the sample following the 4 h exposure to sulphur-containing deposition gas with 5000 ppm C_2H_4 at 600 °C: (a) 188 ppb COS, (c) 246 ppb H_2S and (e) 260 ppb CH_3SH. Carbon X-ray spectra collected from a surface area of 58 µm by 44 µm from both samples under identical electron microscope settings: (b) 188 ppb COS, (d) 246 ppb H_2S and (f) 260 ppb CH_3SH. For comparison, carbon X-ray spectra collected from the sulphur-free sample is also included.

The effect of H_2S, COS and CH_3SH on carbon deposition rate from higher C_2H_4 concentration were also studied. SEM images of the surfaces of samples exposed to three different gases are shown in Fig. 6.4a, 4c and 4e. Although the deposition was reduced significantly from all three sulphur compounds, the formation of carbon filaments was not eliminated, even for COS and H_2S containing gas. SEM analysis of the surface suggested that the amounts of carbon present on samples exposed to COS and H_2S were similar but less than the carbon deposits on samples exposed to CH_3SH. The carbon X-ray peak collected from the 58 µm by 44 µm area, covering several grains from all three samples is shown in Fig. 6.4b, 4d and 4f. All three peaks from samples exposed to sulphur bearing depositing gas are significantly smaller compared to the C-K_α peak for the sulphur-free sample. As an estimate, based on the area under the peak, the carbon yield relative to that from the sulphur-free sample is listed in Table 6.2 Clearly, all three sulphur compounds have significantly reduced the amount of deposit (by a factor of 10) and CH_3SH was the least effective in suppressing deposition. SEM-EDS scan of the surface showed no presence of bulk sulphide.

Table 6.2: Carbon yield in the presence of sulphur species. All tests contained (nominally) 5000 ppm C_2H_4.

Gas	Counts	Carbon Yield relative to S-free
S-free/5000 ppm C_2H_4	451000	1
188 ppb COS/5000 ppm C_2H_4	19000	0.04
246 ppb H_2S/5000 ppm C_2H_4	21000	0.05
260 ppb CH_3SH/5000 ppm C_2H_4	34000	0.08

The carbon filaments formed on all samples were analysed using TEM. The images of carbon deposits in a cluster with nanoparticles are shown in Fig. 6.5 along with the filaments formed from sulphur-free depositing gas. It can be very clearly noticed from the images that the length of the filaments formed on all sulphur containing gas is smaller than that formed from the sulphur-free gas. A higher magnification image of the tip of filament showed that the

particle on all three sulphur containing samples was encapsulated by a carbon layer (see for example Fig. 6.6a). The identity of the Ni-rich nanoparticles was verified with EDS. Furthermore, EDS point analysis of the particle showed a presence of a small but clear sulphur peak on the spectrum. Repeated analysis of several particles showed that the sulphur peak was frequently visible when collected from the edge of the particles (which correspond to its surface) and less frequently visible when it was collected from the centre of particles (which correspond to its bulk). An example is shown in Fig. 6.6b where the spectra were collected from the edge (Position 2) and centre (Position 1) of the particle exposed to the COS-containing gas.

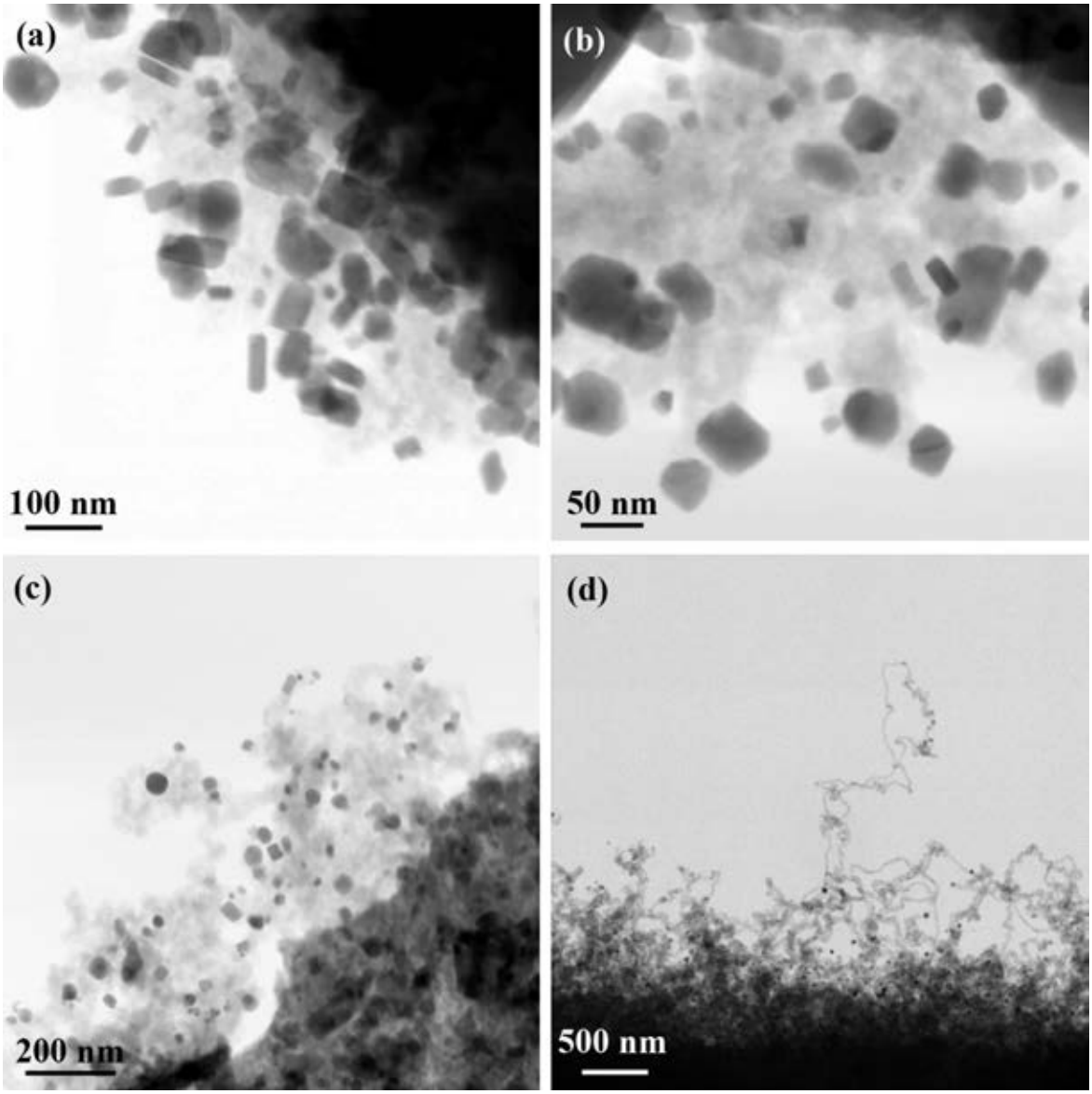

Fig. 6.5: TEM-BF images of filamentary carbon deposits formed on samples exposed to depositing gas that contains 5000 ppm C_2H_4 and (a) 188 ppb COS, (b) 246 ppb H_2S, (c) 260 ppb CH_3SH and (d) S-free.

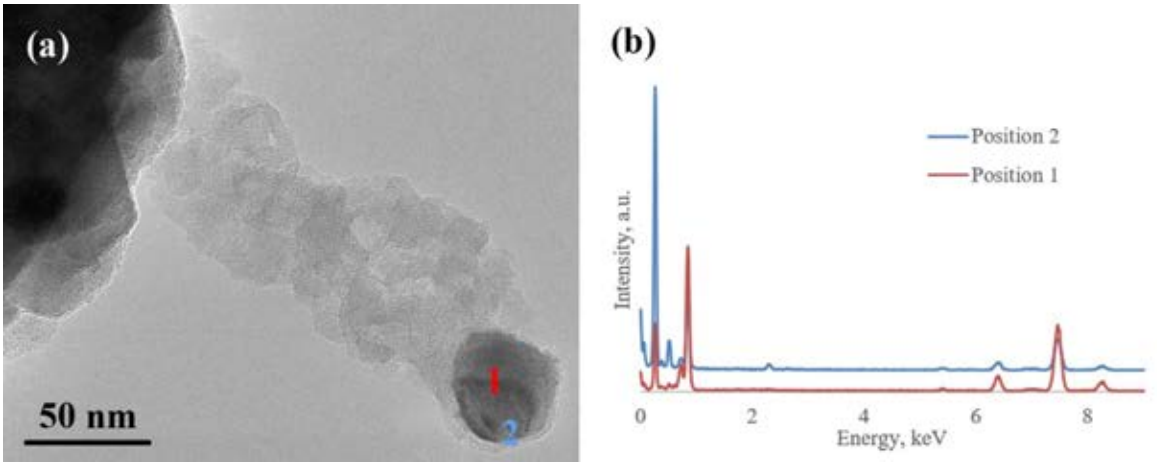

Fig. 6.6: (a) A higher magnification TEM-BF image of carbon filament produced on the sample reacted with 188 ppb COS and 5000 ppm C_2H_4 bearing depositing gas at 600°C. It clearly shows a thin layer of carbon encapsulated the Ni-rich particle. (b) EDS spectra collected at position 1 and 2 shown in (a). At position 2, which represents the edge of the particle, a sulphur peak is detected. In contrast, no sulphur peak was detected on the bulk, position 1.

6.2.3. STEM Analysis of Cross-section

In order to investigate the cross-section of the samples, thin TEM foils were prepared using FIB. The high angle annular dark field (HAADF) images of the cross-section through the oxide layer of the samples exposed to both sulphur-free and sulphur containing gases are shown in Fig. 6.7a – 7g. In all the samples, the subsurface oxide layer was composed of iron-chromium oxide layers (which was shown to be chromite, see Fig 5.11) and within this oxide layers, bright contrast Ni-rich features were located. Above this chromite layer, carbon deposits were discernible as dark contrast features along with the associated bright contrast Ni-rich catalyst. Several other particles that were not associated with the carbon deposits are also visible. These have been identified as iron oxide, namely magnetite (Fig. 6.7h).

Fig. 6.8a shows a STEM image acquired from the sample treated with 188 ppb COS bearing gas mixture for 4 h at 600°C. Fig. 6.8b shows the EDS point analysis of the particle and the surrounding oxide. A clear peak at 230 eV corresponding to the sulphur element was visible on the spectrum collected from the particle. No sulphur peak was detected on oxide. This

clearly demonstrates that the sulphur was associated with the Ni-rich particle. This trend was observed in all the samples that were treated with the sulphur-bearing gas.

The oxide thickness of chromite spinel was also measured from the foil extracted from the samples treated with both sulphur-free and sulphur containing gas mixture and it is listed in Table 6.3. Apart from the sample treated with 246 ppb H_2S/ 5000 ppm C_2H_4, the oxide on all the other samples treated with sulphur containing gas was thinner than that on the sample treated with sulphur-free gas.

Table 6.3: Measured thickness of (Fe, Cr) spinel on samples treated with various carbon depositing gas.

	Oxide Thickness (nm)	
Sulphur (ppb)	1000 ppm C_2H_4	5000 ppm C_2H_4
S-free	370-500	-
215 COS	100-350	-
259 H_2S	25-160	-
S-free	-	390-670
188 COS	-	100-200
246 H_2S	-	380-650
260 CH_3SH	-	160-300

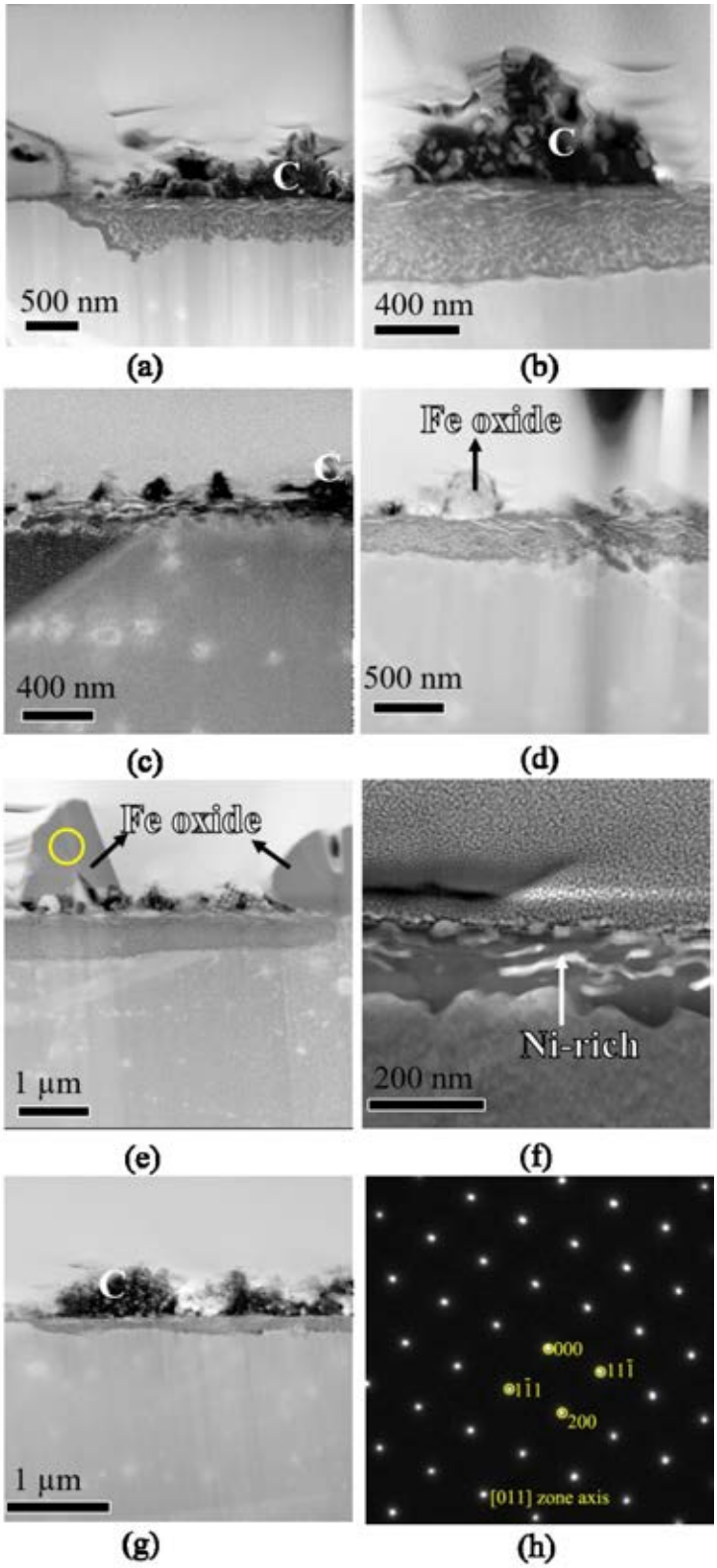

Fig. 6.7: STEM-HAADF images of cross-section of various samples treated at 600 °C in a depositing gas with (a) S-free/5000 ppm C_2H_4, (b) S-free/1000 ppm C_2H_4, (c) 188 ppb COS/5000 ppm C_2H_4, (d) 215 ppb COS/1000 ppm C_2H_4, (e) 246 ppb H_2S/5000 ppm C_2H_4, (f) 259 ppb H_2S/1000 ppm C_2H_4 and (g) 260 ppb CH_3SH/5000 ppm C_2H_4. (h) The diffraction pattern obtained from the micron-sized surface iron oxide, as shown in (e), is consistent with that of the FCC structured magnetite.

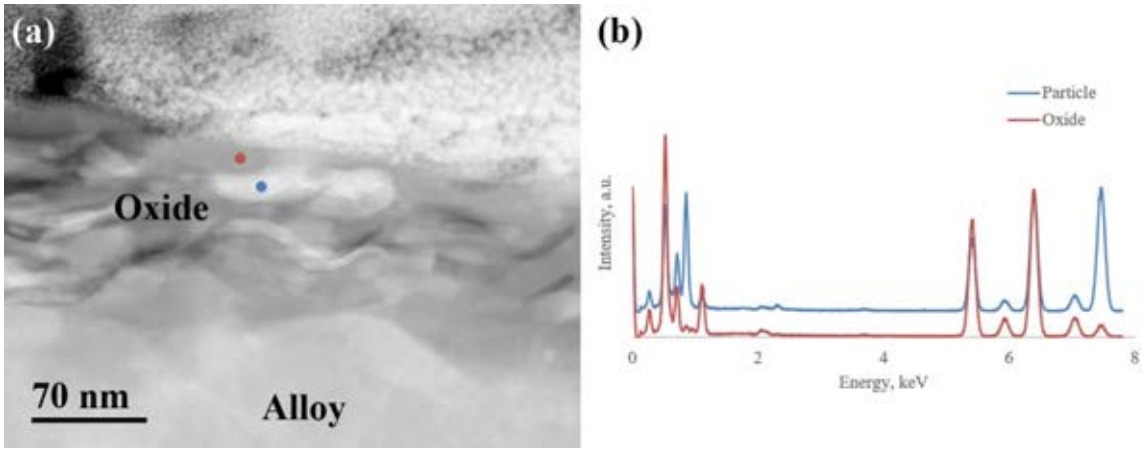

Fig. 6.8: (a) STEM-HAADF image of an oxide layer on sample exposed to depositing gas with 188 ppb COS and 5000 ppm C_2H_4. (b) EDS Point analysis of particle and oxide confirming the association of sulphur with the Ni-rich particle, but not with the oxide.

6.3 Discussion

6.3.1. Inhibition Role of Sulphur at 1000 ppm C_2H_4

It is generally accepted [75, 77, 78] that the mechanism for the formation of filamentary carbon from hydrocarbon involves adsorption and decomposition of hydrocarbon on the front side of particle, dissolution of adsorbed carbon atoms into the particle, diffusion of carbon through particle, and precipitation and growth of the carbon filament on the rear side of the particle. Any changes to these key steps can have a drastic effect on the growth of the carbon filament [81]. The rate controlling step in this mechanism is the diffusion of carbon through the catalyst. The driving force for carbon diffusion is either the temperature gradient [78, 75] created in the particle by the exothermic decomposition of hydrocarbon or the concentration gradient [77, 76] created by a difference in carbon activity at the particle/gas interface (front side) and at the particle/carbon interface (rear side). The growth of a filament is terminated when the surface is covered by a thin layer of excess carbon build-up.

Millward *et al*. [12] have shown that the metallic nickel or Ni-rich particles catalyse the growth of carbon filaments on 20Cr-25Ni steel when exposed to 1000 ppm C_2H_4 /1%

CO/CO_2. These particles are formed during the oxidation of steel under 1% CO/CO_2 at which nickel is the only alloying metal that does not oxidise [14]. It is clear from the present work that the addition of a trace amount of COS, H_2S and CH_3SH can reduce carbon deposition significantly. In some cases, the formation of carbon filaments was virtually eliminated. SEM-EDS analysis of the surfaces of all samples exposed to sulphur bearing gas showed that no bulk metal-sulphides were formed. However, STEM-EDS analysis of the Ni-rich particles located within the filament and oxide layer showed the presence of a trace amount of sulphur (see Fig. 6.6 and 6.9) which suggests that the sulphur was preferentially located at the surface of the Ni-rich particle.

Exposure of 20Cr-25Ni steel to 1000 ppm C_2H_4 /1% CO/ CO_2 with either 215 ppb COS or 259 ppb H_2S effectively suppressed the carbon deposition, and almost no carbon filaments were formed. This suggests that the sulphur coverage (θ_s) on nickel-rich particles was high, such that there are enough sulphur atoms on the surface to prevent ethylene accessing the critical sites on nickel surfaces for adsorption and decomposition, thus preventing the formation of filaments. Furthermore, it has been shown that the coadsorbed sulphur can lower the equilibrium coverage (and hence the dissolution) of adsorbed carbon on the nickel-rich particle [221, 222].

6.3.2. Inhibition Role of Sulphur at 5000 ppm C_2H_4

Although the amount of carbon deposition on the sulphur bearing depositing gas with a higher concentration of ethylene was reduced significantly, the formation of carbon filaments was not prevented. This is not unexpected, since increasing the ethylene concentration increases the activity of carbon (see Table 4.3), thus providing a more highly favourable environment for carbon deposition than the previous case. The effect of this increased carbon activity on the carbon deposition from the sulphur-free gas is clearly demonstrated in Fig. 6.1: the amount of carbon deposited from 5000 ppm C_2H_4 is increased by a factor of 2.5 than

that from 1000 ppm C_2H_4. When the sulphur was added to this high carbon depositing environment (5000 ppm C_2H_4), the deposition was suppressed, but not completely. This suggests that the sulphur coverage (θ_s) on nickel-rich particles was low such that, the adsorbed sulphur reduces the number of critical sites available for ethylene but does not prevent ethylene accessing the critical sites for adsorption-decomposition. Furthermore, at higher concentration of ethylene, the partial pressure of hydrogen P_{H_2} will also be higher due to the decomposition of C_2H_4 to C and H_2. For the H_2S reaction, since the sulphur activity a_s is inversely proportional to the P_{H_2} (see Appendix B)

$$a_s = K_{H_2S} \frac{P_{H_2S}}{P_{H_2}} \qquad \text{(from } H_2S \text{ decomposition)} \qquad (23)$$

increasing the $[C_2H_4]$ concentration may lower the sulphur activity and hence, the effectiveness of H_2S. P_{H_2S} is the partial pressure of H_2S and K_{H_2S} is the equilibrium constant.

It was clearly shown by the high magnification TEM image (see Fig. 6.6) of a carbon filament formed in the sulphur-bearing system that the growth of a filament was terminated when the particle was encapsulated by a carbon layer, similar to that in the sulphur-free system. The rate-controlling step in the filament growth in both systems was the bulk diffusion of carbon in the particle. With the introduction of sulphur it is possible that the diffusion characteristic of carbon was altered: the adsorbed sulphur could reduce the driving force for the diffusion of carbon as the heat (enthalpy) of adsorption-decomposition (temperature gradient) of ethylene is reduced due to reduction of critical surface-site available for ethylene and/or the concentration gradient is reduced as the coadsorbed sulphur lowers the carbon coverage on the exposed face of the particle. As a result of the low bulk diffusion rate of carbon, excess carbon can build-up at the surface such that encapsulation of particle is unavoidable. In other words, the catalyst is deactivated prematurely. This would explain the observed shorter carbon filament on sulphur bearing sample than that on the sulphur-free

sample (see Fig 6.5). The modification of bulk diffusion characteristic of carbon by various additives has been suggested by others as well. To account for the change in the growth mode of the relatively straight filament from sulphur-free particle to the coiled structure filament from pre-adsorbed sulphur, Owens *et al*. [183] reasoned that the pre-adsorbed sulphur modified the diffusion process. More relevant to the current case, Baker *et al*. [81] reported that by adding silica additive to Ni-Fe alloy the solubility and hence, the diffusion of carbon through the particle was reduced which resulted in the drastically slower linear growth rate and shorter filament than that from the unadulterated system (silica-free). Thus, all these effects (reduction of adsorption-decomposition reaction, dissolution and diffusion of carbon) from low sulphur coverage of particle would retard, but not prevent the carbon deposition process.

6.3.3. Suppressing Effect of CH_3SH relative to the H_2S and COS

It was demonstrated that the CH_3SH was the least effective poison in suppressing carbon deposition. This observation contradicts with the work reported by other groups [21, 22, 185, 223] who had claimed that the complex organic sulphide was more effective than the simpler sulphide like H_2S, COS and CS_2. Bennett *et al*. [22] speculated that the thiophene (C_4H_4S) was slightly more effective in inhibiting carbon deposition from acetone decomposition, as its larger molecular size block several adjacent sites. However, it should be noted that at the temperature used by Bennett and others [22], it is likely that thiophene will decompose completely into surface C and S atoms, and with H_2 as desorbed gas [224, 225, 226]. Furthermore, the partial pressure of thiophene was higher than the other sulphur compounds.

The possible explanation for this could be the decomposition of methanethiol into surface carbon (Fig. 6.9) that participates in filament growth: CH_3SH decomposes on nickel surface by S-H bond cleavage to form CH_3S and surface hydrogen, H_a [227, 228]. CH_3S decomposes by C-S bond scission to form CH_3 and surface sulphur, S_a. A methyl group (CH_3) would

decompose further into surface carbon and hydrogen. The adsorb hydrogen (H_a) would desorb as molecular hydrogen (H_2) but the adsorb carbon which bond strongly with nickel will stay on the surface. This adsorbed carbon will probably diffuse [227, 229] into bulk particle and precipitates as a filament, explaining the observed higher carbon deposition than that in H_2S and COS bearing gas. Alternatively, it is possible that the sulphur activity of this gas mixture is lower than that from the H_2S and COS bearing gas. Unfortunately, for the current work, it was not possible to determine the sulphur activities (Appendix 2).

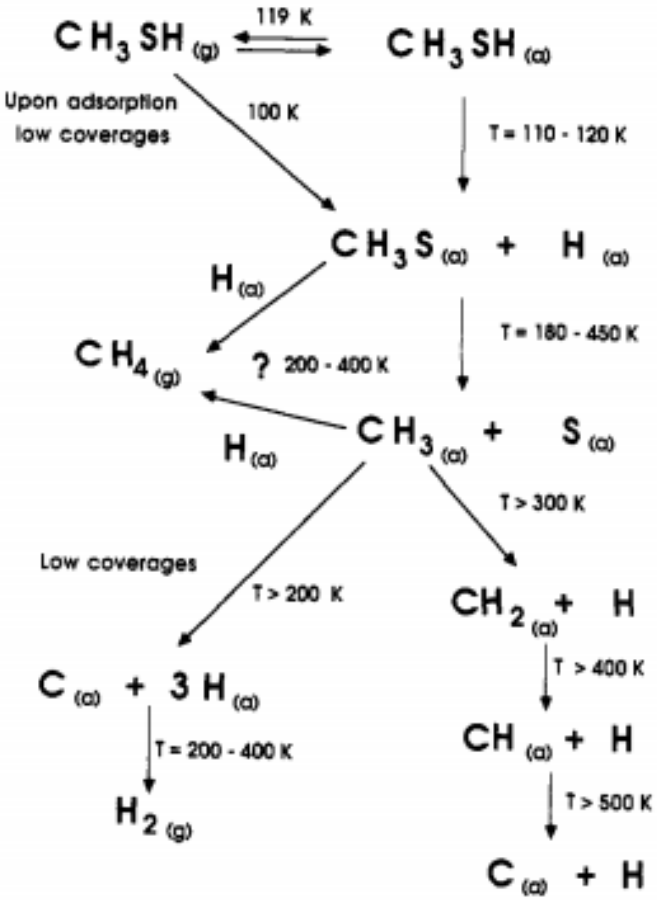

Fig. 6.9: Decomposition mechanism of methanethiol on Ni(100) *[227]*.

6.3.4. Oxide Thickness

In the current study, the thickness of the spinel (chromite) formed in the samples exposed to the sulphur-free gas mixture at 600 °C for 4 hours was thicker than that formed in the sulphur- containing gas mixture. In other words, the oxidation kinetics in the sulphur-

containing gas is slower. Although the role of sulphur on the oxidation kinetics has not been systematically studied, literature [230, 231] suggests that sulphur has an effect on the initial oxide nucleation. It was suggested that the initial oxidation requires adsorption of an oxygen molecule onto the metal surface, followed by the nucleation of oxide. However, when an alloy is exposed to a sulphur containing gas (such as COS, H_2S or CH_3SH in this case), it is probably that sulphur has a stronger affinity to the metal and adsorbs preferentially onto the surface of the alloy. To initiate the oxide formation, sulphur must first be replaced by oxygen. As a result of the competing surface adsorption, the initial oxidation process is slowed in the presence of sulphur.

6.3.5. Adsorption model

Hydrogen sulphide [217, 220] and carbonyl sulphide [232, 233] adsorb dissociatively on nickel by the following reactions:

$$H_2S\ (gas) + Ni\ (surface) = S_a + H_2\ (gas) \quad (24)$$

$$COS\ (gas) + Ni\ (surface) = S_a + CO\ (gas) \quad (25)$$

The estimate of the sulphur coverages, θ_s from reaction (24) is given by the empirical equation [234]:

$$\theta_s = 1.45 - 9.53\times10^{-5}.T + 4.17 \times 10^{-5}.T.\ln\left(\frac{P_{H_2S}}{P_{H_2}}\right) \quad (26)$$

where T is the temperature in K, P_{H_2S} and P_{H_2} are the partial pressure of H_2S and H_2 respectively.

Assuming that minimum sulphur coverage needed to eliminate the carbon filament is 80 % [195], the above eq. (26) would predict, for the current work (259 ppb H_2S/ 1000 ppm C_2H_4),

the hydrogen concentration to be at 150%. The maximum hydrogen concentration that can possibly exist is twice the concentration of C_2H_4 ~ 0.2% by the following reaction:

$$C_2H_4 + 2CO_2 = 2H_2 + 4CO \quad (27)$$

This model does not apply in the current work as it assumes Langmuir isotherm, i.e., non-competitive adsorption. Since the heat of adsorption of O on nickel surface is high (-469 kJ/mol at 800°C [235]), a competitive chemisorption reaction is provided by CO_2:

$$CO_2\ (gas) + Ni\ (surface) = O_a + CO(gas) \quad (28)$$

Using the Langmuir-Hinshelwood approach for two competitive reactions (eq. (25) and (28)), the following relationship can be derived [195] for sulphur coverage θ_S from COS (see Appendix A):

$$\theta_S = \frac{K_{24}[COS]}{K_{27} + [CO] + K_{24}[COS]} \quad (29)$$

where,

$$K_{24} = 3.17\exp\left(\frac{13000}{T}\right) \quad (30)$$

$$K_{27} = 13\exp\left(-\frac{3127}{T}\right) \quad (31)$$

For 215 ppb COS/1000 ppm C_2H_4/ 1%CO/ CO_2, the above equation estimates the sulphur coverage of 84%, at which inhibition of filamentary carbon can be expected. This agrees with the experimental observation (see Fig. 6.3). However, this expression also predicts the sulphur coverage of 82% for 188 ppb COS/ 5000 ppm C_2H_4/ 1%CO/ CO_2. This would imply that the carbon filament cannot be produced from 188 ppb COS bearing gas with a higher concentration of C_2H_4. Clearly, this is not the case (see Fig. 6.5a). It should be noted that this model does not consider the effect of C_2H_4. It was shown that the carbon deposition was more at higher concentration of C_2H_4. Several other studies [236, 237] have also reported that

the rate of carbon formation depends on the concentration (i.e., carbon activity) of carbon precursor. To predict the sulphur coverage of nickel on the carbon bearing environment the adsorption model must include the effect of the concentration of the carbon precursor.

7. Conclusion and Future Work

The current work was divided into two parts. The first part of the work was concerned with the formation of catalytic Ni-rich particles and identifying the inhibition mechanism of carbon deposition by COS. The second part was focused on the relative effects of various sulphur species on carbon deposition. The conclusions are summarised in section 7.1 and 7.2. The future work is in section 7.3.

7.1. The Formation Mechanism of the Nickel-rich Particles and the Inhibition Mechanism of Carbon Deposition due to the Addition of COS

Exposure to the gas mixture of about 1000 ppm C_2H_4/ 1% CO/ Bal. CO_2 at 600°C resulted in filamentary carbon deposition on the surface of a 20Cr-25Ni stainless steel. The carbon filaments were associated with metallic nickel-rich particles, consistent with literature reports that the carbon deposition was catalysed by these particles. Inhibition of this filamentary carbon deposition was achieved by adding 215 ppb of COS to the gas mixture. The following concluding remarks can be drawn from the electron microscopy studies performed in this work:

1. Nickel-rich metallic particles existed in the samples treated in both COS-free and COS-containing gas mixtures. Electron diffraction experiments confirmed that these nickel-rich particles assumed the same FCC crystal structure and orientation as the steel matrix and the lattice parameter was about 0.36 nm similar to that of the steel matrix. Nickel enrichment at the metal-oxide interface has also been observed. Under the current experimental conditions, both iron and chromium oxidised, leaving nickel enriched at the metal-oxide interface which became detached from the steel matrix with further oxidation. Therefore, these nickel-rich particles maintained the same crystal structure and orientation as that of the underneath steel matrix.

2. STEM-EDS results confirmed that sulphur concentrates on the surface of the nickel-rich particles and also at nickel-enriched regions at the metal-oxide interface. Although, it was not possible to be certain that sulphidation of nickel did not occur, however, based on thermodynamic consideration it is likely it did not. As such surface adsorption of sulphur can be regarded, at least in part, as the reason for the observed suppression of carbon deposition when treated in the COS-containing gas mixture.

7.2. The Effect of COS, H_2S and CH_3SH on Inhibiting Carbon Deposition on 20Cr-25Ni Steel.

The studies were carried out at two concentration levels of ethylene. It was found that the suppression effect of all three-sulphides depended on the concentration of ethylene. A trace amount of sulphur was preferentially located on the surface of a nickel-rich particle on all the samples exposed to sulphur bearing gas. Following are the concluding remarks drawn from this work:

1. The formation of carbon filaments was virtually eliminated, when the samples were exposed to 215 ppb COS/1000 ppm C_2H_4 and 259 ppb H_2S/1000 ppm C_2H_4 depositing gas at 600 °C. This was explained in terms of high sulphur coverage of the nickel catalyst such that the adsorbed sulphur physically blocked the adsorption and decomposition of C_2H_4 over the nickel-rich particles.
2. At higher concentration, 5000 ppm of C_2H_4, carbon deposition was suppressed by all three sulphur additives: 188 ppb COS, 246 ppb H_2S and 260 ppb CH_3SH. However, the complete inhibition was not achieved as the activity of carbon was higher. It was argued that the adsorbed sulphur coverage was low such that it reduces (but does not prevent) the number of critical sites available for adsorption-decomposition of ethylene and reduces the dissolution and diffusion of carbon atoms through the

particle. This resulted in the premature deactivation of the nickel catalyst and thus producing shorter filaments than that on the sulphur-free sample.

3. In both concentration levels of ethylene, the inhibition effect of COS and H_2S were similar. CH_3SH was the least effective sulphur poison. This was attributed to the decomposition of CH_3SH to the surface carbon atom that aided the deposition process.

4. In the current work, the oxide layer formed was thinner when sulphur compound was added than that without sulphur. This might be caused by the slowed oxide nucleation or the slowed diffusion across the metal-oxide interface when sulphur enriches, due to the strong nickel-sulphur affinity. Further work will be needed to clarify this.

7.3. Future Work

- Study of the effect of COS on the oxidation kinetics of 20Cr/25Ni/Nb steel in 1% CO/CO_2 without the presence of C_2H_4. This could later be extended to H_2S and other sulphur species.
- Develop the competitive adsorption model that depends on the carbon activity of the gas used. This work could be aided by the (chemical) analysis of the gas during the carbon deposition.
- Verify the effect of the molecular size of catalyst poison species on carbon deposition by using different sulphides such as thiophene - C_4H_4S, dimethyl sulphide - CH_3SCH_3 and dimethyl disulphide -CH_3SSCH_3. In particular, consideration must be given to thiophene as it was suggested to be more effective poison due to its larger molecular size. Furthermore, the gas phase must be analysed to monitor the thermal decomposition of sulphides.

- Study the sulphur poisoned Ni-rich particle using electron energy loss spectroscopy (EELS) and atom probe tomography (APT) to determine the chemical bonding and identities of the Ni-rich catalyst surfaces and the associated sulphur atom. This might be key to determining the nature of sulphur species i.e., chemisorbed or thin layer of nickel sulphide.
- As preliminary studies in the current work showed that more carbon was deposited on the sample prepared by chemical electropolishing than on the mechanically polished sample, it is of interest to investigate the effect of sample preparation methods on the carbon deposition process in the future.

8. Appendix

A: Adsorption Model

Assuming that the sulphur, S and oxygen, O atom compete for the same nickel-surface site (Ni-s), an adsorption isotherm can be derived (based on Langmuir-Hinshelwood approach) for the following two competitive reactions

$$CO_2 + Ni\ (Surface) \longrightarrow CO + O_a \tag{32}$$

$$COS + Ni\ (Surface) \longrightarrow CO + S_a \tag{33}$$

where O_a and S_a are the oxygen and sulphur atom adsorbed on a nickel surface.

Let θ_O, θ_S be the fraction of sites occupied by oxygen and sulphur such that,

$$\theta_E = 1 - \theta_O - \theta_S \tag{34}$$

where θ_E is an empty (unoccupied) sites that are available for adsorption.

For the oxygen adsorption reaction (32): the rate of adsorption of oxygen $R_{ads,O}$ (i.e. forward reaction of Eq. (32)) is directly proportional to the concentration of $[CO_2]$ and to the concentration/fraction of unoccupied sites

$$\text{i.e., } R_{ads,O} = K_{ads,O}[CO_2]\theta_E \tag{35}$$

where $K_{ads,O}$ is a proportionality constant for adsorption of oxygen.

The corresponding rate of desorption for O $R_{des,O}$ (i.e., backward reaction of Eq. (32) to form CO_2) is directly proportional to the concentration of $[CO]$ and to the fraction of sites occupied by oxygen

$$\text{i.e., } R_{des,O} = K_{des,O}[CO]\theta_O \tag{36}$$

where $K_{des,O}$ is a proportionality constant for desorption of oxygen.

At equilibrium, the rate of adsorption is equal to the rate of desorption,

$$R_{ads,O} = R_{des,O}$$

or,

$$K_{ads,O}[CO_2]\theta_E = K_{des,O}[CO]\theta_O \quad (37)$$

$$K_O[CO_2]\theta_E = [CO]\theta_O \quad (38)$$

where $K_O = K_{ads,O}/K_{des,O}$ is the equilibrium constant for reaction (32).

Similarly, for the sulphur adsorption reaction (33)

$$K_S[COS]\theta_E = [CO]\theta_S \quad (39)$$

with $K_S = K_{ads,S}/K_{des,S}$ as an equilibrium constant for the reaction (33).

Now substituting (34) on (38), the expression can be rearranged to obtain the surface coverage by oxygen, θ_O:

$$K_O[CO_2]\,(1 - \theta_O - \theta_S) = [CO]\theta_O \quad (40)$$

$$K_O[CO_2] - K_O[CO_2]\theta_O - K_O[CO_2]\theta_s = [CO]\theta_O \quad (41)$$

$$\theta_O(K_O[CO_2] + [CO]) = K_O[CO_2] - K_O[CO_2]\theta_s \quad (42)$$

$$\theta_O = \frac{K_O[CO_2] - K_O[CO_2]\theta_s}{(K_O[CO_2] + [CO])} \quad (43)$$

Combining this equation with (34) will give

$$\theta_E = 1 - \theta_S - \frac{K_O[CO_2] - K_O[CO_2]\theta_s}{(K_O[CO_2] + [CO])} \quad (44)$$

Finally, substituting (44) in (39)

$$[CO]\theta_S$$

$$= K_S[COS] - K_S[COS]\theta_S - K_S[COS]\left(\frac{K_O[CO_2] - K_O[CO_2]\theta_s}{(K_O[CO_2] + [CO])}\right)$$

$$= \frac{K_S[COS]K_O[CO_2] + K_S[COS][CO] - K_S[COS]\theta_S K_O[CO_2] - K_S[COS]\theta_S[CO] - K_S[COS]\,K_O[CO_2] + K_S[COS]K_O[CO_2]\theta_s}{(K_O[CO_2] + [CO])}$$

$$= \frac{K_S[COS][CO] - K_S[COS]\theta_S[CO]}{(K_O[CO_2] + [CO])}$$

$$\Longrightarrow \quad [CO]\theta_S\,(K_O[CO_2] + [CO]) = K_S[COS][CO] - K_S[COS]\theta_S[CO] \tag{45}$$

and solving for θ_S gives:

$$\theta_S(K_O[CO_2] + [CO] + K_S[COS]) = K_S[COS] \tag{46}$$

$$\theta_S = \frac{K_S[COS]}{K_O[CO_2] + [CO] + K_S[COS]} \tag{47}$$

Since the concentration of $[CO_2]$ is ~ 1,

$$\therefore \quad \theta_S = \frac{K_S[COS]}{K_S[COS] + K_O + [CO]} \tag{48}$$

B: Sulphur Activity

Recall the adsorption-decomposition reaction of H_2S and COS compounds:

$$H_2S + Ni\ (Surface) \longrightarrow H_2 + S_a \tag{49}$$

$$COS + Ni\ (Surface) \longrightarrow CO + S_a \tag{50}$$

At 600 °C, CH_3SH is likely to decompose by the following reaction:

$$CH_3SH + Ni\ (Surface) \longrightarrow 2H_2 + C_a + S_a \tag{51}$$

The sulphur activities for each of these reactions are

$$a_s = K_{H_2S} \frac{P_{H_2S}}{P_{H_2}} \quad \text{(from } H_2S \text{ decomposition)} \tag{52}$$

$$a_s = K_{COS} \frac{P_{COS}}{P_{CO}} \quad \text{(from COS decomposition)} \tag{53}$$

$$a_s = K_{CH_3SH} \frac{P_{CH_3SH}}{a_c P_{H_2}^2} \quad \text{(from } CH_3SH \text{ decomposition)} \tag{54}$$

where a_c is the activity of carbon, K_i and P_i are the equilibrium constant and partial pressure respectively.

From eq. (52) and (54), increasing the P_{H_2} ($[H_2]$ concentration) will lower the sulphur activities. At the higher concentration of $[C_2H_4]$, the activity of sulphur will decrease as more $[H_2]$ will form from the decomposition of C_2H_4. In addition, the sulphur activity from CH_3SH, eq. (54) depends (inversely proportional) on the activity of carbon.

For H_2S and CH_3SH, it is not possible to calculate the sulphur activities since the $[H_2]$ concentration (hence, P_{H_2}) is not known for the current work. However, the sulphur activity for COS can be estimated as the concentration of [COS] and [CO] are known.

The equilibrium constant (K) and enthalpies (ΔH) at 800 K for the reaction (50) are given below in Table B1.

Table B1: Equilibrium constant and enthalpy for COS reaction with a Ni surface at 800 K *[238]*.

Reaction	K (at 800 K)	$\Delta H_{800\,K}$ (kJ/mol)
$COS + Ni\ (Surface)$	1.45×10^7	-104.0

Using these values, the equilibrium constant at 873 K for the reaction (50) can be determined by applying the van't Hoff equation:

$$\frac{d(\ln K)}{dT} = \frac{\Delta H}{RT^2} \tag{55}$$

where K, ΔH, T and R are the equilibrium constant, standard enthalpy change, absolute temperature and gas constant respectively. The enthalpy change ΔH is assumed to be constant over the temperature range.

For the temperature range T_1 to T_2, the above differential equation can be expressed as

$$K_2 = K_1 \exp\left[-\frac{\Delta H}{R}\left(\frac{1}{T_2} - \frac{1}{T_1}\right)\right] \tag{56}$$

where K_1 and K_2 are the equilibrium constant at temperature T_1 and T_2, respectively.

The calculated equilibrium constant and the sulphur activity for the reaction (50) at 600 °C (873 K) is given in Table (B2).

Table B2: Calculated equilibrium constant and sulphur activity for COS reaction with Ni surface at 873 K.

Reaction	K (at 873 K)	Sulphur activity, a_s (at 873 K)	
		215 ppb COS/ 1% CO	188 ppb COS/ 1% CO
$COS + Ni\ (Surface)$	4.46×10^6	96	84

9. References

[1] M. R. Everett, D. V. Kinsey and E. Romberg, in *Chemistry and Physics of Carbon (ed. P. L. Walker Jr.)*, New York, Marcel Dekker, 1968, p. 289.

[2] A. Dyer, Gas Chemistry in Nuclear Reactors and Large Industrial Plants, London: Heyden, 1980.

[3] P. Biloen, J. N. Helle and W. M. H. Sachtler, "Incorporation of surface carbon into hydrocarbons during Fischer-Tropsch synthesis: Mechanistic implications," *Journal of Catalysis,* vol. 58, no. 1, p. 95, 1979.

[4] M. A. Vannice, "The Catalytic Synthesis of Hydrocarbons from Carbon Monoxide and Hydrogen," *Catalysis Reviews: Science and Engineering,* vol. 14, no. 1, p. 153, 1976.

[5] C. H. Bartholomew, "Carbon Deposition in Steam Reforming and Methanation," *Catalysis Reviews: Science and Engineering,* vol. 24, no. 1, p. 67, 1982.

[6] J. R. Rostrup-Nielsen, "Catalytic Steam Reforming," in *Catalysis (Science and Technology) (ed. J. R. Anderson and M. Boudart), vol. 5*, Berlin, Heidelberg, Springer, 1984, p. 1.

[7] P. M. L. G. M. Figueiredo J. L., "Carbon Deposition in Steam-Cracking," in *Fouling Science and Technology (ed. L. F. Melo, T. R. Bott and C. A. Bernardo) vol 145. ,*, Dordrecht, Springer, 1988, p. 425.

[8] D. E. Brown, J. T. K. Clark, A. I. Foster, J. J. McCarroll and M. L. Sims, "Inhibition of Coke Formation in Ethylene Steam Cracking," in *Coke Formation on Metal Surfaces (ed. L. F. Albright and R. T. K. Baker), vol 202*, American Chemical Society, 1983, p. 23.

[9] A. Holmen, O. A. Lindvaag and D. Trimm, "Surface Effects on the Steam Cracking of Propane," in *Coke Formation on Metal Surfaces (ed. L. F. Albright and R. T. K. Baker), vol 202*, American Chemical Society, 1982, p. 45.

[10] C. J. Wood, "Coolant Chemistry in CEGB Reactors," in *Gas Chemistry in Nuclear Reactors and Large Industrial Plant (ed. A. Dyer)*, London, Heyden, 1980, p. 6.

[11] E. Nonbøl, "Description of the Advanced Gas Cooled Type of Reactor (AGR)," Risø National Laboratory, Roskilde, Denmark, 1996.

[12] G. R. Millward, H. E. Evans, M. Aindow and C. W. Mowforth, "The Influence of Oxide Layers on the Initiation of Carbon Deposition on Stainless Steel," *Oxidation of Metals,* vol. 56, p. 231, 2001.

[13] R. A. Holm and H. E. Evans, "The resistance of 20 Cr/25 Ni steels to carbon deposition. IV: The influence of alloy silicon content," *Materials and Corrosion,* vol.

38, no. 5, p. 224, 1987.

[14] G. R. Millward, H. E. Evans, I. P. Jones and C. D. Eley, “Carbon deposition on stainless steel in oxidising environments,” *Materials at High Temperatures,* vol. 20, no. 4, p. 535, 2003.

[15] G. R. Millward, H. E. Evans, C. D. Eley and C. W. Mowforth, “The influence of carbonyl sulphide on the inhibition of filamentary carbon deposition on stainless steel,” *Materials and corrosion,* vol. 54, p. 864, 2003.

[16] W. J. Stephen, “The Effect of Temperature on the Inhibition of Carbon Deposition by Carbonyl Sulphide (Technical Report),” 2014.

[17] J. Knapp and M. Mignanelli, “Fuel Clad Equilibrium Calculations (Technical Report),” National Nuclear Laboratory, 2015.

[18] J. Large, “Measurement of Sulphur Species in the AGR Primary Circuit: Commissioning Report, (Technical Report),” AMEC, 2014.

[19] J. Large, “Hartlepool Primary Circuit Sulphur Measurements (Technical Report),” 2015.

[20] M. P. Taylor, H. E. Evans, P. Smith, R. Ding, Y. -L. Chiu, S. Rai, B. Connolly, N. Smith, L. Pearson and C. Mowforth, “The Effect of Temperature and Carbonyl Sulphide on Carbon Deposition on 20Cr25Ni Stainless Steel,” *Oxidation of Metals,* vol. 87, no. 5-6, p. 667, 2017.

[21] C. D. Tan and R. T. K. Baker, “The effect of various sulfides on carbon deposition on nickel–iron particles,” *Catalysis Today,* vol. 63, no. 1, p. 3, 2000.

[22] M. J. Bennett, G. H. Chaffey, B. L. Myatt and D. R. V. Silverster, “Inhibition by Sulfur Poisoning of the Heterogeneous Decomposition of Acetone,” in *Coke formation on metal surfaces (ed. L. F. Albright and R. T. K. Baker) , vol 202*, American Chemical Society, 1983, p. 223.

[23] C. W. (. E. Mowforth, *Private Communication,* 2015.

[24] R. W. Nichols, “Advances in Materials: Proceedings of a Symposium Organised by the North Western Branch of the Institution of Chemical Engineers,” in *Elsevier*, Manchester, 1964.

[25] R. A. Bailey, H. Clark, J. Ferris, S. Krause and R. Strong, “The nuclear environment,” in *Chemistry of the Environment*, Ronald Albert Bailey, 2002, p. 561.

[26] L. Granger and A. B. McIntosh, “British Nuclear Energy Conference Calder Symposium,” 1957.

[27] L. Owen, “Nuclear engineering in the United Kingdom-the First Ten Years,” *The Journal of the British Nuclear Energy Society,* vol. 2, no. 1, p. 23, 1963.

[28] H. K. Hardy, J. F. W. Bishop, D. O. Pickman and V. W. Eldred, “The development of uranium-magnox fuel elements for an average irradiation life of 3000 MWD/te,” *The Journal of the British Nuclear Energy Society,* vol. 2, no. 1, p. 33, 1963.

[29] C. Tyzack, C. S. Campbell and F. W. Trowse, “Compatibility problems in AGR systems,” *The Journal of the British Nuclear Energy Society,* vol. 2, no. 2, p. 246, 1963.

[30] G. Brown, G. Packman and G. B. Greenough, “Fuel Elements,” *The Journal of the British Nuclear Energy Society,* vol. 2, no. 2, p. 186, 1963.

[31] H. Kronberger, “AGR Research and Development Programme,” *The Journal of the British Nuclear Energy Society,* vol. 2, no. 2, p. 225, 1963.

[32] H. K. Hardy, L. M. Wyatt and S. F. Pugh, “Metallurgy of Fuel and Cans,” *The Journal of the British Nuclear Energy Society,* vol. 2, no. 2, p. 236, 1963.

[33] H. E. Evans and R. C. Lobb, “Conditions for the initiation of oxide-scale cracking and spallation,” *Corrosion Science,* vol. 24, no. 3, p. 209, 1984.

[34] H. E. Evans, “Spallation of oxide from stainless steel AGR nuclear fuel cladding: mechanisms and consequences,” *Materials Science and Technology,* vol. 4, no. 5, p. 414, 1988.

[35] A. M. Emsley and M. P. Hill, “High-temperature oxidation of a 20/25 stainless steel in high-pressure carbon dioxide,” *Oxidation of Metals,* vol. 33, no. 3-4, p. 265, 1990.

[36] J. M. Francis, M. T. Curtis and D. A. Hilton, “The oxidation and spalling behaviour of 20% Cr/25% Ni/Nb-stabilised steel under thermal cycling conditions,” *Journal of Nuclear Materials,* vol. 41, no. 2, p. 203, 1971.

[37] F. H. Fern and J. E. Antill, “A study of the high temperature oxidation behaviour of stainless steel using time lapse photomicrography,” *Corrosion Science,* vol. 10, no. 9, p. 649, 1970.

[38] W. A. England, M. J. Bennett, D. A. Greenhalgh, S. N. Jenny and C. F. Knights, “The characterization by raman spectroscopy of oxide scales formed on a 20Cr-25Ni-Nb stabilized stainless steel,” *Corrosion Science,* vol. 26, no. 7, p. 537, 1986.

[39] J. W. Tyler, “Characterization of the initial oxide formed on annealed and unannealed 20Cr-25Ni-Nb-stabilized steel in 50 torr CO2 at 973 K,” *Oxidation of Metals,* vol. 24, no. 3-4, p. 149, 1985.

[40] P. A. Tempest and R. K. Wild, “Formation and growth of spinel and Cr2O3 oxides on 20% Cr-25% Ni-Nb stainless steel in CO2 environments,” *Oxidation of Metals,* vol. 23, no. 3-4, p. 207, 1985.

[41] G. C. Allen, P. A. Tempest, J. W. Tyler and R. K. Wild, “Oxidation behavior of 20%Cr/25%Ni/Nb stabilized stainless steel in CO2 environments,” *Oxidation of*

Metals, vol. 21, no. 3-4, p. 187, 1984.

[42] P. A. Tempest and R. K. Wild, "The nature of the oxide formed on 20%Cr/25%Ni/Nb steel oxidised at 1123K in CO2," *Journal of Nuclear Materials,* vol. 102, p. 183, 1981.

[43] H. E. Evans, D. A. Hilton, H. A. Holm and S. J. Webster, "The development of localized pits during stainless steel oxidation," *Oxidation of Metals,* vol. 14, no. 3, p. 235, 1980.

[44] H. E. Evans, D. A. Hilton, R. A. Holm and S. J. Webster, "Influence of silicon additions on the oxidation resistance of a stainless steel," *Oxidation of Metals,* vol. 19, no. 1-2, p. 1, 1983.

[45] J. E. Antill, "Influence of Minor Alloying Elements on the High Temperature Oxidation Behaviour of a 20 % Cr-25 % Ni-Nb steeL," *Materials and Corrosion,* vol. 22, p. 513, 1971.

[46] R. C. Lobb and H. E. Evans, "An evaluation of the effect of surface chromium concentration on the oxidation of a stainless steel," *Corrosion Science,* vol. 23, no. 1, p. 55, 1983.

[47] R. C. Lobb and H. E. Evans, "A determination of the chromium concentration for 'healing' layer formation during the oxidation of chromium-depleted 20Cr-25Ni-Nb stainless steel," *Corrosion Science,* vol. 24, no. 5, p. 385, 1984.

[48] W. B. Jepson, J. E. Antill and J. B. Warburton, "The Oxidation and Carburisation of a 20/25/Nb Steel in Carbon Dioxide, in Carbon Monoxide and in Carbon Dioxide-Carbon Monoxide Mixtures," *British Corrosion Journal,* vol. 1, no. 1, p. 15, 1965.

[49] R. K. Wild, "Metal/oxide interface studies," *Spectrochimica Acta Part B: Atomic Spectroscopy,* vol. 40, no. 5-6, p. 827, 1985.

[50] P. A. Tempest and R. K. Wild, "Thickness measurements of spinel and chromia layers in stainless steel oxide scales by X-ray diffractometry," *Oxidation of Metals,* vol. 17, no. 5-6, p. 345, 1982.

[51] J. M. Francis, "Structure of Surface Oxides Formed on A 20% Cr/25% Ni/Nb-Stabilised Steel in Carbon Dioxide at High Temperatures," *British Corrosion Journal,* vol. 3, no. 3, p. 113, 1968.

[52] M. J. Bennett, "Beneficial and Detrimental Effects of Silica in the High Temperature Oxidation of 20Cr/25Ni/Nb Stainless Steel," *Key Engineering Materials,* Vols. 20-28, p. 3761, 1988.

[53] M. J. Bennett, J. A. Desport and P. A. Labun, "Analytical Electron Microscopy of a Selective Oxide Scale Formed on 20%Cr-25%Ni-Nb Stainless Steel," *Oxidation of Metals,* vol. 22, no. 5-6, p. 291, 1984.

[54] P. A. Tempest and R. K. Wild, "Internal report," Berkeley Nuclear Laboratory, 1982.

[55] H. E. Evans, D. A. Hilton and R. A. Holm, “Chromium-depleted zones and the oxidation process in stainless steels,” *Oxidation of Metals,* vol. 10, no. 3, p. 149, 1976.

[56] R. T. K. Baker, D. J. C. Yates and J. A. Dumesic, “Filamentous Carbon Formation over Iron Surfaces,” in *Coke Formation on Metal Surfaces (ed. L. F. Albright and R. T. K. Baker), vol 202*, American Chemical Society, 1983, p. 1.

[57] R. T. K. Baker, M. S. Kim, A. Chambers, C. Park and N. M. Rodriguez, “The relationship between metal particle morphology and the structural characteristics of carbon deposits,” *Studies in Surface Science and Catalysis,* vol. 111, p. 99, 1997.

[58] L. S. Lobo, J. L. Figueiredo and C. A. Bernardo, “Carbon formation and gasification on metals. Bulk diffusion mechanism: A reassessment,” *Catalysis Today,* vol. 178, no. 1, p. 110, 2011.

[59] T. V. Hughes and C. R. Chambers, “Manufacture of Carbon Filaments”. Patent U.S. Patent 405, 480, 18 June 1889.

[60] P. Schützenberger and L. Schützenberger, “Sur quelques faits relatifs à l’histoire du carbone,” *Comptes rendus de l'Académie des Sciences Paris,* vol. 111, p. 774, 1890.

[61] L. V. Radushkevich and V. M. Lukyanovich, “O strukture ugleroda, obrazujucegosja pri termiceskom razlozenii okisi ugleroda na zeleznom kontakte (About the structure of carbon formed by thermal decomposition of carbon monoxide on iron substrate),” *Zurn. Fisic. Chim.,* vol. 26, p. 88, 1952.

[62] M. Manning, J. E. Garmirian and R. C. Reid, “Carbon deposition studies using nickel and cobalt catalysts,” *Industrial & Engineering Chemistry Process Design and Development,* vol. 21, no. 3, p. 404, 1982.

[63] S. Iijima, “Helical microtubules of graphitic carbon,” *Nature ,* vol. 354, p. 56, 1991.

[64] P. Harris, Carbon Nanotube Science: Synthesis, Properties and Applications., Cambridge: Cambridge University Press, 2009.

[65] T. Baird, J. R. Fryer and B. Grant, “Structure of Fibrous Carbon,” *Nature,* vol. 233, p. 329, 1971.

[66] R. T. K. Baker, P. S. Harris, R. B. Thomas and R. J. Waite, “Formation of filamentous carbon from iron, cobalt and chromium catalyzed decomposition of acetylene,” *Journal of Catalysis,* vol. 30, no. 1, p. 86, 1973.

[67] J. R. Rostrup-Nielsen, “Equilibria of decomposition reactions of carbon monoxide and methane over nickel catalysts,” *Journal of Catalysis,* vol. 27, no. 3, p. 343, 1972.

[68] H. P. Boehm, “Carbon from carbon monoxide disproportionation on nickel and iron catalysts: Morphological studies and possible growth mechanisms,” *Carbon,* vol. 11, no. 6, p. 583, 1973.

[69] M. S. Kim, N. M. Rodriguez and R. T. K. Baker, "The role of interfacial phenomena in the structure of carbon deposits," *Journal of Catalysis,* vol. 134, no. 1, p. 253, 1992.

[70] P. K. de Bokx, A. J. H. M. Kock, E. Boellaard, W. Klop and J. W. Geus, "The formation of filamentous carbon on iron and nickel catalysts: I. Thermodynamics," *Journal of Catalysis,* vol. 96, no. 2, p. 454, 1985.

[71] A. J. H. M. Kock, P. K. de Bokx, E. Boellaard, W. Klop and J. W. Geus, "The formation of filamentous carbon on iron and nickel catalysts: II. Mechanism," *Journal of Catalysis,* vol. 96, no. 2, p. 468, 1985.

[72] I. Alstrup, "A new model explaining carbon filament growth on nickel, iron, and Ni-Cu alloy catalysts," *Journal of Catalysis,* vol. 109, no. 2, p. 241, 1988.

[73] A. Sacco Jr., P. Thacker, T. N. Chang and A. T. S. Chiang, "The initiation and growth of filamentous carbon from α-iron in H2, CH4, H2O, CO2, and CO gas mixtures," *Journal of Catalysis,* vol. 85, no. 1, p. 224, 1984.

[74] R. T. Yang and J. P. Chen, "Mechanism of carbon filament growth on metal catalysts," *Journal of Catalysis,* vol. 115, no. 1, p. 52, 1989.

[75] R. T. K. Baker, "Catalytic growth of carbon filaments," *Carbon,* vol. 27, no. 3, p. 315, 1989.

[76] J. -W. Snoeck, G. Froment and M. Fowles, "Filamentous Carbon Formation and Gasification: Thermodynamics, Driving Force, Nucleation, and Steady-State Growth," *Journal of Catalysis,* vol. 169, no. 1, p. 240, 1997.

[77] J. Rostrup-Nielsen and D. L. Trimm, "Mechanisms of carbon formation on nickel-containing catalysts," *Journal of Catalysis,* vol. 48, no. 1-3, p. 155, 1977.

[78] R. T. K. Baker, M. A. Barber, P. S. Harris, F. S. Feates and R. J. Waite, "Nucleation and growth of carbon deposits from the nickel catalyzed decomposition of acetylene," *Journal of Catalysis,* vol. 26, no. 1, p. 51, 1972.

[79] M. Manning and R. Reid, "C-H-O Systems in the Presence of an Iron Catalyst," *Industrial & Engineering Chemistry Process Design and Development,* vol. 16, no. 3, p. 358, 1977.

[80] J. R. Rostrup-Nielsen, "Sulfur-passivated nickel catalysts for carbon-free steam reforming of methane," *Journal of Catalysis,* vol. 85, no. 1, p. 31, 1984.

[81] R. T. K. Baker and J. J. Chludzinski Jr., "Filamentous carbon growth on nickel-iron surfaces: The effect of various oxide additives," *Journal of Catalysis,* vol. 64, no. 2, p. 464, 1980.

[82] R. T. K. Baker, "Electron Microscopy Studies of the Catalytic Growth of Carbon Filaments," in *Carbon Fibers Filaments and Composites (ed. J. L. Figueiredo, C. Bernardo, R. T. K. Baker and K. J. Hüttinger)*, Dordrecht, Kluwer Academic, 1990, p.

405.

[83] R. T. K. Baker and R. J. Waite, “Formation of carbonaceous deposits from the platinum-iron catalyzed decomposition of acetylene,” *Journal of Catalysis,* vol. 37, no. 1, p. 101, 1975.

[84] R. T. K. Baker, J. J. Chludzinski Jr., N. S. Dudash and A. J. Simoens, “The formation of filamentous carbon from decomposition of acetylene over vanadium and molybdenum,” *Carbon,* vol. 21, no. 5, p. 463, 1983.

[85] R. T. K. Baker and J. J. Chludzinski Jr., “In-situ electron microscopy studies of the behavior of supported ruthenium particles. 2. Carbon deposition from catalyzed decomposition of acetylene,” *The Journal of Physical Chemistry,* vol. 90, no. 20, p. 4734, 1986.

[86] C. P. Deck and K. Vecchio, “Prediction of carbon nanotube growth success by the analysis of carbon–catalyst binary phase diagrams,” *Carbon,* vol. 44, no. 2, p. 267, 2006.

[87] N. M. Rodriguez, A. Chambers and R. T. K. Baker, “Catalytic Engineering of Carbon Nanostructures,” *Langmuir,* vol. 11, no. 10, p. 3862, 1995.

[88] T. Baird, J. R. Fryer and B. Grant, “Carbon formation on iron and nickel foils by hydrocarbon pyrolysis—reactions at 700°C,” *Carbon,* vol. 12, no. 5, p. 591, 1974.

[89] A. Oberlin, M. Endo and T. Koyama, “Filamentous growth of carbon through benzene decomposition,” *Journal of Crystal Growth,* vol. 32, no. 3, p. 335, 1976.

[90] A. Sacco Jr., “Carbon Deposition and Filament Initiation and Growth Mechanisms on Iron Particles and Foils,” in *Carbon Fibers Filaments and Composites (ed. J. L. Figueiredo, C. Bernardo, R. T. K. Baker and K. J. Hüttinger)*, Dordrecht, Springer, 1990, p. 459.

[91] G. G. Tibbetts, “Physical Modeling of Carbon Filament Growth,” in *Carbon Fibers Filaments and Composites (ed. J. L. Figueiredo, C. Bernardo, R. T. K. Baker and K. J.Hüttinger)*, Dordrecht, Kluwer Academic, 1990, p. 525.

[92] T. Massaro and E. Petersen, “Bulk Diffusion of Carbon-14 through Polycrystalline Nickel Foil between 350 and 700°C,” *Journal of Applied Physics,* vol. 42, p. 5534, 1971.

[93] R. Seidel, G. S. Duesberg, E. Unger, A. P. Graham, M. Liebau and F. Kreupl, “Chemical Vapor Deposition Growth of Single-Walled Carbon Nanotubes at 600 °C and a Simple Growth Model,” *The Journal of Physical Chemistry B,* vol. 108, no. 6, p. 1888, 2004.

[94] S. Hofmann, G. Csányi, A. C. Ferrari, M. C. Payne and J. Robertson, “Surface Diffusion: The Low Activation Energy Path for Nanotube Growth,” *Physical Review Letters,* vol. 95, no. No. 036101, p. 036101, 2005.

[95] J. -Y. Raty, F. Gygi and G. Galli, “Growth of Carbon Nanotubes on Metal Nanoparticles: A Microscopic Mechanism from Ab Initio Molecular Dynamics Simulations,” *Physical Review Letters,* vol. 95, p. 096103, 2005.

[96] S. Helveg, C. López-Cartes, J. Sehested, P. L. Hansen, B. S. Clausen, J. R. Rostrup-Nielsen, F. Abild-Pedersen and J. K. Nørskov, “Atomic-scale imaging of carbon nanofibre growth,” *Nature,* vol. 427, p. 426, 2004.

[97] S. Helveg and P. L. Hansen, “Atomic-scale studies of metallic nanocluster catalysts by in situ high-resolution transmission electron microscopy,” *Catalysis Today,* vol. 111, no. 1-2, p. 68, 2006.

[98] V. J. J. Kehrer and H. J. Leidheiser, “The Catalytic Decomposition of Carbon Monoxide on Large Metallic Single Crystals,” *The Journal of Physical Chemistry ,* vol. 58, no. 7, p. 550, 1954.

[99] S. D. Robertson, “Carbon formation from methane pyrolysis over some transition metal surfaces—I. Nature and properties of the carbons formed,” *Carbon,* vol. 8, no. 3, p. 365, 1970.

[100] C. W. Keep, S. Terry and G. R. Gadsby, “The Effect of Surface Pretreatment on the Growth of Carbon onto Stainless Steel from the Decomposition of Propane,” in *Gas Chemistry in Nuclear Reactors and Large Industrial Plant (ed. A. Dyer)*, London, Heyden, 1980, p. 40.

[101] G. W. Horsley and J. A. Cairns, “The inhibition of carbon deposition on stainless steel by prior selective oxidation,” *Application of Surface Science,* vol. 18, no. 3, p. 273, 1984.

[102] D. C. W. Blaikley and N. Jorgensen, “Studies of catalytically enhanced carbon deposition and removal using a gas plasma system,” *Catalysis Today,* vol. 7, p. 277, 1990.

[103] M. J. Durbin and J. E. Castle, “Carbon deposition from acetone during oxidation of iron—the effects of chromium and nickel,” *Carbon,* vol. 14, no. 1, p. 27, 1976.

[104] S. Waher, “The influence of surface oxide composition and structure on carburization in carburization in carbon monoxide – carbon dioxide,” *Materials and Corrosion,* vol. 26, no. 12, p. 936, 1975.

[105] H. J. Grabke, R. Krajak and J. C. Nava Paz, “On the mechanism of catastrophic carburization: ‘metal dusting’,” *Corrosion Science,* vol. 35, no. 5-8, p. 1141, 1993.

[106] S. Hofmann, R. Blume, C. T. Wirth, M. Cantoro, R. Sharma, C. Ducati, M. Hävecker, S. Zafeiratos, P. Schnoerch, A. Oestereich, D. Teschner, M. Albrecht, A. Knop-Gericke, R. Schlögl and J. Robertson, “State of Transition Metal Catalysts During Carbon Nanotube Growth,” *The Journal of Physical Chemistry C,* vol. 113, no. 5, p. 1648, 2009.

[107] M. Audier, M. Coulon and A. Oberlin, “Relative crystallographic orientations of carbon and metal in a filamentous catalytic carbon,” *Carbon,* vol. 18, no. 1, p. 73, 1980.

[108] M. Audier, P. Bowen and W. Jones, “Electron microscopic and mössbauer study of the iron carbides θ-Fe3C and X-Fe5C2 formed during the disproportionation of CO,” *Journal of Crystal Growth,* vol. 64, no. 2, p. 291, 1983.

[109] W. R. Ruston, M. Warzee, J. Hennaut and J. Waty, “The solid reaction products of the catalytic decomposition of carbon monoxide on iron at 550°C,” *Carbon,* vol. 7, no. 1, p. 47, 1969.

[110] A. Sacco Jr. and J. C. Caulmare, “Growth and Initiation Mechanism of Filamentous Coke,” in *Coke Formation on Metal Surfaces (ed. L. F. Albright and R. T. K. Baker), vol. 202*, American Chemical Society, 1983, p. 177.

[111] G. D. Renshaw, C. Roscoe and P. L. J. Walker, “Disproportionation of CO: I. Over iron and silicon-iron single crystals,” *Journal of Catalysis,* vol. 18, no. 2, p. 164, 1970.

[112] I. Stewart, M. J. Tricker and J. A. Cairns, “Application of Conversion Electron Mossbauer Spectroscopy to the study of carbon deposition on iron,” *Journal of Catalysis,* vol. 94, no. 2, p. 360, 1985.

[113] G. G. Tibbetts, M. G. Devour and E. J. Rodda, “An adsorption-diffusion isotherm and its application to the growth of carbon filaments on iron catalyst particles,” *Carbon,* vol. 25, no. 3, p. 367, 1987.

[114] M. Lin, J. P. Y. Tan, C. Boothroyd, K. P. Loh, E. S. Tok and Y. -L. Foo, “Direct Observation of Single-Walled Carbon Nanotube Growth at the Atomistic Scale,” *Nano Letters,* vol. 6, no. 3, p. 449, 2006.

[115] S. Hofmann, R. Sharma, C. Ducati, G. Du, C. Mattevi, C. Cepek, M. Cantoro, S. Pisana, A. Parvez, F. Cervantes-Sodi, A. C. Ferrari, R. Dunin-Borkowski, S. Lizzit, L. Petaccia, A. Goldoni and J. Robertson, “In situ Observations of Catalyst Dynamics during Surface-Bound Carbon Nanotube Nucleation,” *Nano Lett.,* vol. 7, no. 3, p. 602, 2007.

[116] J. Nava Paz and H. Grabke, “Metal dusting,” *Oxidation of Metals,* vol. 39, no. 5-6, p. 437, 1993.

[117] H. J. Grabke, “Metal Dusting of Low- and High-Alloy Steels,” *CORROSION SCIENCE,* vol. 51, no. 9, p. 711, 1995.

[118] H. J. Grabke, “Thermodynamics, mechanisms, and kinetics of metal dusting,” *Materials and Corrosion,* vol. 49, no. 5, p. 303, 1998.

[119] H. J. Grabke, R. Krajak, E. M. Müller-Lorenz and S. Strauß, “Metal dusting of nickel-base alloys,” *Materials and Corrosion,* vol. 47, p. 495, 1996.

[120] R. T. K. Baker, J. R. Alonzo, J. A. Dumesic and D. J. C. Yates, "Effect of the surface state of iron on filamentous carbon formation," *Journal of Catalysis,* vol. 77, no. 1, p. 74, 1982.

[121] E. T. Turkdogan and J. V. Vinters, "Catalytic effect of iron on decomposition of carbon monoxide: I. carbon deposition in H2-CO Mixtures," *Metallurgical Transactions,* vol. 5, no. 1, p. 11, 1974.

[122] P. L. Walker Jr., J. F. Rakszawski and G. R. Imperial, "Carbon Mixture over Iron Catalysts. II. Rates of Carbon Formation," *The Journal of Physical Chemistry,* vol. 63, no. 2, p. 140, 1959.

[123] B. Chatterjee and P. P. Das, "Nature of the Catalyst in the Decomposition of Carbon Monoxide in Presence of Iron," *Nature,* vol. 173, p. 1046, 1954.

[124] K. L. Yang and R. T. Yang, "The accelerating and retarding effects of hydrogen on carbon deposition on metal surfaces," *Carbon,* vol. 24, no. 6, p. 687, 1986.

[125] E. C. Bianchini and C. R. F. Lund, "Kinetic implications of mechanisms proposed for catalytic carbon filament growth," *Journal of Catalysis,* vol. 117, no. 2, p. 455, 1989.

[126] F. Bonnet, F. Ropital, Y. Berthier and P. Marcus, "Filamentous carbon formation caused by catalytic metal particles from iron oxide," *Materials and Corrosion,* vol. 54, no. 11, p. 870, 2003.

[127] C. Emmenegger, J. -M. Bonard, P. Mauron, P. Sudan, A. Lepora, B. Grobety, A. Züttel and L. Schlapbach, "Synthesis of carbon nanotubes over Fe catalyst on aluminium and suggested growth mechanism," *Carbon,* vol. 41, no. 3, p. 539, 2003.

[128] K. Nishimura, N. Okazaki, L. J. Pan and Y. Nakayama, "In Situ Study of Iron Catalysts for Carbon Nanotube Growth Using X-Ray Diffraction Analysis," *Japanese Journal of Applied Physics,* vol. 43, no. 2, p. L471, 2004.

[129] C. Mattevi, S. Hofmann, M. Cantoro, A. C. Ferrari, J. Robertson, C. Castellarin-Cudia, S. Dolafi, A. Goldoni and C. Cepek, "Surface-bound chemical vapour deposition of carbon nanotubes: In situ study of catalyst activation," *Physica E: Low-dimensional Systems and Nanostructures,* vol. 40, no. 7, p. 2238, 2008.

[130] L. Ni, K. Kuroda, L.-P. Zhou, K. Ohta, K. Matsuishi and J. Nakamura, "Decomposition of metal carbides as an elementary step of carbon nanotube synthesis," *Carbon,* vol. 47, no. 13, p. 3054, 2009.

[131] M. V. Kharlamova, "Investigation of growth dynamics of carbon nanotubes," *Beilstein Journal of Nanotechnology,* vol. 8, p. 826, 2017.

[132] C. H. Toh, P. R. Munroe and D. J. Young, "Metal Dusting of Fe–Cr and Fe–Ni–Cr Alloys Under Cyclic Conditions," *Oxidation of Metals,* vol. 58, no. 1-2, p. 1, 2002.

[133] C. H. Toh, P. R. Munroe and D. J. Young, "The role of cementite in the metal dusting of Fe–Cr and Fe–Ni–Cr Alloys," *Materials at High Temperatures,* vol. 20, no. 4, p.

527, 2003.

[134] J. R. Bradley, Y. -L. Chen and H. W. Sturner, "The structure of carbon filaments and associated catalytic particles formed during pyrolysis of natural gas in steel tubes," *Carbon,* vol. 23, no. 6, p. 715, 1985.

[135] Z. Zeng and K. Natesan, "Relationship between the Growth of Carbon Nanofilaments and Metal Dusting Corrosion," *Chemistry of Materials,* vol. 17, no. 14, p. 3794, 2005.

[136] R. T. K. Baker and P. S. Harris, "The formation of filamentous carbon," in *Chemistry and Physics of Carbon (ed. P. L. Walker, Jr. and P. A. Thrower), vol. 14*, New York, Marcel Dekker, 1978, p. 83.

[137] B. Ozturk, V. L. Fearing, J. A. Ruth and G. Simkovich, "Self-Diffusion Coefficients of Carbon in Fe3C at 723 K via the Kinetics of Formation of This Compound," *Metallurgical Transactions A,* vol. 13, no. 10, p. 1871, 1982.

[138] H. Yoshida, S. Takeda, T. Uchiyama, H. Kohno and Y. Homma, "Atomic-Scale In-situ Observation of Carbon Nanotube Growth from Solid State Iron Carbide Nanoparticles," *Nano Letters,* vol. 8, no. 7, p. 2082, 2008.

[139] I. Wolf and H. J. Grabke, "A study on the solubility and distribution of carbon in oxides," *Solid State Communications,* vol. 54, no. 1, p. 5, 1985.

[140] S. Tokura, N. Otsuka and T. Kudo, "Coke Formation on Preoxidized Iron and Nickel in a CH4-H2 Gas Atmosphere at 1,000°C," *CORROSION SCIENCE,* vol. 49, no. 7, p. 561, 1993.

[141] C. Steurbaut, H. J. Grabke, F. R. van Buren, S. J. Korf and J. De-francq, "Kinetic studies of coke formation and removal onHP40 in cycled atmospheres at high temperatures," *MATERIALS AND CORROSION,* vol. 49, no. 5, p. 352, 1998.

[142] H. J. Grabke, "Coking caused by fine metal particles from oxide reduction," *Materials and Corrosion,* vol. 50, no. 12, p. 673, 1999.

[143] R. T. K. Baker, G. R. Gadbsy and S. Terry, "Formation of carbon filaments from catalysed decomposition of hydrocarbons," *Carbon,* vol. 13, no. 3, p. 245, 1975.

[144] R. T. Yang and K. L. Yang, "Mechanism of coke deposition on the surface of molybdenite," *Journal of Catalysis,* vol. 90, no. 2, p. 194, 1984.

[145] R. T. Yang and K. L. Yang, "Evidence for temperature-driven carbon diffusion mechanism of coke deposition on catalysts," *Journal of Catalysis,* vol. 93, no. 1, p. 182, 1985.

[146] S. D. Robertson, "Carbon formation from methane pyrolysis over some transition metal surfaces—II. Manner of carbon and graphite formation," *Carbon,* vol. 10, no. 2, p. 221, 1972.

[147] E. L. Evans, J. M. Thomas, P. A. Thrower and P. L. Walker, “Growth of filamentary carbon on metallic surfaces during the pyrolysis of methane and acetone,” *Carbon,* vol. 11, no. 5, p. 441, 1973.

[148] C. W. Keep, R. T. K. Baker and J. A. France, “Origin of filamentous carbon formation from the reaction of propane over nickel,” *Journal of Catalysis,* vol. 47, no. 2, p. 232, 1977.

[149] E. Boellaard, P. K. dE Bokx, A. Kock and J. W. Geus, “The formation of filamentous carbon on iron and nickel catalysts: III. Morphology,” *Journal of Catalysis,* vol. 96, no. 2, p. 481, 1985.

[150] A. I. F.-R. E. D. I. L. LaCava and M. Caraballo, “Effect of Hydrogen on the Iron- and Nickel-Catalyzed Formation of Carbon from Benzene,” in *Coke Formation on Metal Surfaces, L. F. Albright, R. T. K. Baker (Eds.)*, New York, American Chemical Society, 1982, p. 89.

[151] H. Leidheiser Jr. and A. T. Gwathmey, “The Selective Deposition of Carbon on the (111) Face of a Nickel Crystal in the Catalytic Decomposition of Carbon Monoxide,” *Journal of the Amercian Chemical Society,* vol. 70, p. 1206, 1948.

[152] V. J. Kehrer Jr. and H. Leidheiser Jr., “The Catalytic Decomposition of Carbon Monoxide on Large Metallic Single Crystals,” *The Journal of Physical Chemistry ,* vol. 58, p. 550, 1954.

[153] H. E. Grenga and K. R. Lawless, “Active Sites for Heterogeneous Catalysis,” *Journal of Applied Physics ,* vol. 43, p. 1508, 1972.

[154] J. Zhang, C. Kong and D. J. Young, “Surface orientation effects on initial carbon deposition and metal dusting of nickel,” *Materials at High Temperatures,* vol. 26, p. 45, 2009.

[155] Schouten, F. C., O. L. J. Gijzeman and G. A. Bootsma, “Interaction of methane with Ni(111) and Ni(100); diffusion of carbon into nickel through the (100) surface; An aes-leed study,” *Surface Science,* vol. 87, p. 1, 1979.

[156] M. Eizenberg and J. M. Blakely, “Carbon interaction with nickel surfaces: Monolayer formation and structural stability,” *The Journal of Chemical Physics,* vol. 71, p. 3467, 1979.

[157] J. C. Hamilton and J. M. Blakely, “Carbon segregation to single crystal surfaces of Pt, Pd and Co,” *Surface Science,* vol. 91, p. 199, 1980.

[158] A. E. B. Presland and P. L. Walker Jr., “Growth of single-crystal graphite by pyrolysis of acetylene over metals,” *Carbon,* vol. 7, p. 1, 1969.

[159] A. A. Dost, V. R. Dhanak and D. W. Bassett, “Field emission microscope studies of carbon on nickel surfaces,” *Vacuum,* vol. 33, p. 687, 1983.

[160] H. S. Bengaard, J. K. Nørskov, J. Sehested, B. S. Clausen, L. P. Nielsen, A. M. Molenbroek and J. R. Rostrup-Nielsen, "Steam Reforming and Graphite Formation on Ni Catalysts," *Journal of Catalysis,* vol. 209, p. 365, 2002.

[161] Y. Wang, A. J. Page, H. B. Li, H. J. Qian, M. G. Jiao, Z. J. Wu, K. Morokuma and S. Irle, "Step-edge self-assembly during graphene nucleation on a nickel surface: QM/MD simulations.," *Nanoscale,* vol. 6, p. 140, 2014.

[162] F. Abild-Pedersen, J. K. Nørskov, J. R. Rostrup-Nielsen, J. Sehested and S. Helveg, "Mechanisms for catalytic carbon nanofiber growth studied by ab initio density functional theory calculations," *Physical Review B,* vol. 73, p. 115419 , 2006.

[163] C. J. Wood, "Application of radiation chemistry research to the operation of nuclear reactors," *Annals of Nuclear Energy,* vol. 9, no. 4, p. 195, 1982.

[164] J. Wright, "Historical introduction to gas chemistry in nuclear reactors," in *Gas Chemistry in Nuclear Reactors and Large Industrial Plant (ed. A. Dyer)*, London, Heyden, 1980, p. 1.

[165] C. J. Wood and A. J. Wickham, "Graphite oxidation and coolant chemistry in CEGB AGRs," *Nuclear Energy,* vol. 19, no. 4, p. 277, 1980.

[166] J. V. Shennan, "Radiolytic Carbon Gasification," in *Gas Chemistry in Nuclear Reactors and Large Industrial Plant (ed. A. Dyer)*, London, Heyden, 1980, p. 98.

[167] P. Campion, "Carbon Formation Processes Relevant to Advanced Carbon Dioxide-Cooled Reactors," in *Gas Chemistry in Nuclear Reactors and Large Industrial Plant (ed. A. Dyer)*, London, Heyden, 1980, p. 53.

[168] A. Blanchard and P. Campion, "Carbon Deposition on 20/25/Nb Steel Using an Electrically Heated AGR Fuel Pin," in *Gas Chemistry in Nuclear Reactors and Large Industrial Plant (ed. A. Dyer)*, London, Heyden, 1980, p. 90.

[169] D. Norfolk, R. Skinner and W. Williams, "Mechanisms Involved in Radiolytic Carbon Deposition from CO2/CO/CH4," in *Gas Chemistry in Nuclear Reactors and Large Industrial Plant (edited by A. Dyer)*, London, Heyden, 1980, p. 67.

[170] M. J. Bennett, R. L. Faircloth, R. J. Firth, M. R. Houlton, K. S. Norwood and H. A. Prior, "Survey of The Principal Parameters Underlying Carbon Deposition on 20% Cr/25% Ni/Niobium Stabilised Austenitic Stainless Steel From CO2/CO/CH4/H2O Gas Mixtures in DIDO 6V3 Gas Loops," in *Gas Chemistry in Nuclear Reactors and Large Industrial Plant (ed. by A. Dyer)*, London, Heyden, 1980, p. 81.

[171] M. J. Bennett, G. H. Chaffey, B. L. Myatt and D. R. V. Silvester, "The heterogeneous decomposition of acetone by a 20%Cr-25%Ni-Nb stabilised austenitic stainless steel and other materials: Part 1. Kinetics and deposit characterisation (Technical Report)," United Kingdom Atomic Energy Authority, Harwell, 1973.

[172] R. A. Holm and H. E. Evans, "The resistance of 20Cr/25Ni steels to carbon deposition.

I. The role of surface grain size," *Materials and Corrosion,* vol. 38, no. 3, p. 115, 1987.

[173] R. A. Holm and H. E. Evans, "The resistance of 20 Cr/25 Ni steels to carbon deposition. II: Internal oxidation and carburisation," *Materials and Corrosion,* vol. 38, no. 4, p. 166, 1987.

[174] R. A. Holm and H. E. Evans, "The resistance of 20Cr/25Ni steels to carbon deposition. III. Cold work and selective pre-oxidation," *Materials and Corrosion,* vol. 38, no. 5, p. 219, 1987.

[175] C. Mowforth, "Mechanism and Control of Fuel-Pin Deposition," British Energy Generation Limited and/or British Energy Generation (UK) Limited Engineering Division, Internal Report, 2005.

[176] R. Lind and J. Wright, *Proceedings of the Third International Conference on the Peaceful Uses of Atomic Energy, Geneva,* vol. 9, p. 541, 1964.

[177] A. R. Blake, D. A. Hilton and I. H. Robins, "Carbon Deposition from Irradiated Methane," *Journal of Applied Chemistry,* vol. 17, p. 321, 1967.

[178] M. L. Sykes, I. A. S. Edwards and K. M. Thomas, "Metal carbonyl decomposition and carbon deposition in the advanced gas-cooled nuclear reactor," *Carbon,* vol. 31, no. 3, p. 467, 1993.

[179] E. T. C. Vogt, A. J. van Dillen and J. W. Geus, "Prevention of Growth of Filamentary Carbon in Supported iron and Nickel Catalysts," *Studies in Surface Science and Catalysis,* vol. 34, p. 221, 1987.

[180] P. C. M. van Stiphout and J. W. Geus, "Platinum-nickel catalysts: Characterisation, methanation and carbon deposition," *Applied Catalysis,* vol. 25, no. 1-2, p. 19, 1986.

[181] J. A. Cairns, J. P. Coad, E. W. T. Richards and I. A. Stenhouse, "Carbon deposition on metallic surfaces studied by r.f. plasma discharge," *Nature,* vol. 288, p. 686, 1980.

[182] W. Karcher and P. Glaude, "Inhibition of carbon deposition on iron and steel surfaces," *Carbon,* vol. 9, no. 5, p. 617, 1971.

[183] W. T. Owens, N. M. Rodriguez and R. T. K. Baker, "Effect of sulfur on the interaction of nickel with ethylene," *Catalysis Today,* vol. 21, no. 1, p. 3, 1994.

[184] M. S. Kim, N. M. Rodriguez and R. T. K. Baker, "The Interplay Between Sulfur Adsorption and Carbon Deposition on Cobalt Catalysts," *Journal of Catalysis,* vol. 143, no. 2, p. 449, 1993.

[185] E. B. Maxted and H. C. Evans, "Catalytic toxicity and chemical structure. Part I. The relative toxicity of sulphur compounds in catalytic hydrogenation," *Journal of the Chemical Society,* p. 603, 1937.

[186] J. L. S. Curtis and M. O. Baker, "Determination of unsaturation in sulfur-containing petroleum fractions by quantitative hydrogenation," *Analytical Chemistry,* vol. 42, no.

2, p. 278, 1970.

[187] C. H. Bartholomew, P. K. Agrawal and J. R. Katzer, “Sulfur Poisoning of Metals (ed. D. D. Eley, H. Pines and P. B. Weisz), vol. 31,” in *Advances in Catalysis*, Academic Press, 1982, p. 135.

[188] P. K. Agrawal, J. R. Katzer and W. H. Manogue, “Methanation over transition metal catalysts: III. in sulfur-poisoning studies,” *Journal of Catalysis,* vol. 69, no. 2, p. 327, 1981.

[189] W. D. Fitzharris, J. R. Katzer and W. H. Manogue, “Sulfur deactivation of nickel methanation catalysts,” *Journal of Catalysis,* vol. 76, no. 2, p. 369, 1982.

[190] S. Johnson and R. J. Madix, “Desorption of hydrogen and carbon monoxide from Ni(100), Ni(100)p(2 × 2)S, and Ni(100)c(2 × 2)S surfaces,” *Surface Science,* vol. 108, no. 1, p. 77, 1981.

[191] M. Kiskinova and D. W. Goodman, “Modification of chemisorption properties by electronegative adatoms: H2 and CO on chlorided, sulfided, and phosphided Ni(100),” *Surface Science,* vol. 108, no. 1, p. 64, 1981.

[192] D. W. Goodman and M. Kiskinova, “Chemisorption and reactivity studies of H2 and CO on sulfided Ni(100),” *Surface Science,* vol. 105, no. 2-3, p. L265, 1981.

[193] D. C. Gardner and C. H. Bartholomew, “Kinetics of carbon deposition during methanation of carbon monoxide,” *Industrial & Engineering Chemistry Product Research and Development,* vol. 20, no. 1, p. 80, 1981.

[194] D. A. Pask and R. W. Hall, “Review of the commissioning and operational experience of the Hinkley Point B AGR after three years' power operation,” *Nuclear Energy,* vol. 18, no. 4, p. 237, 1979.

[195] J. C. McGurk, “Long Term Variations in Hydrogen Concentration in AGR Gas Circuits,” Internal Report, AEA Technology plc, 2002.

[196] T. Ogura, T. Ishimoto and M. Koyama, “Density Functional Theory Study of Sulfur Poisoning on Nickel Anode in Solid Oxide Fuel Cells: Effects of Surface and Subsurface Sulfur Atoms,” *JOURNAL OF CHEMICAL ENGINEERING OF JAPAN,* vol. 11, p. 793, 2014.

[197] A. Rist, M. F. Ancey-Moret, C. Gatellier and P. V. Ribound, “Equilibres thermodynamiques dans l’élaboration de la fonte et de l’acier. Techniques de l’Ingénieur, traité Matériaux Métalliques, M 1730 (in French),” 1974.

[198] D. Huin, P. Flauder and J. B. Leblond, “Numerical Simulation of Internal Oxidation of Steels during Annealing Treatments,” *Oxidation of Metals,* vol. 64, no. 1-2, p. 131, 2005.

[199] M. Hasegawa, “Chapter 3.3 – Ellingham Diagram,” in *Treatise on Process Metallurgy*

(ed. S. Seetharaman), Boston, Elsevier, 2014, p. 507.

[200] "Teledyne-api," [Online]. Available: http://www.teledyne-api.com/software/. [Accessed 11 November 2017].

[201] D. R. Lide (ed.), Handbook of Chemistry and Physics, 90th edition, CRC Press, 2009.

[202] C. Park and R. T. K. Baker, "Carbon Deposition on Iron–Nickel during Interaction with Ethylene–Hydrogen Mixtures," *Journal of Catalysis,* vol. 179, no. 2, p. 361, 1998.

[203] P. V. (. Editor), "PAULING FILE in: Inorganic Solid Phases, SpringerMaterials (online database)," Springer, Heidelberg , 2016.

[204] R. J. Wakelin and E. L. Yates, "A Study of the Order-Disorder Transformation in Iron-Nickel Alloys in the Region FeNi3," *Proceedings of the Physical Society. Section B,* vol. 66 , p. 221, 1953 .

[205] J. Liu, L. J. Riddiford, C. Floristean, F. Goncalves-Neto, M. Rezaeeyazdi, L. H. Lewis and K. Barmak, "Kinetics of order-disorder transformation of L12 FeNi3 in the Fe-Ni system," *Journal of Alloys and Compounds,* vol. 689, p. 593, 2016.

[206] G. Cacciamani, J. De Keyzer, R. Ferro, U. E. Klotz, J. Lacaze and P. Wollants, "Critical evaluation of the Fe–Ni, Fe–Ti and Fe–Ni–Ti alloy systems," *Intermetallics,* vol. 14, p. 1312, 2006.

[207] C. Wagner, "Theoretical Analysis of the Diffusion Processes Determining the Oxidation Rate of Alloys," *Journal of The Electrochemical Society,* vol. 99, no. 10, p. 369, 1952.

[208] D. P. Whittle, D. J. Evans, D. B. Scully and G. C. Wood, "Compositional changes in the underlying alloy during the protective oxidation of alloys," *Acta Metallurgica,* vol. 15, no. 9, p. 1421, 1967.

[209] J. Barbehon, A. Rahmel and M. Schutze, "Behavior of the Scale on a 9.5Cr Steel under Cyclical," *Oxidation of Metals,* vol. 30, no. 1-2, p. 85, 1988.

[210] J. P. T. Vossen, P. Gawenda, K. Rahts, M. Röhrig, M. Schorr and M. Schütze, "Limits of the oxidation resistance of several heat-resistant steels under isothermal and cyclic oxidation as well as under creep in air at 650°C," *Materials at High Temperatures,* vol. 14, no. 4, p. 387, 1997.

[211] H. Gamsjager, J. Bugajski, T. Gajda, R. J. Lemire and W. Preis, Chemical Thermodynamics of Nickel, Chemical Thermodynamics Vol. 6, Elsevier, 2005.

[212] A. Vignes, Extractive Metallurgy 1: Basic Thermodynamics and Kinetics, Wiley, 2013.

[213] K. Huang and J. B. Goodenough, "Poisoning of solid oxide fuel cell (SOFC) electrodes," in *Solid Oxide Fuel Cell Technology*, Woodhead Publishing, 2009, p. 197.

[214] M. E. Fleet, "The crystal structure of heazlewoodite, and metallic bonds in sulfide

minerals," *American Mineralogist,* vol. 62, p. 341, 1977.

[215] H. J. Okamoto, "Ni-S (Nickel-Sulfur)," *Journal of Phase Equilibria and Diffusion,* vol. 30, no. 1, p. 123, 2009.

[216] D. J. Vaughan and J. R. Craig, "The crystal chemistry of iron-nickel thiospinels," *American Mineralogist ,* vol. 70, p. 1036, 1985.

[217] J. R. Rostrup-Nielsen, "Chemisorption of hydrogen sulfide on a supported nickel catalyst," *Journal of Catalysis,* vol. 11, no. 3, p. 220, 1968.

[218] C. H. Bartholomew and J. R. Katzer, "Sulfur Poisoning of Nickel in CO Hydrogenation," in *Catalyst Deactivation: Proceedings of the International Symposium*, Antwerp, 1980.

[219] J. G. McCarty and H. Wise, "Thermodynamics of sulfur chemisorption on metals. I.," *The Journal of Chemical Physics ,* vol. 72, p. 6332, 1980.

[220] J. H. Wang and M. Liu, "Computational study of sulfur–nickel interactions: A new S-Ni phase diagram," *Electrochemistry Communications,* vol. 9, p. 2212, 2007.

[221] R. Ramanathan, M. Quinlan and H. Wise, "Carbon segregation to a Ni(100) surface in the presence of adsorbed sulfur," *Chemical Physics Letters,* vol. 106, no. 1-2, p. 87, 1984.

[222] J. J. Vajo and J. G. McCarty, "Thermodynamics of carbon coadsorbed with sulfur on Ni(100)," *Applied Surface Science,* vol. 47, no. 1, p. 23, 1991.

[223] D. Salari, A. Niaei, M. R. Shoja and R. Nabavi, " Coke Formation Reduction in the Steam Cracking of Naphtha on Industrial Alloy Steels Using Sulfur-Based Inhibitors," *International Journal of Chemical Reactor Engineering,* vol. 8, no. 1, 2010.

[224] F. Zaera, E. B. Kollin and J. L. Gland, "Thiophene chemisorption and thermal decomposition on nickel(100) single-crystal surfaces," *Langmuir,* vol. 3, p. 555, 1987.

[225] F. Zaera, E. B. Kollin and J. L. Gland, "Vibrational characterization of thiophene decomposition on the Mo(100) surface," *Surface Science,* vol. 184, p. 75, 1987.

[226] A. J. Gellman, M. H. Farias, M. Salmeron and G. A. Somorjai, "A thermal desorption study of thiophene adsorbed on the clean and sulfided Mo(100) crystal face," *Surface Science,* vol. 136, p. 217, 1984.

[227] M. E. Castro, S. Ahkter, A. Golchet, J. M. White and T. Sahin, "Methanethiol decomposition on nickel(100)," *Langmuir,* vol. 7, p. 126, 1991.

[228] M. E. Castro and J. M. White, "Decomposition of methanethiol on Ni(111): a TPD and SSIMS study," *Surface Science,* vol. 257, p. 22, 1991.

[229] T. S. Rufael, D. R. Huntley, D. R. Mullins and J. L. Gland, "Adsorption and Reaction of Dimethyl Disulfide on the Ni(111) Surface," *The Journal of Physical Chemistry B ,*

vol. 102 , no. 18, p. 3431, 1998 .

[230] H. J. Grabke, R. Dennert and B. Wagemann, “The effect of S, N, and C on the oxidation of Ni-20%Cr and Fe-20%Cr,” *Oxidation of Metals,* vol. 47, no. 5, p. 495, 1997.

[231] H. J. Grabke, “Surface and interface segregation in the oxidation of metals,” *Surface and Interface Analysis,* vol. 30, p. 112, 2000.

[232] C. S. Sass and J. W. Rabalais, “Chemisorption of carbonyl sulfide (OCS) on Ni between 77 and 293 K,” *Surface Science,* vol. 194, p. L95, 1988.

[233] J. M. Saleh and F. A. K. Nasser, “Adsorption of carbonyl sulfide on nickel and tungsten films,” *The Journal of Physical Chemistry,* vol. 89, p. 3392, 1985.

[234] I. Alstrup, J. R. Rostrup-Nielsen and S. Røen, “High temperature hydrogen sulfide chemisorption on nickel catalysts,” *Applied Catalysis,* vol. 1, p. 303, 1981.

[235] D. W. Blaylock, T. G. W. H. Ogura and G. J. O. Beran, “Computational Investigation of Thermochemistry and Kinetics of Steam Methane Reforming on Ni(111) under Realistic Conditions,” *The Journal of Physical Chemistry C,* vol. 113, p. 4898, 2009.

[236] P. B. Tøttrup, “Kinetics of decomposition of carbon monoxide on a supported nickel catalyst,” *Journal of Catalysis,* vol. 42, p. 29, 1976.

[237] V. Pawar, S. Appari, D. Monder and V. Janardhanan, “Study of the Combined Deactivation Due to Sulfur Poisoning and Carbon Deposition during Biogas Dry Reforming on Supported Ni Catalyst,” *Industrial & Engineering Chemistry Research,* vol. 56, p. 8448, 2017.

[238] J. Henshaw and S. Dickinson, “Sulphur Adsorption and Speciation Effects in AGR Coolant,” National Nuclear Laboratory, 2015.